POLITECNICO DI TORINO

Dipartimento di Ingegneria
Meccanica e Aerospaziale
Corso di Laurea in Ingegneria Aerospaziale

Tesi di Laurea Magistrale

Effects of injector geometry in Air-Jet Vortex-Generator flow control

Relatori:
Prof. Gaetano Iuso
Prof. Luigi Vigevano

Candidato:
Gandolfo Scialabba

Dicembre 2018

Effects of injector geometry in Air-Jet Vortex-Generator flow control

Master Thesis

by

Gandolfo Scialabba

The present work was submitted to the Institute of Aerodynamics

Faculty of Mechanical Engineering
RWTH Aachen University

1. Examiner: Univ.-Prof. Dr.-Ing. Wolfgang Schröder
2. Examiner: Dr.-Ing. Anne-Marie Schreyer

Aachen, October 2018

Acknowledgments

I would like to express my gratitude to Dr. Anne-Marie Schreyer for giving me the opportunity to work on this project. Thanks to everyone I met at the Aerodynamisches Institut of Aachen, especially Christopher and Rasmus with whom I worked during the measurement campaign, for every precious suggestion or help from which I learned a lot and that made this whole experience very formative and enjoyable. Thanks to Prof. Iuso and Prof. Vigevano for their supervision on the work. I want to thank my family for the constant support, trust and affection they gave me during my whole life. Thanks to Jessica for being always there, even in the harder times when distant from each others. Thanks also to all my friends, especially to the Via Morghen guys who became my second family during these years in Turin. Finally, thanks to everyone I met and shared some experience with throughout my University years who contributed to make me grow up and become who I am now.

Table of contents

Chapter 1

Introduction

Flow separation has always been a major concern in all sort of aerodynamic applications, from aircraft wings, to turbomachinery, wind turbines, and more others. It consists in an abrupt thickening of the rotational flow region next to a wall, the boundary layer, which leads to a breakaway of the flow from the body itself. Separation occurs in response to an adverse pressure gradient, usually caused by a sharp direction change of the flow boundary. In case of transonic and supersonic flows a sudden rise in pressure level can be also generated by the presence of strong impinging shock waves that can cause the boundary layer to separate (Shock-Boundary Layer Interaction, SBLI). Displacement of the surrounding flow and significant losses in total pressure are a result of this phenomenon. Furthermore, the flow fields of such shock wave/boundary layer interactions are highly unsteady, characteristic that can induce strong local pressure and heat loads. If such pressure fluctuations excite a resonance frequency, structural vibrations that can cause material fatigue (buffeting) can be induced. In air-breathing engines the oscillations that are inherent with shock wave/boundary layer interactions prevent the stable operation of the engine.

For this reason, research on the reduction of separation in flows of highly loaded boundary layers was and still is largely promoted in the scientific community since some aspects, especially in supersonic applications, need to be fully understood [1, 2]. The main idea beyond control techniques is to strengthen the boundary layer by means of either passive [3] or active devices. The energizing process can be performed for example by either suction [4, 5] or blowing [6] through the wall of the area interested by the separation phenomena. A successful technology used throughout the years is the application of vortex generators [7, 8]. Vortex generators induce small longitudinal vortices which energize the boundary layer by enhancing mixing between the higher momentum external flow and the low momentum near-wall flow. These devices have been widely used in the aircraft industry, but there are two main disadvantage on their usage. First there is the introduction of additional parasitic drag [9], which more recent studies have found that can be reduced with

the implementation of sub-boundary layer vortex generators [10, 11]. The second disadvantage is connected with their passive nature and therefore the lack of an active control.

A solution to overcome the detrimental effects of vortex generators was first proposed by Wallis between the 1950s and 1960s [12, 13] with the introduction of Air Jet Vortex Generators (AJVG). In this device the longitudinal vortices are now generated by the interaction of small air jets with the incoming crossflow, reducing substantially the introduced drag. Moreover, being an active system, AJVGs can be deactivated when their application is not required, thus avoiding additional disturbances to the main flow. Their functionality has been successfully tested in various flow regimes (sub-,trans- and supersonic) in several studies [14, 15, 16, 17, 18].

This Master thesis is part of the Emmy Noether group *Separation control with Air Jet Vortex Generator arrays in transonic and supersonic flow"*, of which the main objective is to investigate the promising and flexible separation control method of air-jet vortex generators with a series of parametric studies and experimental verifications, in order to obtain a reduction of separation and of its inherent unsteadinesses. In particular, this thesis focuses on the effect of non-circular orifices on air jet vortex generator arrays for separation control, since only few cases of non-circular AJVG are reported in literature. This will be studied by examining the control of shock wave induced boundary layer separation in a supersonic flow at a compression ramp. Tests will involve a fully developed turbulent layer interacting with an oblique shock generated by a ramp. A baseline case consisting in an array of 1 mm diameter circular inclined holes performed on an interchangeable inlet has been analysed to predict which geometrical configuration could improve the AJVG system. From these experimental results, the designed shaped inlets will be introduced. The designing process will keep mass flow and other flow conditions as much similar as possible, in order to isolate only the shape influence.

First, a theoretical overview of shock-boundary layer interactions and both VGs and AJVGs control techniques, with a particular attention on vortical structures emerging from the interaction of the jets with main flow, will be given in chapter 2. A separate chapter will be then dedicated to the analysis of non-circular jet in crossflow (JICF), not only for cases with supersonic crossflow, but also in subsonic crossflow due to a larger availability of literature on non-circular jets in low-speed regimes. Chapter 4 will include all the details regarding the experimental setup. Baseline control configuration, experimental conditions and measuring methods will be described. Moreover, the design process of the inlets with non-circular orifices will be reported, with an excursus on particular manufacturing techniques required for such holes. In the subsequent chapter the experimental results for the uncontrolled and baseline controlled cases will be discussed, with some considerations on the expected results for the shaped injectors. Finally an outline and suggestion for future developments are given.

Chapter 2

Theoretical Background

An overview on Shock Boundary Layer Interaction and some control techniques will be given in the following pages. A review on turbulent boundary layers and basic shock wave structures will be described, with focus on the experimental configuration of the project. A description of the interaction between shock waves and boundary layer will follow. After a short review of other control methods such as suction, blowing and vortex generators (VGs), a more detailed description of Air Jet Vortex Generators (AJVG) control systems is finally presented.

2.1 Turbulent boundary layer

For sufficiently high Reynolds numbers, the flow past a body can be divided in two regions: an outer region where viscous effects are negligible that can be described by potential flow equations, with a good accuracy, and a very thin layer close to the body, called *boundary layer*, where the viscosity plays an important role and the flow is highly rotational. The boundary layer concept was first introduced by Ludwig Prandtl at the beginning of the 20th century and has been since then widely studied.

Inside the boundary layer, normal to the wall velocity gradients are much larger than longitudinal ones ($\partial/\partial y \gg \partial/\partial x$, where the x axis is aligned with the wall boundary of the body and the y axis is normal to it), since for an attached flow velocity goes rapidly from the no-slip condition ($u = v = 0$) at the wall boundary to the free stream values of the inviscid outer flow. Starting from the momentum equation, with an analysis of magnitude orders of velocity derivatives, boundary layer equations for a two dimensional flow can be obtained. The following formulation is valid for incompressible flows:

$$\frac{\partial u}{\partial t} + u\frac{\partial u}{\partial x} + v\frac{\partial u}{\partial y} = -\frac{1}{\rho}\frac{\partial p_e}{\partial x} + \nu\frac{\partial^2 u}{\partial y^2} \tag{2.1}$$

When the flow incurs in a further increase in the Reynolds number turbulent transition takes place. Boundary layer transition can also arise due to adverse pressure gradients, roughness of the surface or active modification of wall conditions (e.g. blowing), in general anything that perturbs sufficiently the flow to cause its instability. Transition is a very complex process and its prediction remains a topic of intense research. In turbulent boundary layers, velocity fluctuations are more prominent and cause additional stress (Reynolds stresses). While laminar boundary layer can be idealized as a series of flow layers sliding onto each other in an ordered manner, the structure of turbulent boundary layers is mainly dominated by the random motion of turbulent eddies. The latter is thus characterized by a larger exchange of mass, momentum and energy on a wider scale than the microscopical viscous exchange typical of laminar fluids.

In general, turbulent boundary layer profiles present a steeper rise in mean velocity, with a consequent flatter profile away from the wall. This flatness can be quantified by the shape factor H defined as the ratio of displacement thickness δ^* and momentum thickness θ. For the Blasius solution (steady two-dimensional laminar boundary layer that forms on a semi-infinite plate with a constant unidirectional flow) its value is typically assumed as $H = 2.59$, while for turbulent boundary layers (e.g.[19]) a common value for a flat plate is $H = 1.3 - 1.4$ [20] and it decreases when both Mach and Reynolds numbers increase [21]. Thus turbulent transition is characterized by a substantial decrease of H.

Turbulent boundary layers can be described by means of normalized parameters:

$$y^+ = \frac{y u_\tau}{\nu} \qquad U^+ = \frac{U}{u_\tau}$$

where $u_\tau = \sqrt{\tau_w/\rho}$ is the friction velocity, τ_w the wall shear stress and y the distance from the surface. It can be subdivided in the following regions [22]:

- A viscous sublayer for $y^+ < 5$, where $U^+ = y^+$ and viscous effects are predominant
- the *log-law* region which holds for $y^+ > 30 - 50$ and $y/\delta < 0.1$, where $U^+ = \frac{1}{\chi}\ln y^+ + B$ and χ is the Von Kármán constant. For a large variety of flows $\chi = 0.41$ and $B = 5.2$. The transition region between the viscosity-dominant and the turbulence-dominant parts of the flow is called *buffer layer*.

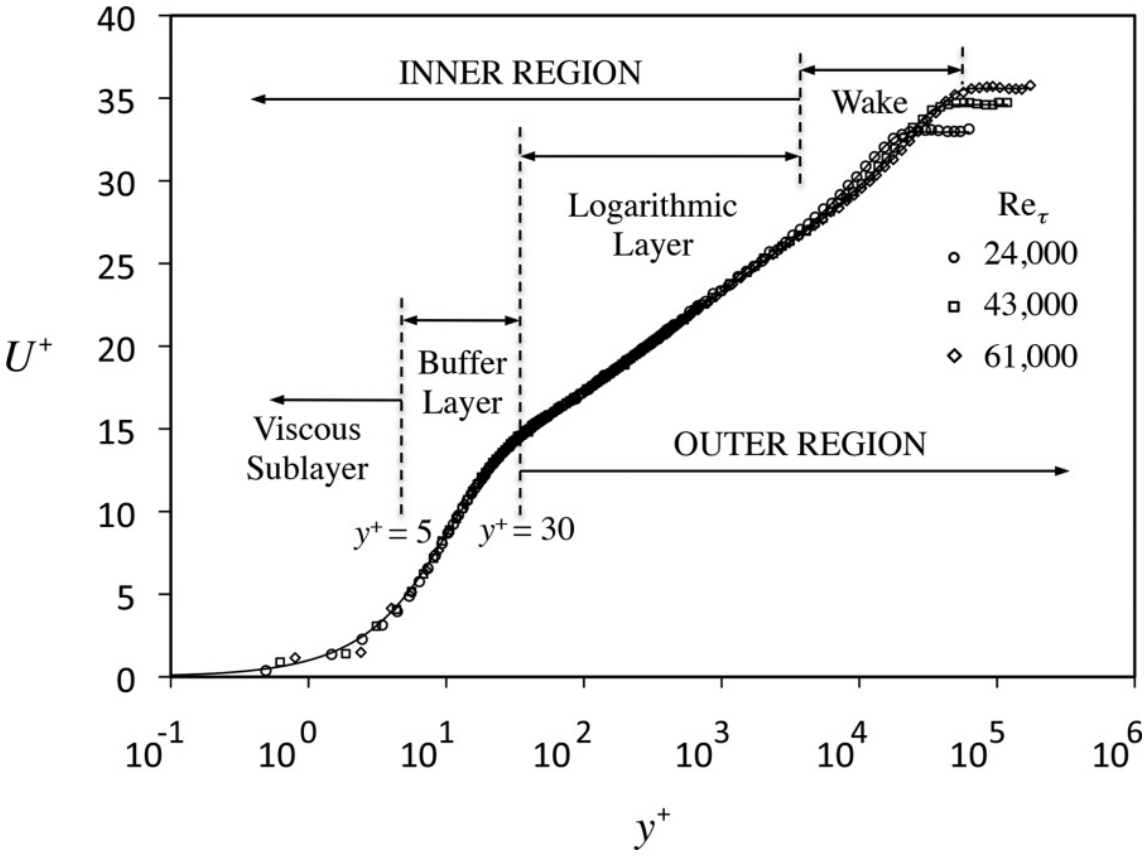

Figure 2.1: Mean velocity profile of a smooth-flat-plate turbulent boundary layer plotted in log-linear coordinates with law-of-the-wall normalizations. Experimental (dotted) and theoretical (solid) results compared for different Re. From [24]

- The outer part is called the *defect-velocity* region, where the mean velocity starts to deviate from the log-law. For turbulent boundary layers the velocity profile can be described by Coles' empirical *law of the wake*. According to this formulation the outer part of a turbulent boundary layer behaves like a turbulent wake, thus neglecting wall effects.

A representation of this subdivision is given in figure 2.1 for a smooth flat plate. To take into account compressibility effects, further corrections must be applied [20, 23].

In order to describe the interaction between viscous and inviscid of a wall flow, the *triple deck* structure (figure 2.2) was introduced by Lighthill [25]. The flow along a solid surface can be divided in three layers:

1. An outer inviscid and irrotational part (the latter condition with some exception)

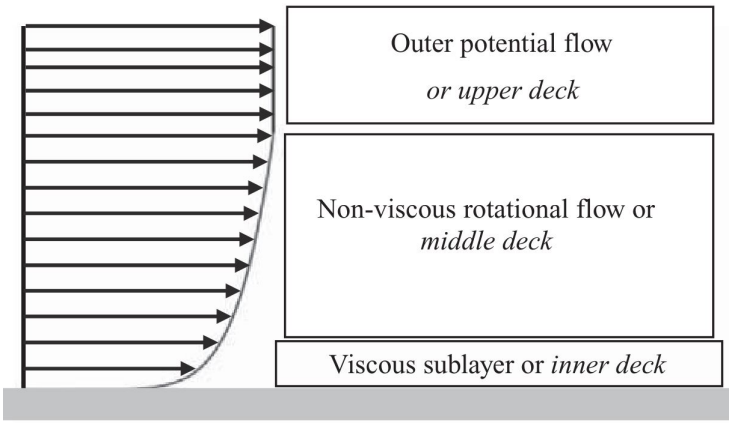

Figure 2.2: Triple deck structure of a boundary layer [21]

2. An intermediate region, within the boundary layer but sufficiently far from the wall, where the flow can still be considered inviscid but with highly rotational characteristics. In a turbulent boundary layer, the middle deck represents the greatest part of the boundary layer even at moderate Mach number.

3. A third layer directly in contact with the wall where viscous forces are predominant.

This subdivision is valid for flows in which time scales of any phenomena are short compared to the viscous ones, except for the inner layer. Such conditions are verified in case of Shock-Boundary Layer Interaction (SBLI), therefore the flow can be described applying this model [21].

2.1.1 Boundary layer separation

Considering the general boundary layer equation (2.1), for an attached steady flow at a wall position $y = 0$ ($u = v = 0$) it reduces to

$$\frac{1}{\rho}\frac{\partial p_e}{\partial x} = \nu\frac{\partial^2 u}{\partial y^2} \tag{2.2}$$

When a favourable pressure gradient is present ($\partial p_e/\partial x < 0$), the u component second derivative is negative, thus $u(y)$ presents a negative curvature that means a decreasing slope of the function. Since the boundary layer tends to the external u_∞ value, a trend of the function can be represented as in figure 2.3a. In case of an adverse pressure gradient ($\partial p_e/\partial x < 0$) the slope of $u(y)$ results first in an increase and then to satisfy the outer flow condition ($\partial u/\partial y = 0$) needs to decrease again. For sufficiently strong adverse gradient this allows $\partial u/\partial y|_{wall} = 0$, which

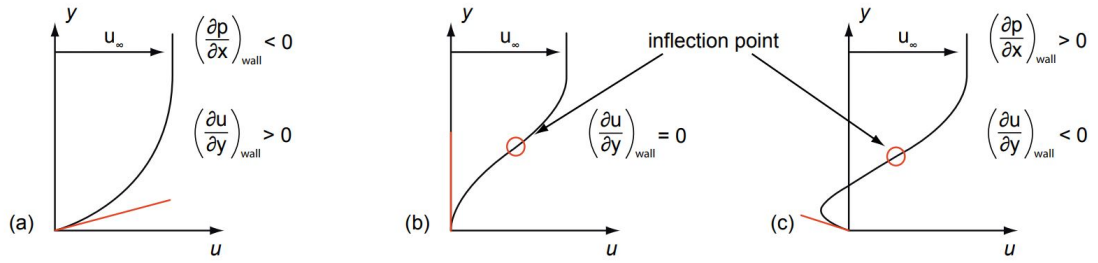

Figure 2.3: Schematic of boundary layer separation. Case (a) attached flow with favourable pressure gradient, case (b) separation condition with adverse gradient, case (c) reverse flow after separation.

is assumed as the condition for an attached flow to separate (figure 2.3b). Higher values allow a negative slope at the wall which means that a portion of the flow is reversed after separation (figure 2.3c). In physical terms, an adverse pressure gradient causes a deceleration of the flow. If this delay is sufficient enough, the flow inertia of boundary layer's lower part is too weak to outlive this deceleration and it separates from the wall, generating also regions of back flow.

Strong adverse pressure gradient can be caused by downstream condition, large pressure recovery in high attack angle airfoils and other conditions. In supersonic flows, sudden pressure rise can emerge from compression shocks. Flow separation is characterized by a large displacement of the flow from the wall. This translates in a sudden increase in boundary layer parameters such as displacement thickness δ^* and shape factor H. Its important to notice that turbulent boundary layers are less prone to separation than laminar ones as a consequence of a larger momentum in the near wall region. For separation to occur in turbulent boundary layer, the shape factor H has to increase to a critical value starting from a lower one ("fuller profile") than the laminar counterpart.

2.2 Shock Wave-Boundary Layer Interaction

Supersonic flows are characterized by severe compressibility effects. They are often linked with non-linearities emerging from shock waves, strong compression waves across which flow properties undergo abrupt changes. Being the thickness of this interaction region just a few times the molecular mean free path, shock wave can be described as discontinuity by means of the Rankine-Hugoniot equations. The only quantity conserved through a shock wave is the total enthalpy, while static pressure increases substantially and velocity decreases, with a loss of stagnation pressure. Shock topology is strongly related to both flow conditions and geometry. Normal shocks are the most intense and directly cause the flow behind to become subsonic.

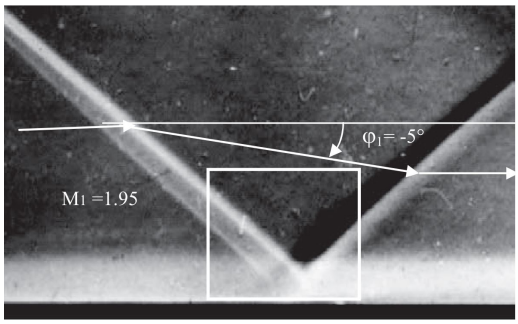

Figure 2.4: Shock-Boundary Layer interaction without separation for a reflected oblique shock at Ma=1.95 [21]

Figure 2.5: Single lambda shock wave on an airfoil with a laminar boundary layer at Ma=0.9 [27].

When a supersonic flow encounters a blunt body a detached bow shock is generated, while for sharp geometries oblique shocks can be observed. Flow behind an oblique shock undergo a deflection and may remain supersonic, as a result of a reduced intensity. Shock patterns may arise due to wall reflections or interaction between different perturbations [26].

As mentioned earlier, the strong adverse pressure gradient generated by a shock wave leads to a thickening, and eventually a separation, of an incoming boundary layer. This interaction is quite complex and it is usually referred as *Shock-Boundary Layer Interaction* (SBLI). Schlieren visualizations of two examples of SBLI are reported in figures 2.4 and 2.5 (from [21] and [27] respectively). The first picture shows an oblique shock reflection at a flat surface that, along with compression ramps, is characteristic of supersonic air-intakes. The second one is an interaction between a lambda shock on a transonic airfoil and a laminar boundary layer, of which both transition and separation are induced by the shock itself.

According to the triple deck hypothesis, the initial phase of an SBLI can be analyzed with an inviscid flow assumption, therefore inertia terms are predominant. Since shock waves can usually penetrate a large part of the boundary layer these assumption are valid with, however, considering viscous terms in the near wall region that are necessary to assure consistency with the wall no-slip condition [21].

As a result of the confined interaction region between the shock and the boundary layer, streamwise derivatives become comparable to wall-normal ones, opposed to classical boundary layers. Same applies for normal components of the Reynolds stress tensor with turbulent shear stress component. The response to a sudden pressure increase of these stresses is affected by some delay, hence a decoupling of mean velocity and turbulent fields is observed. This complex mechanism, especially when separation occurs, makes it difficult to find an adequate turbulence model for

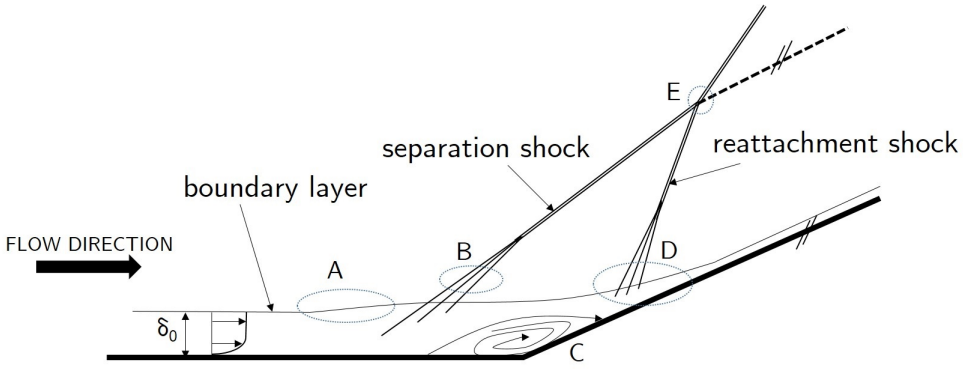

Figure 2.6: Schematic of an SBLI at a compression ramp: (A) boundary layer thickening, (B) formation of separation shock, (C) recirculation area, (D) reattachment shock, (E) triple point ([31] redrawn from [30]).

SBLIs [28].

SBLIs take place in various flow configuration but a more detailed analysis of compression ramp induced SBLI will be now provided as the experimental configuration of the thesis belongs to this category. It is a situation of particular interest in supersonic engine air inlets of which the main function is to decelerate the flow to subsonic conditions. This deceleration may be achieved by a single normal strong shock (Pitot type), but it would result in an excessive loss of total pressure. Therefore a system of oblique shocks induced by one or more compression ramps is preferred. A detailed analysis of this particular flow structure has been carried out by Settles [29, 30] and the following description will mainly refer to his experiments.

A schematic of the flow is showed in figure 2.6. The incoming boundary layer first reaches the shock region, incurring into a thickening (A) due to the pressure rise. The flow then undergoes an initial turn at separation and generates a shock wave, which is composed by merging compression waves (B). In the corner region (C) after flow separation a recirculation area , often referred as separation bubble, is present as a result of the strong deceleration caused by the shock. A further pressure increase inside this area causes the formation of a second compression fan (D), which again merge in a second shock where the flow reattaches to the wall. The two oblique shocks determine the boundaries of the overall shock-boundary layer interaction and they both merge and form a main shock in the triple point (E), where also a slip line is generated to ensure separation between two different flow conditions.

Oil flow visualizations for 8°, 20° and 24° compression corner flows at Mach=2.85 from Settles [30] are showed in figure 2.7. For lower redirection angles of the flow (8°) no separation occurs, while at higher values (20° and 24°) recirculation areas are displayed by flow traces of the oil mixture. Larger deflections translate in stronger shocks which in turn generate a wider separation bubble. Additionally, wall pres-

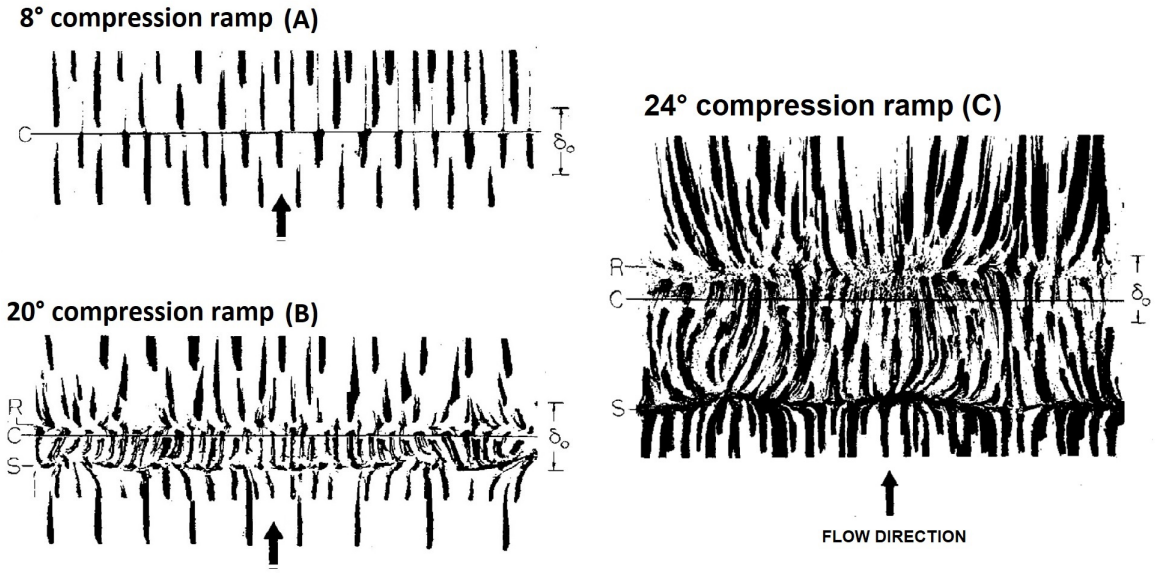

Figure 2.7: Oil flow visualization for 8° (A), 20°(B) and 24° (C) compression corner flows at Mach=2.85 [30]. Separation (S) and reattachment (R) shock positions are indicated

sure measurements, captured with a series of longitudinal and transverse surface tap, from the same study for the 24° ramp are exhibited in figure 2.8. It is worth noticing that the pressure rise in the separation area is lower than the one caused by the shocks. This leads to an overall lower pressure rise than the one obtained with inviscid considerations [29], showing the effects of total pressure loss of these phenomena.

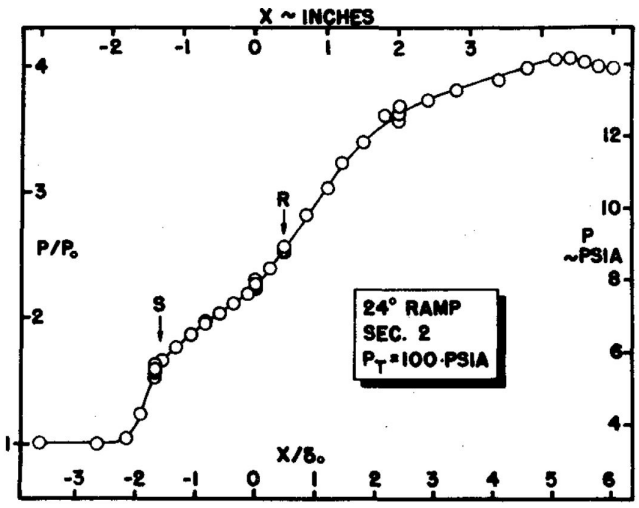

Figure 2.8: Surface pressure distribution on a 24° compression corner [29]

Strong enough shock waves associated with SBLIs which cause the flow to separate are also linked with large-scale unsteadiness. Low-frequency oscillations are observed in a sort of "breathing" mechanism in which the separated region is first injected with mass from the incoming flow and then ejects it downstream. These oscillation may cause buffeting on wings or buzz for air-intakes [21, 32]. This condition might limit substantially a veichle's performance and, if the fluctuations are strong enough, can prevent for example the stable operation of an engine or structural damages of the airframe. Therefore, various flow control techniques have been implemented in order to reduce the detrimental effects of SBLI. Two ways can be followed for this purpose: shock control and boundary layer control.

The first one mainly consist in altering the shock position and structure to reduce its intensity that in turn reduces boundary layer thickening. This can be performed by deflecting the outer flow with the additions of bumps or slots in the surface [3]. Such modification favour the reduction of intensity or the change of normal shocks in systems of multiple oblique shocks with an overall lower intensity. However they also introduce regions of additional viscous drag and, moreover, their application requires a previous knowledge of the shock position which under off-design conditions tends to change, increasing drastically drag penalties and possibility of additional shocks [21].

The second and most diffused solution is the direct control of boundary layer of which some methods will be described in the following, in particular the usage of air jet vortex generators (AJVG) that is the main scope of this work.

2.2.1 Control techniques - suction and blowing

Considering the simple two dimensional boundary layer equation 2.1 at a wall surface, assuming now that a normal velocity component can be introduced ($v \neq 0$), for a steady case it reduces to:

$$\frac{1}{\rho}\frac{\partial p_e}{\partial x} = \nu\frac{\partial^2 u}{\partial y^2} - v\frac{\partial u}{\partial y} \tag{2.3}$$

An increased stabilization of the boundary layer against adverse pressure gradients can be obtained with suction, the addition of a negative component on the normal velocity. Suction efficacy on drag and separation reduction has been proved already by Prandtl in his boundary layer theorization and since then has been largely implemented in several applications [20]. Suction can be performed either by discrete slots or by means of distributed holes (e.g. perforated plates). Krogmann et al [4] verified the effectiveness of three different suction configurations, single/double slot and perforated strip with a cavity underneath, on SBLI induced separation for a

transonic airfoil, obtaining good results for all three cases. Positive effects of these configurations have been reported even without suction, due to a passive action of the added cavities. Babinsky [5] documented an effective counteract of boundary layer parameters increment linked to separation such as the shape factor H, by means of suction in an oblique shock interaction.

In a similar fashion, boundary layer can be energized via tangential upstream blowing performed through wall slots which supply additional higher velocity to the fluid elements on the low momentum region. The main disadvantages of these two technologies are related to additional drag penalties (e.g. *sink drag* in slot systems), losses of inlet performance due to bleed air, need of a substantial mass flow rate and consequently of an air supply system. Bleed losses can be reduced by means of active control of the system, but the requirement of high mass flows can still be problematic in certain applications.

2.2.2 Control techniques - Vortex Generators

A widely used method for boundary layer control is the implementation of vortex generators (VG). Their working principle is based on the introduction of longitudinal vortices in the boundary layer region in order to strengthen it. These vortices cause an internal transfer of momentum between different layers of the flow [7]. Outer flow characterized by a larger momentum is transferred to the near-wall viscous region which instead is weakly energized. In the same manner, low energetic flow is pushed up into the main flow. This exchange favours an overall reinforcement of the boundary layer and a subsequent lowering of its integral parameters, counteracting detrimental effects of adverse pressure gradients. A schematic of this mechanism is showed in figure 2.9.

In SBLI cases, the longitudinal vortices generated by the interaction of these devices with main flow can penetrate the shock system, introducing beneficial effects in the recirculation area. Induced vortices show a span-wise vortex movement as they fully develop in the main flow [7], therefore an optimal effect is obtained placing

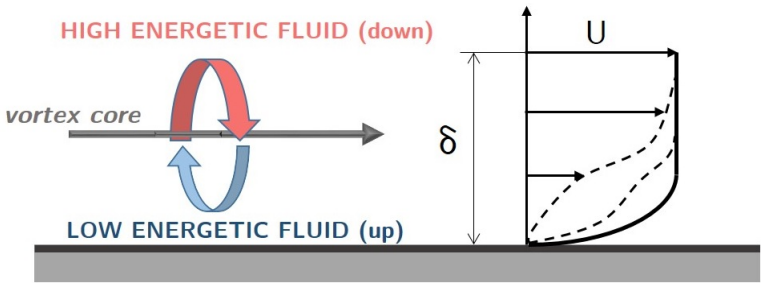

Figure 2.9: Schematic of Vortex Generator induced momentum exchange

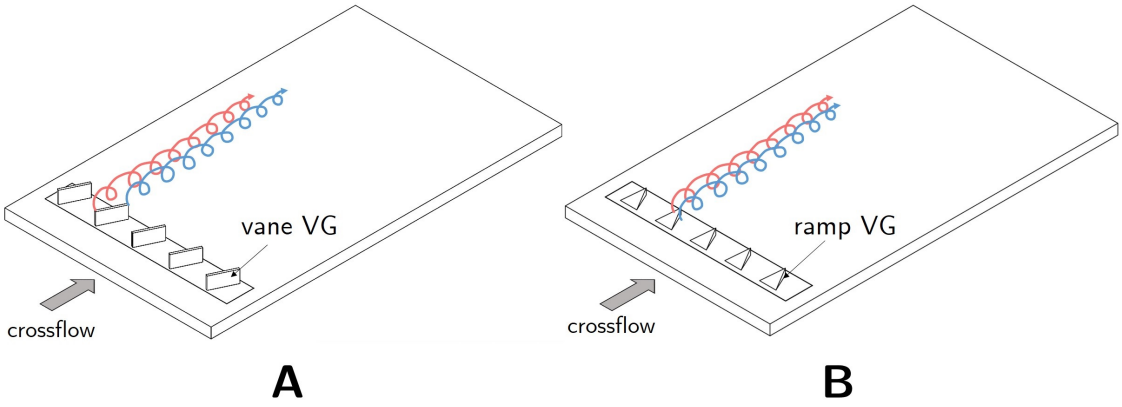

Figure 2.10: Schematic setup of Vane-Type (A) and Ramp Type (B) vortex generators

VGs within a certain distance to the SBLI region.

Implementation of VG introduces an expanding degree of freedom in the design process, consequently several possible configuration are possible. A first classification is made on the geometry, distinguishing mainly two possibilities: Vane-type VGs and Ramp VGs (see figure 2.10).

Vane-type vortex generators consist in simple rectangular or delta-shaped winglets on which tips a pair of vortices is generated. They are usually assembled in a co-rotating or counter-rotating disposition (figure 2.11). In some applications, vane-type vortex generators are problematic due to their perceived mechanical fragility. In these situations ramp-type VG are therefore preferred. A pair of counter-rotating streamwise vortices are generated from the tip of the ramp, but also backward configurations are possible (figure 2.12). However, ramp-type VGs have been proved to be less effective than the vane-type counterpart in reducing the separation length on SBLIs [7, 10]. Several other geometries have been implemented, such as wave-type VGs, Wheeler doublet and wishbone VGs and others [8].

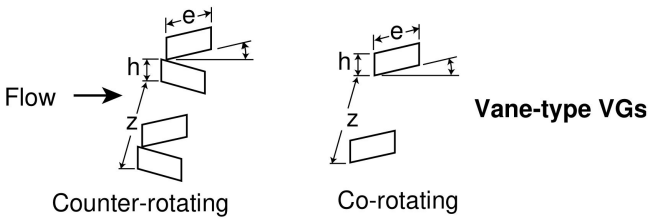

Figure 2.11: Vane-Type configurations

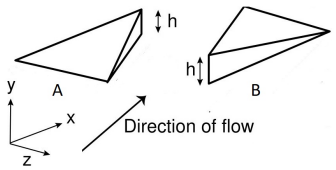

Figure 2.12: Ramp-Type configurations: forward wedge (A), backward wedge (B)

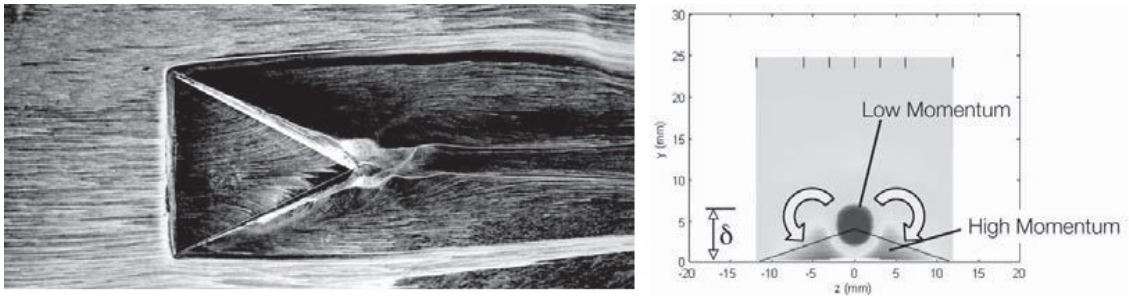

Figure 2.13: Surface oil flow visualization of a micro-ramp vortex generators and relative velocity change measured downstream of the device. From [21]

Conventional vane-type vortex generators' height, h, is on the order of the boundary layer thickness, δ. However, many aerodynamics application use these relatively large VGs to control a localized flow separation over a relative short downstream distance. Such type of VGs may cause excessive residual drag, penalizing the overall performance of an aircraft [9].

Reduction of parasitic drag can be performed using sub-boundary-layer vortex generators (SBVGs), or also called micro-vortex generators (MVGs). These devices' height is lower than boundary layer thickness, usually $h/\delta \approx 0.2 - 0.5$, and in virtue of both the smaller wetted area and a positioning into much slower region, they provide a substantial reduction into viscous parasitic drag. Kuethe [33] examined a particular type of wave-type VGs with a ranging height of $h/\delta \approx 0.27 - 0.42$ that use the Taylor-Görtler instability to generate streamwise vortices inside the boundary layer, obtaining a reduction in intensity of acoustic disturbances in the wake region by suppressing vortex shedding. Görtler vortices are secondary flows that occours when the wall curvature, in this case due to MGVs, is comparable to the boundary layer thickness and centrifugal action creates pressure variation across the BL causing the previously mentioned instability. MVGs have been effectively used also in SBLI cases. Reduction of a normal shock induced separation by means of these devices for a Mach 1.5 flow has been analyzed by Holden et al [10]. Both ramp and vane type MVGs have been tested and the latter resulted to be more effective, as a consequence of a wider separation of the produced vortices and a smaller lift off from the surface [10]. A surface oil flow visualization of micro-ramp vortex generators from [21] is showed in figure (2.13). An effective exchange between different momentum flow regions can be seen in the sided plot. In general, due to the reduced size, micro-vortex generators need to be placed closer to the interaction area to be controlled, in respect to the larger VGs. A detailed overview of Vortex-Generators is given in Lin's paper [8], where several other implementation of MVGs in shock-induced separation control are reported.

Although it can be attenuated, VG induced parasitic drag is still present also in flow situation where boundary layer control is not needed, for example in airfoils in cruise

conditions. Additionally, implementation of VGs in critical parts such as turbine blades is usually avoided because of the danger of their possible detachment [34]. Moreover, vortex generators cannot be used for active stall control or in general conditions in which they are required only in specific time intervals. A possible alternative to overcome these difficulties are air jet vortex-generators (AJVG) which are described in more detail in the next section.

2.3 Air Jet Vortex Generators (AJVG)

The main idea behind air jet vortex generators (AJVG) is to generate an effective vortical structure for the momentum exchange, as with mechanical VGs, exploiting instabilities resulting from the interaction of a transverse jet with the incoming flow. Air is injected through small jet holes on the surface with a certain angle and it interacts with the main flow, generating a system of vortices which is convected downstream. Momentum mixing is thus obtained as in classical VG. Although fixed solid-vortex generators are characterized by an inherent constructive simplicity and low costs, an active control implementation is rather complicate therefore, as previously discussed, parasitic drag incurs also when flow control is not required. On the contrary, air-flow control by means of AJVG might be easily managed with direct control on air supply lines. Therefore jets can be deactivated and parasitic drag is avoided [9]. Furthermore, AJVG can be implemented in critical parts where an eventual detachment of mechanical appendices is dangerous (e.g turbine blades).

However, pressurized air must be provided and appropriate supply system are needed. To reduce the amount of additional components, using engine compressor bleed air or even sources of stagnation air might be sufficient since the mass flow required in case of microjets is small [9, 12]. Krzysiak [35] tested a self-supplying air-jet vortex generator system on a modified NACA 0012 airfoil, where air is extracted from the airfoil overpressure region in the nose part. Although the resulting effectiveness was less than a conventionally supplied system, he achieved a significant simplification of the system. Successful applications of self-supplying (or seldom referred as passive) AJVG have been documented also in wind turbine applications [36] and in SBLI control [37] with good results.

First studies on AJVG have been conducted between the 1950s and 1960s by Wallis [12, 13], which first established this technology with comparable results to the classic mechanical VGs for a transonic airfoil at $Ma = 0.9$. An 8% chord bump has been used to recreate the airfoil and air was injected from a 2,75 bar supply. Later studies on a similar flow configuration of Wallis experiments were conducted by Rao [15]. Two additional bump cases were added (10% and 14% of the chord length), introducing also rectangular jets that resulted more effective than the regular round jets under certain pressure conditions. Several studies on AJVG in subsonic boundary

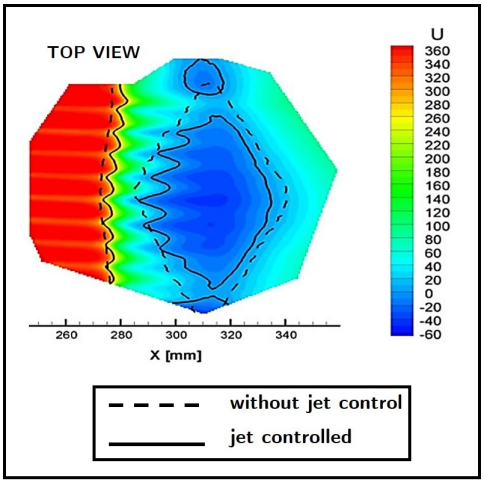

Figure 2.14: Mean longitudinal velocity obtained by means of PIV-measurements in a top-view plane [18]

layer control applications have been then performed, with analysis on jet inclination, speed and other relevant parameters [16, 14, 9]. Usage of AJVG in shock-induced separation control was investigated by Szwaba [17, 34], Souverein and Debiève [18] among the others. PIV measurements results from Souverein and Debiève studies are reported in figure 2.14. They show a substantially reduced recirculation area, in both longitudinal extent and area. This was obtained with an array of 45° inclined round jets (0,8 mm diameter) for a $Ma = 2.3$ flow. Injection was performed at a 90° skew angle. A corrugated line and further traces generated by the longitudinal AJVG induced vortices can be observed in the shock area. They also report an increase in shock oscillation frequency of about 50% as a direct consequence of recirculation bubble reduction [18].

AJVG test on separation reduction for a 24° compression ramp and a Mach 2 flow have been conducted by Verma et al [32]. Two sets of parameters are compared in their study, both resulting in a sensible separation region reduction. Schlieren and surface oil flow visualization for the clean configuration and one of the two AJVG sets are visible in figure 2.15. From both visualization is it possible to see a downstream shifting of the separation shock, while the reattachment shock moves upstream. The typical corrugated separation line of the controlled case is again present in the oil flow pictures and flow trails of reverse flow are clearly visible. In the clean configuration an accentuated curvature of the reattachment line can be seen, while for the same line in the controlled case the three-dimensionality is lost.

Further detail on AJVG working principle are given in the next subsection. An overview of AJVG design parameters will follow.

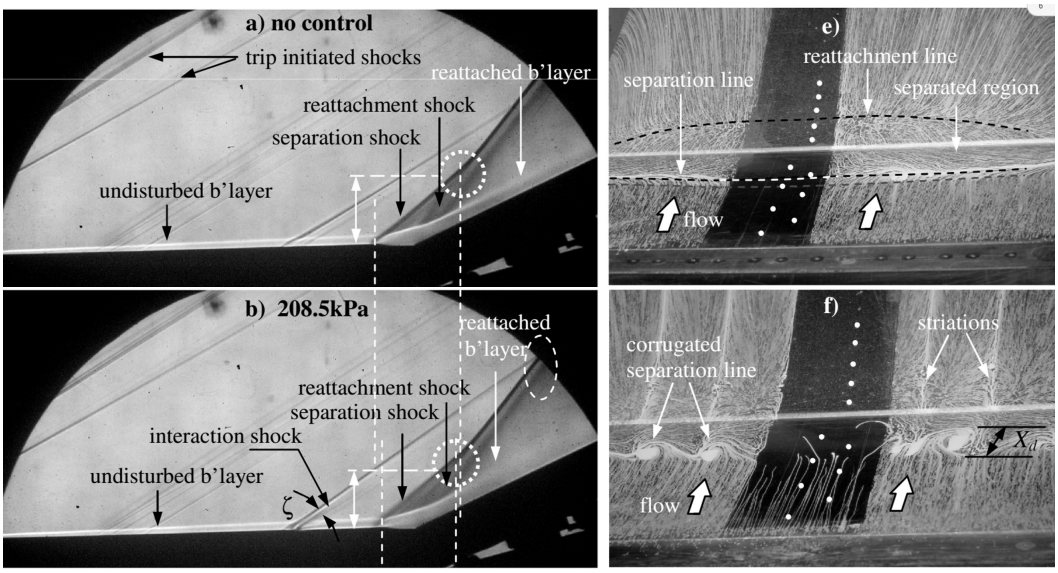

Figure 2.15: Schlieren and oil flow visualization for a non controlled case (first row) and an AJVG controlled case (second row) [32]

2.3.1 Vortex generation from jets in crossflow

The core mechanism behind air-jet vortex generators is the interaction of transverse jets with the main flow. Jet in crossflow (JICF) have been used in a wide range of engineering application other than separation control: film cooling for turbines and combustors, fuel injection for burners, vectored thrust, suppression in cavity flows and others. Therefore it is a classically studied fluid dynamic problem. In case of subsonic crossflow, four types of coherent structure can be discerned in the near field of the jet, where the three-dimensional interaction with the main flow is more intense. A detailed description of these structures for a low speed crossflow is provided by Fric and Roshko [38, 39] and it is here reported. A sketch of the four types of vortical structures is showed in figure 2.16.

First, jet shear-layer vortices, resulting from the Kelvin-Helmholtz instability of the annular shear layer that separates from the edge of the orifice, can be observed. Lateral smoke and streaklines visualization of a transverse jet show the interaction of the leading edge with the main flow (figure 2.16). Entrainment of the flow into the jet can be seen from the streaklines. These vortices are similar to the vortex ring structures of free jets [38].

A system of horseshoe or collar vortices at the crossflow wall is generated. These structures wrap around the jet base and mantain a distinct structure until just downstream of the orifice where the jet's wake turblence dissipates them. A similar structure is present in a flow around the base of a wall-mounted circular cylinder.

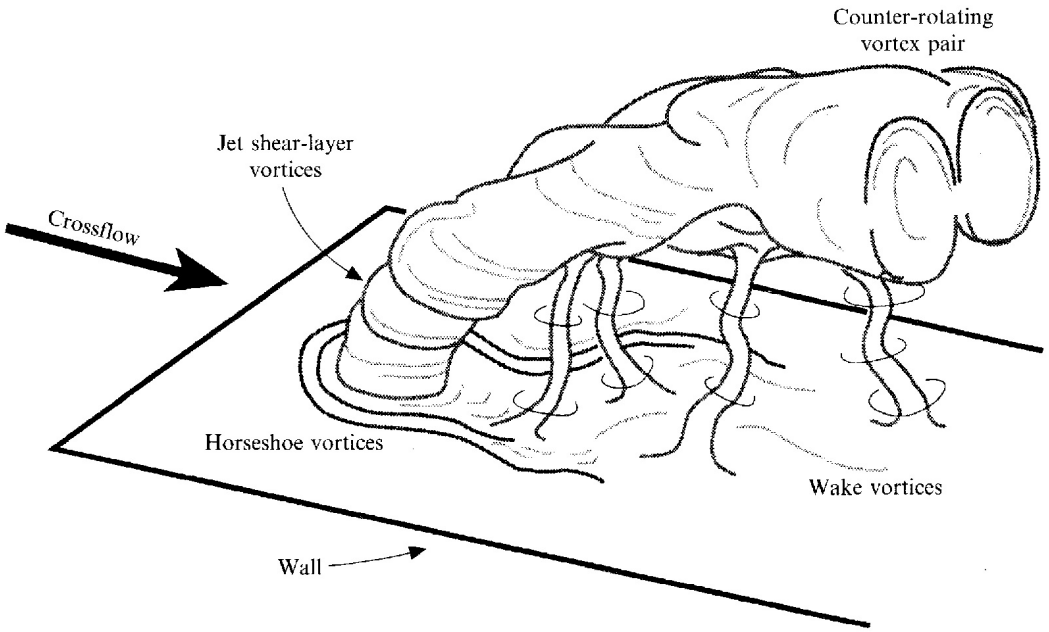

Figure 2.16: Sketch of the four types of vortical structures associated with the interaction of a transverse jet with crossflow [39]

The third visible structures on the sketch are wake vortices. According to Fric and Roshko, differently than it was usually believed, their formation mechanism is different from the shedding of vorticity from solid cylinders. They are originated from the crossflow boundary layer which separation generates a series of tornado-like vortices extending from the boundary layer to the jet plume over it (figure 2.16) [39].

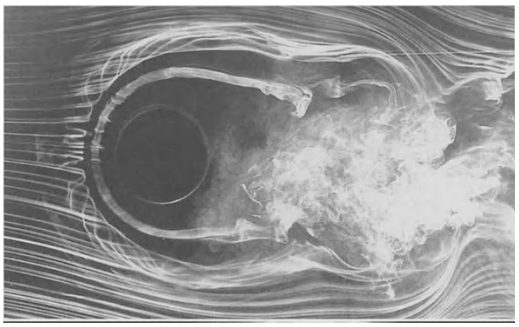

Figure 2.18: Horseshoe vortex system - Top view of a streakline visualization [38]

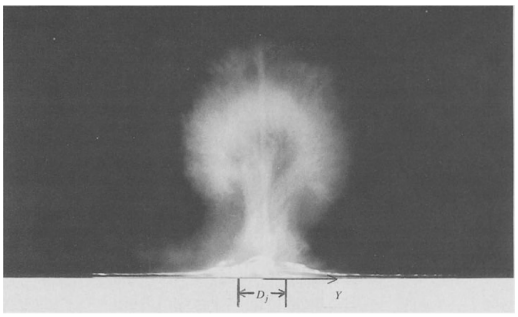

Figure 2.19: Counter-rotating vortex pair early formation - Front view of a smoke visualization [38]

Finally, the most important interaction related to air jet vortex generators is the formation of a counter-rotating vortex pair (CVPs), which are the main actors in

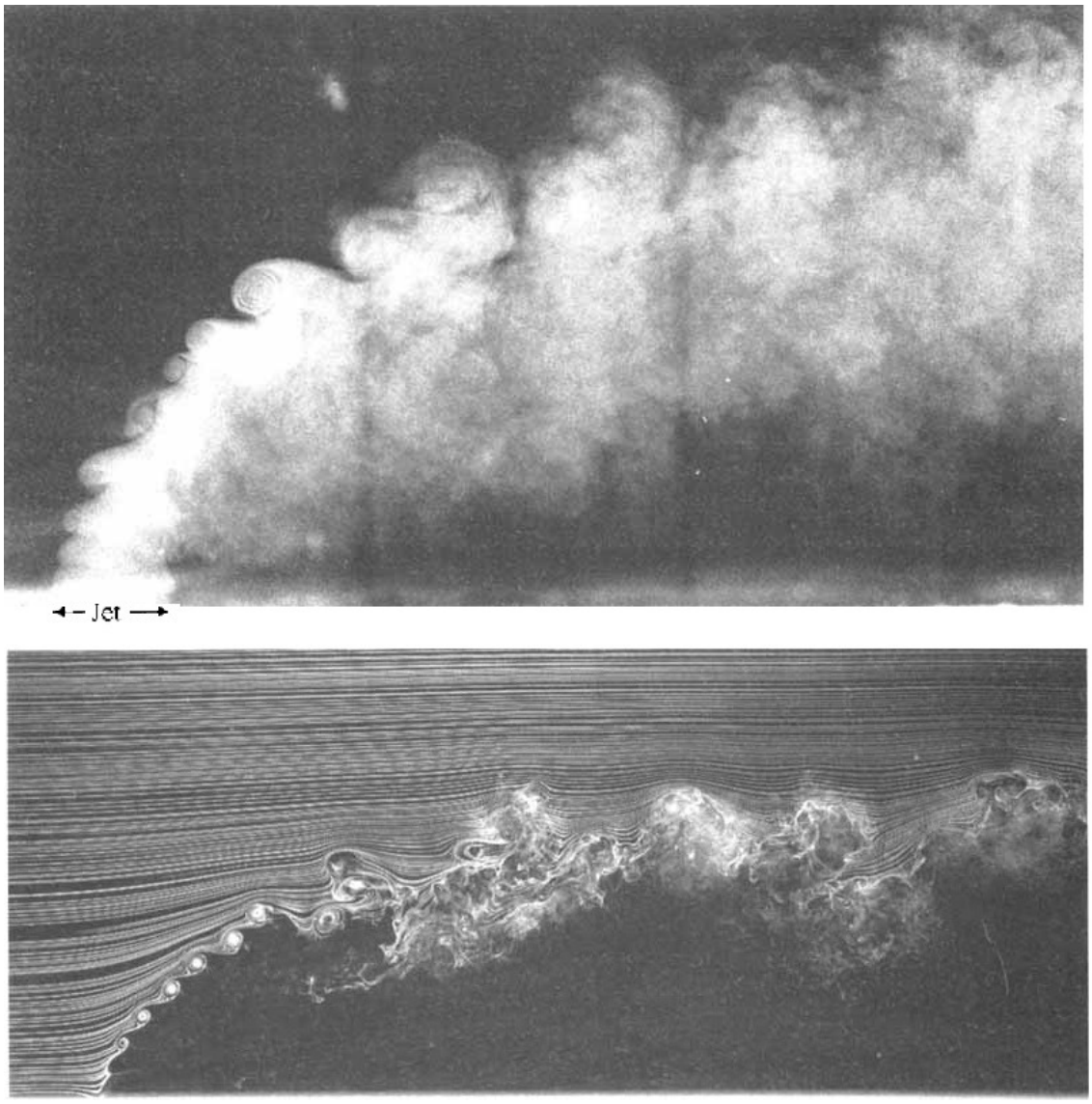

Figure 2.17: Transverse-jet shear layer structure visualized by a smoke-filled jet (top) and by smoke streaklines (bottom) for a low speed crossflow [39].

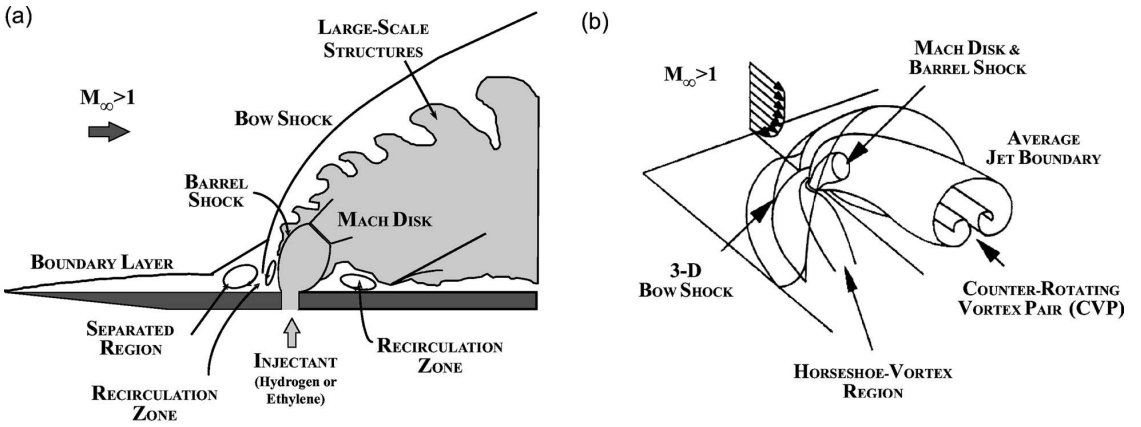

Figure 2.20: Schematic of an underexpanded jet in a supersonic crossflow. Lateral view (a) and 3D view (b)

the momentum mixing process for boundary layer energization. This vortex pair dominate the cross-section of the jet, especially in the far field where they are convected by the crossflow. They result from a major periodic roll-up process of the jet shear layer. The initially vorticity issued from the nozzle is forcedly re-oriented by the crossflow, leading to a folding of the cylindrical vortex sheet. The superposition of these two mechanism describe the evolution of downstream convected vorticity. Shear layer of the jet folding and rolling is also present very closely to the jet exit, which contributes to the formation of the CVPs. Additional vorticity is also provided by other vortex systems such as the previously mentioned wake vortices, which distort the roll-up process [40].

In case of supersonic crossflow the corresponding interaction presents further complications. Jets act as an obstacle in the flow, therefore a shock system arise. The main vortical structures in supersonic configurations are rather similar to the just described ones for subsonic cases. Schematics of an underexpanded transverse injection into a supersonic crossflow are pictured in figure 2.20. The obstruction caused by the jet acts as a blunt body and induces a three-dimensional bow shock in the freestream. After leaving the orifice, the jet expands through a Prandtl-Meyer fan and then compresses by means of a barrel shock and a Mach disk (illustrated in the lateral view of the picture). Afterwards, the jet plume is quickly bended towards the wall in the flow direction. The two characteristic counter-rotating vortex pair are then generated in the plume and convected downstream afterwards. In contrast with subsonic JICF, Santiago and Dutton [41] observed an increased confinement of the vortex pair as they move apart, probably caused by the high compressibility effects of the $Ma = 1.6$ crossflow and the low momentum of the jet considered in their experiments.

For a transverse injection the obstruction can generate a sufficiently strong bow

shock which may induce a separated region upstream of the jet and a further recirculation area ahead of it [32]. This separation might be reduced or even avoided by either an inclined injection or a change in the orifice shape. Further details on this aspect will be given later. Jets used in AJVG applications are often quite small compared to the boundary, with a diameter of $d \approx 0.1 - 0.2\delta_0$, in analogy with the implementation of sub-boundary layer mechanical vortex generators. Weaker vortices are produced but, on the positive side, also less disturbance is introduced into the main current because of the reduced mass flow. Besides, such micro-jets operate within the boundary layer region, providing higher velocity flow in the viscous sub-layer. In the same fashion of VGs, they are referred as micro air jet vortex generators (MAJVG), but this additional adjective will be dropped for convenience, referring to the AJVG without size distinction. In order to obtain an efficient energization of the low momentum region of the boundary layer, it is required that the obtained CVPs do not lift up excessively from the wall surface, reducing the desired effect.

Since AJVG are composed of arrays of jets and not single ones, it is important to consider the interaction between adjacent jets and the relative CVPs. A study on arrays of micro-jets in supersonic crossflow has been conducted by Ali and Alvi [42]. Along with other parameters, two different sizes (400 and 800 μm) with various spacing have been analyzed. Through stereoscopic PIV measurements on different streamwise planes, a distance of 5 diameters has been calculated between two vortex cores emerging from the same jet. The two cases with a spacing larger than this distance provided similar penetration and vortical structure of single, larger jets in crossflow. On the contrary, for a 5 diameter spacing no discrete vortices could be identified even at streamwise positions closer to the injection point. This is caused by an interaction between different CVPs. The opposite orientation of the vortices produced by adjacent jets resulted in a mutual cancellation (as illustrated in figure 2.21), with a consequent reduced overall vorticity generation and a faster diffusion in the flow. Ali's PIV results for streamwise vorticity show a faster vorticity dissipation in the reduced spacing case. Moreover, the wall-normal velocity contours show that as a result of less coherent CVP structures a more two-dimensional shock and flow structure downstream of the array are observed, which might positive for air-inlet applications [42]. Within the project group of which this thesis belongs an analysis of spacing influence on AJVG was performed and it will be discussed in the next section.

If jets are issued into a crossflow with a certain pitch or skew angle with respect to the wall surface, the resulting vortex system might be altered. An inclined injection can cause a strength unevenness between the two main counter-rotating vortices. This phenomenon was observed by Pearcy et al. [43]. They noticed that for a pitched injection above a certain skew angle, the CVP is replaced by a single persistent stronger vortex. This critical value is dependant on the jet velocity ratio, but

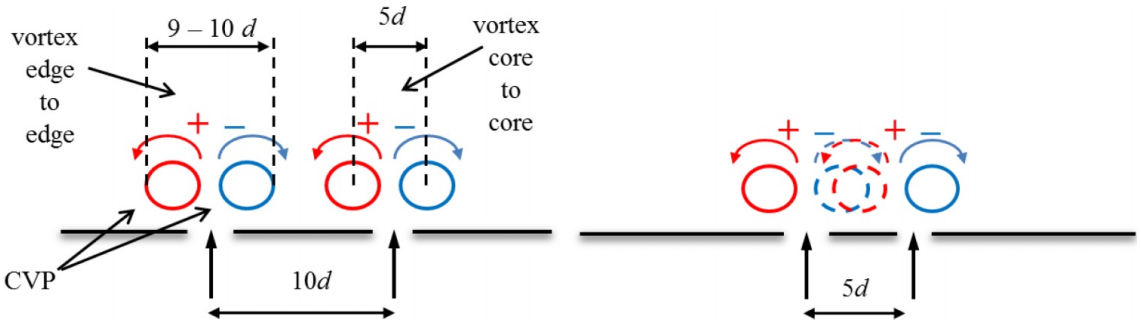

Figure 2.21: Schematic of the interaction of adjacent vortices for microjet arrays with two different spacing [42].

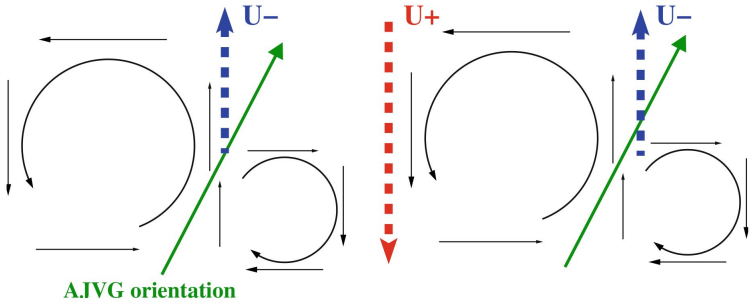

Figure 2.22: Inclined jet vortex generation [18].

in general adding skewness to the jet results in a strengthening of the main vortex. Souverein and Debiève [18] analyzed an AJVG array with an injection angle of 45° with respect to the wall and in a transverse direction of the main flow. PIV observation showed the different vortical structure for the generated CVPs. A weaker vortex was observed between the wall and jet, while the vortex on top of the jet resulted in an higher strength (figure 2.22). As the vortices are convected downstream, the weaker one is rapidly entrained and becomes lost in the resulting flow field [13]. Asymmetric vortices generated by an inclined jet are usually distinguished between primary and secondary vortex, according to their different strength. In case of reduced spacing the interaction between adjacent vortices issuing from different jets might lead to a net positive balance of their rotational component, in contrast with Ali's results [42] for transverse jets, where the interacting vortices have a comparable intensity.

2.3.2 Configuration parameters

Several design parameters affect AJVG systems efficacy, therefore an overview on some parametric studies will be here presented. Figure 2.23 shows a schematic of

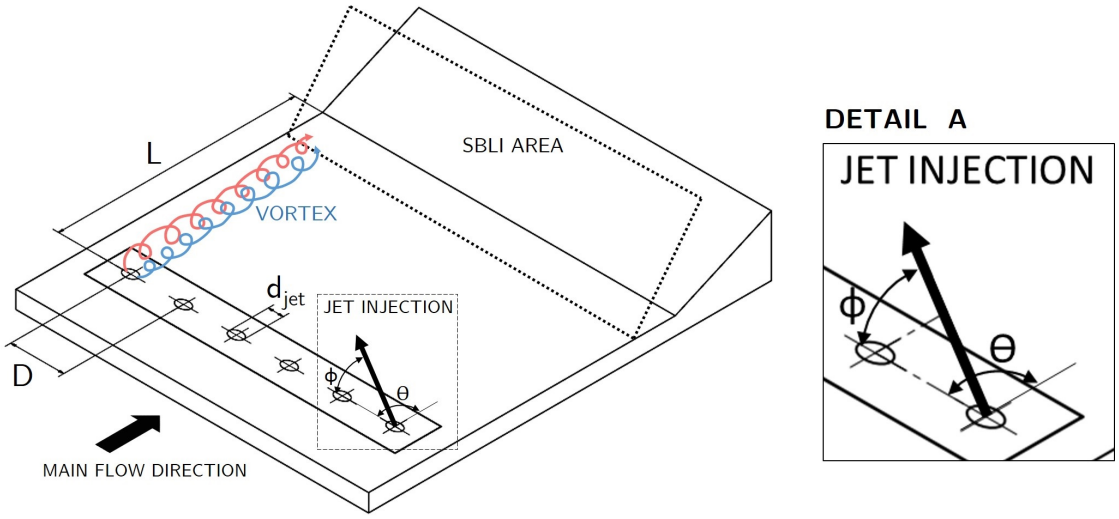

Figure 2.23: Schematic of main AJVG geometric parameters.

an AJVG system for SBLI separation control in a compression ramp, similar to the test case used within this project. The main geometric parameter indicated are: diameter of the hole d, development length between jets and interaction area L, pitch and skew angles of injection, ϕ and θ respectively and jet spacing D. Other parameters include jet conditions such as pressure and velocity levels.

Several studies have proved that an inclined injection is more effective in reducing separation regions. As mentioned earlier, introducing a skew component results in a vortex strengthening. On his first developments, Wallis [13] already saw the successful performance of inclined jets compared to transverse ones. A pitched injection with lower angles, introduces also less disturbance or no disturbance at all to the outer flow. Therefore the resulting bow shock formed upstream of the jets in supersonic cases is weaker [32]. A parametric study for a low-speed AJVG system conducted by Selby et al. [14], showed that decreasing the pitch angle ϕ resulted in a better performance for a skew angle of 90° and keeping the other parameters fixed. Vortices tends to remain closer to the wall surface and therefore energize more efficiently the lower deck. Within the same study, an optimal skew angle θ between 60°, for $\phi = 15°$, and 90°, for $\phi = 45°$, was found. Later Bray [16] performed a wider parametric study, confirming a similar trend for the optimal angles. However, he noticed that for all the different skew cases very low pitch angles ($\phi < 20°$) resulted in a vortex excessively close to the wall with insufficient height for a proper development. Bray extended his research also to high-speed cases (up to $Ma = 0.75$), showing that no significant changes in the optimal angles configurations was noticed from the low-speed tests. Various successful studies on AJVG applications for SBLI separation control later reported a typical configuration of 45° pitched jets with a 90° skew angle from the crossflow [17, 18, 32], therefore

the same configuration is used within this project. A later study from Szwaba [34] reports an improved configuration of $\phi = 30°$ and $\theta = 75°$ on the basis of a numerical optimization.

Assessment on jet diameter influence has also been performed in various studies. Wallis and Stuart [13] reported no significant influence for different sizes under transonic conditions, while Bray declares a linear growth in peak vorticity with increasing diameter at constant blowing pressure. A larger size for the same pressure conditions results in an higher mass flow rate [16]. An increased mass flow rate might translate in a larger disturbance introduced into the main flow, especially in supersonic conditions. Szwaba [37] observed, in a SBLI separation control system, that for a large injector diameter ($2mm \approx 0.4\delta_0$) increased flow unsteadiness was visible, especially for cases without longitudinal pressure gradient. Smaller jets (0.5 and $0.8mm$) instead provided a better stabilization and reduction of the separation area. For this reason Szwaba suggests the implementation of smaller jets with a diameter not exceeding a quarter of the boundary layer thickness for regions without significant acceleration and slightly larger value when a favourable pressure gradient is present after the interaction [37].

Being the counter-rotating vortex pair formation strictly related to the jet momentum, an higher injection velocity results in a stronger vortex formation [16, 14, 18]. Round jet penetration, especially in supersonic crossflow, depends strongly on the jet-to-flow momentum ratio ($J = (\rho U)_j/(\rho U)_\infty$) and to a lesser degree on air Mach number and incoming boundary-layer thickness [44]. An excessive penetration of the jet might result in a vortex formation above the low momentum region, undermining the energizing process. This possibility in AJVG configuration however is usually avoided by the typical inclined injection previously discussed. Moreover, since jet channels are usually straight, the maximum exit velocity is the sonic condition. An other factor that can influence penetration is the orifice shape. Penetration properties of non-circular jets will be discussed in the next chapter.

The previously considered parameters were properties only of the single jets composing an AJVG system. It is crucial to assess also other parameters linked to the overall installation. An effective development length between the vortex formation and the separation area is necessary to allow a full development of a vortical system. On the other side, a disproportionate distance could lead the vortices to an excessive dissipation and lifting from the wall while they are convected downstream to the interaction area.

Mutual interaction of the vortices is also relevant, therefore jet spacing affects the AJVG performance. This parameter was analyzed by Hinke [31] as part of the same project group of this thesis. Three different spacing (8, 12.5 and 16 mm) for an array of 1 mm diameter jets were analyzed. A corner ramp induced separation for a $Ma = 2.5$ flow was considered. Among the three spacing, the 8 mm case resulted

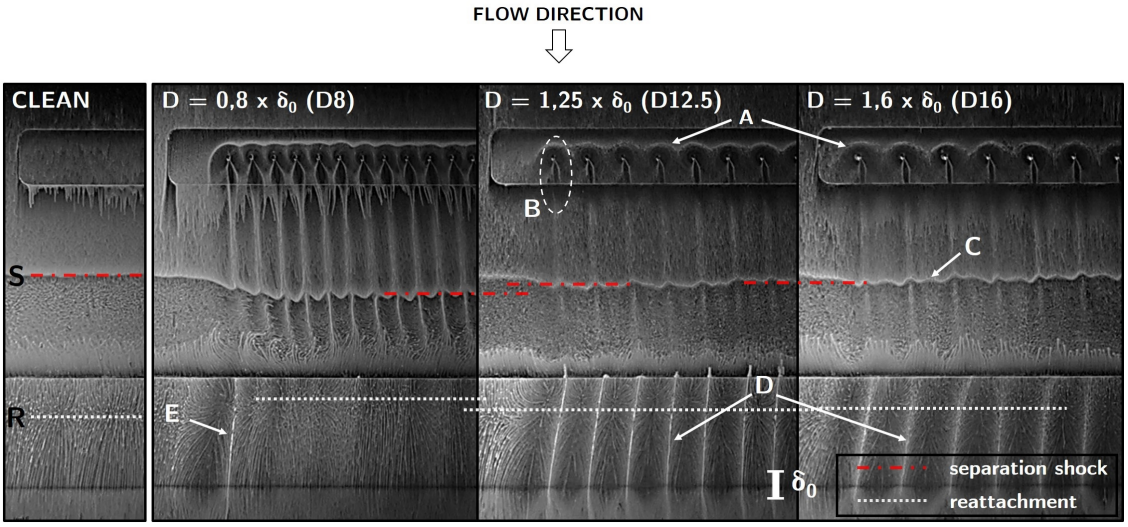

Figure 2.24: Oil visualization of the SBLI separation region with AJVG for 3 different spacings (8,12.5 and 16 mm) plus the reference clean case [31].

in a 27% reduction of the separation area and only of 11% for the larger spacings. Oil flow visualization of Hinke's results are showed in figure 2.24. It is possible to notice vortices trails downstream of the reattachment for the wider cases, probably due to a lack of interaction among the adjacent vortices which instead is present in the 8 *mm* case. Smaller spacing configurations are currently under testing in order to assess an optimal value for this parameter. The 8 *mm* spacing case has been taken as reference for the design of non-circular AJVG injectors of this thesis. Further details on the flow conditions and on the experimental setup will be given in chapter 4.

Lastly, an additional parameter will be shortly addressed here. Channel length of the jets in air-jet vortex generator systems is not mentioned in almost all the cited studies so far, probably because it is more likely assured a sufficient length for the flow to develop inside the channel. But if the ratio between the channel length L and the jet diameter D becomes small enough, some recirculation effects within the supply region might affect the penetration properties of the jet, especially in low-speed flows. This has been observed by Peterson and Plesniak [45], for a transverse injection in a low-speed crossflow with a an L/D ratio of 0.5. Two different supply conditions were tested and as can be seen on figure 2.25 different recirculating regimes within the supply chamber led to unequal penetrations of the jet into the main flow. Due to manufacturing requirements for the non-circular shapes designed within this thesis, the channel length of the reference model has been substantially reduced. This effect might negligible in our case with a sonic injection, however an assessment on its eventual influence will be made. This aspect will be discussed in the next chapters.

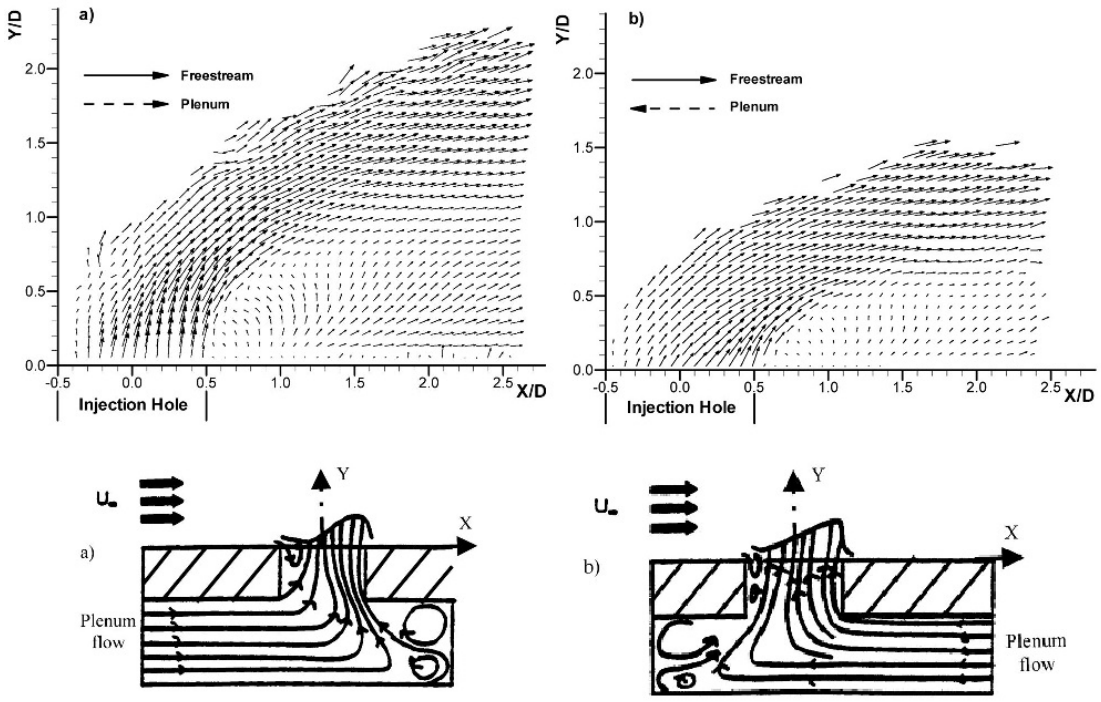

Figure 2.25: Influence of channel length to diameter ratio for two different supply conditions [45].

2.3.3 Non-circular AJVG

Air-jet vortex generator applications discussed so far are characterized exclusively by round jets. The main aim of this thesis is to examine possible influence of non-circular shapes for the jet orifices in AJVG, as there is a lack of studies on this aspect. Only few documented cases have been found in literature, which are here reported.

A direct comparison between circular and non-circular jets in AJVG for separation control over a transonic airfoil has been performed by Rao [15]. A circular jet and a rectangular jet (1.59 mm x 7.62 mm, Aspect Ratio $\approx$ 4.8) with approximately the same jet exit area, both with a 30° pitch and 60° skew angle, thus with a downstream component, were analyzed for different blowing pressures and three wall bumps to simulate a transonic airfoil as in [13]. A comparison of the shock position against trailing edge pressure for an 8% chord-length bump is showed in figure 2.26, where a larger shifting downstream is indicated for the rectangular case. Rao attributes this effect to an increased length of the orifice seen by the crossflow, which results in an increase in the vortices' diameter for the same mass flow rate. In a further comparison between the mentioned rectangular jet and a longer one (12.7 mm x 1.59 mm, Aspect Ratio $\approx$ 8) stronger vortices and thus a better performance are

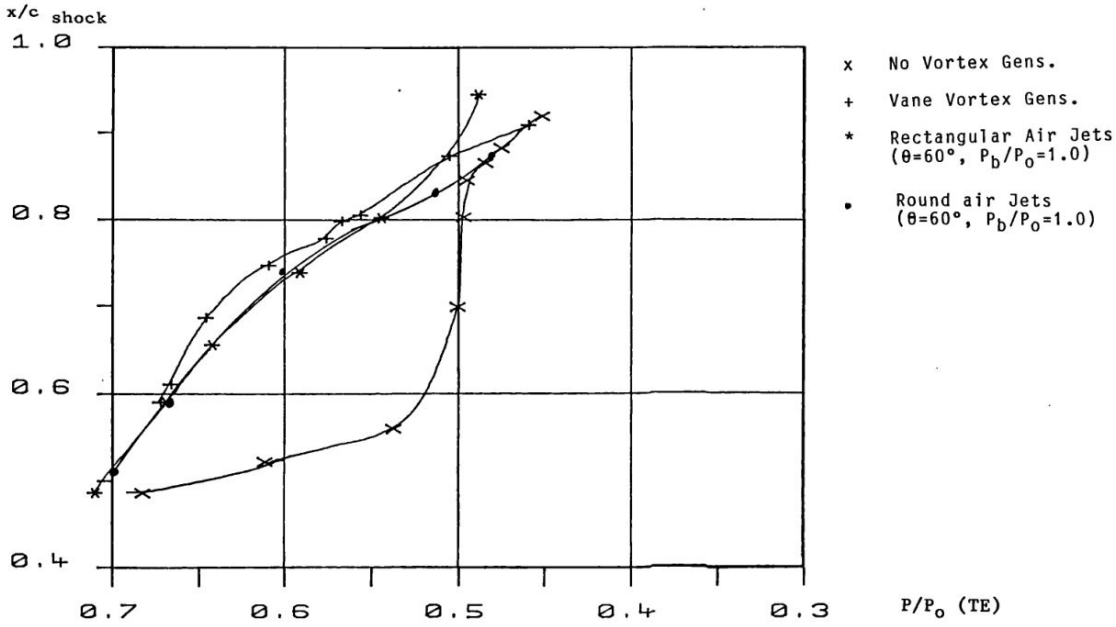

Figure 2.26: Comparison of shock position against trailing edge pressure for: uncontrolled case, vane-type VG, round AJVG and rectangular AJVG [15].

claimed by Rao. However this last result might be imputed to the increased mass flow rate and not directly to the geometry itself.

An other demonstration of rectangular AJVG application is given by Singh et al. [46]. Arrays of rectangular AJVG with an aspect ratio of 8 were applied on the blades of an helicopter rotor. An effective reduction of dynamic stall vortices and airfoil oscillation was accomplished with an array placed on front ($x/c = 0.12$). Jets were issued at a pitch angle of 30° and a skew angle of 60°, thus with a downstream component as suggested by Rao [15] and other studies. No comparison with a circular counterpart is provided.

A particular injector shape for AJVG is presented by Shun and Ahmed [47]. Jets presented an "exponential" nozzle configuration, characterized by a width and injection profile that both increase once by a factor of e. A minimum and maxium injection width of respectively 1.5 mm and 4.08 mm (1.5 x e) is given. In order to simplify their manufacturing, the exponential shape was discretized in 4 discrete rectangles with increasing width and injection length of 1 mm with a 0.2 mm spacing from each other (figure 2.27). Two velocity profiles issuing from the discretized holes were considered, one with the same increasing factor and one with a constant-blowing velocity profile. This profile was claimed to have an increase in penetration up to 40% more of a round jet. This configuration was implemented on a NACA 63-421 airfoil at 40 m/s, obtaining a noticeable increase in maximum C_l, with a

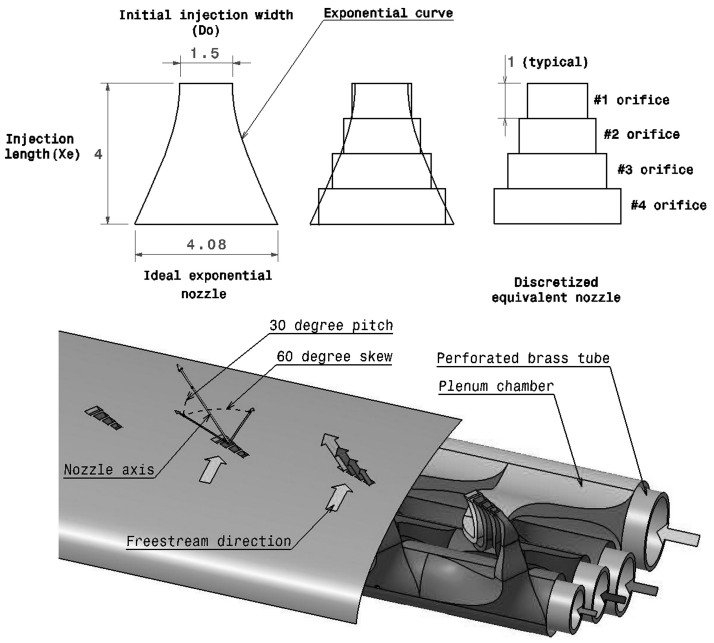

Figure 2.27: Exponential nozzle configuration and relative discretizaton (top). Nozzle array configuration on an airfoil (bottom) [47].

lower energy requirement for the incremental velocity profile compared to the uniform one. Also here no comparison with circular jets is performed.

No further relevant non-circular AJVG applications have been found in the literature. Therefore, the designing of the test cases of this thesis was made mostly based on general noncircular jets in crossflow studies, which will be reviewed in the next chapter. This analysis will focus mainly on two aspects of the jet interaction. First, penetration will be considered since a more effective momentum exchange between different decks is performed when vortices have a reduced tendency of lifting from the wall. Second, considerations on the shock formations ahead of jets for supersonic crossflow will be taken into account to see if some particular shape shows a weaker interaction and therefore a lower disturbance introduced by the resulting shock system. Other shape influcences that might increase the strength of the produced vortices will be taken into account

Chapter 3

Non-Circular Jets

This chapter is dedicated to non-circular jets in crossflow (JICF), with particular attention to the influence of orifices' shape on jet properties such as penetration, vortices strength, mixing characteristics and in general interactions with the main flows that might influence the effectiveness of Air Jet Vortex Generators systems for boundary layer separation control. Since the implementation of non-circular geometries for jets in supersonic crossflow lacks of relevant literature, an overview on subsonic non-circular JICF studies, which instead are more comprehensive, is also here first presented in order to assess the impact of shapes not described (or at least not extensively) in supersonic literature, despite the different flow conditions. A few cases of non-circular jets without crossflow will be also included to illustrate some particular shapes that might be of interest for the purpose of this analysis. Finally, a summary of shape influence is given with respect of the four cross section selected for this study. Since most of the literature on non-circular JICF refers to a transverse injection, additional effects caused by skew or pitch angles, such as the unevenness of vortex strength described in the previous chapter, are here only partially included.

3.1 Non-circular jets in subsonic crossflow

Jets in crossflow can be found in several applications. For each of them, some particular aspects of this flow interaction has to be accentuated. For example, better mixing capability or a deeper penetration might be required in fuel injection applications for burners while in other situation the opposite is preferred. This is the case of film cooling applications, where an improved performance in maintaining tolerable wall temperatures in region of high heat loads (e.g. turbine blades and vanes) is obtained when the injected coolant gas is kept closer to the surface. One way to enhance this feature was sought in the shape influences on jets in crossflow,

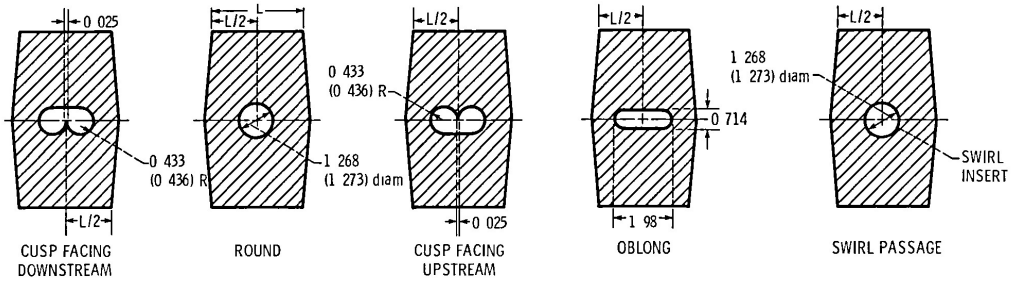

Figure 3.1: Schematics of the five shapes tested by Simon and Ciancone [48]. Flow direction from top.

therefore studies on non-circular jets applications have emerged. Since a similar condition might be beneficial for a better momentum mixing in AJVG applications, some results of these researches are reported here. It is worth noticing that in cooling applications avoiding excessive mixing is required, while in AJVG an enhanced recirculation favours the energization process. However, the vortices lift-off reduction properties of certain shapes that will be described can be advantageous in both applications.

In 1985 Simon and Ciancone [48] tested five different shapes for a 30° downstream inclined injector: a reference circular, an additional circular with a swirled insert, an oblong shape and two additional oblong with cusps, one facing downstream and one upstream (figure 3.1). Penetration characteristics for cold flow injection at different momentum ratios ($J = 0.53 - 6.2$) were obtained by means of flow visualization and results were compared to cooling performances obtained from an another study with the same configuration. From the results reported in figure 3.2, higher aspect ratios resulted in a noticeably lower penetration, especially the configuration without cusps. Moreover, between the two cusp shaped holes the downstream configuration showed an initial greater turning of the jet towards the surface, caused probably by the larger pressure drag created by the flat side, as the authors report.

Aspect ratio (AR) is defined as the ratio of the main crosswise dimension to the main streamwise dimension, therefore jets that cause a larger obstruction to the flow are characterized by an higher aspect ratio. Although some authors define this ratio inverting the two sizes, this definition will be used throughout the chapter to avoid any confusion.

A detailed study on the different vortices generation mechanisms which affect the lift-off characteristics of a transverse jet was conducted by Haven in 1997 [49]. Shape influence on lift-off characteristics of the counter-rotating vortex pair, here referred as kidney pair due to their shape, is discussed in this work, introducing the concept of a double-deck structure and of a second unsteady pair of either kidney or "anti-kidney" vortices. The considered hole geometries include two pair of elliptic and

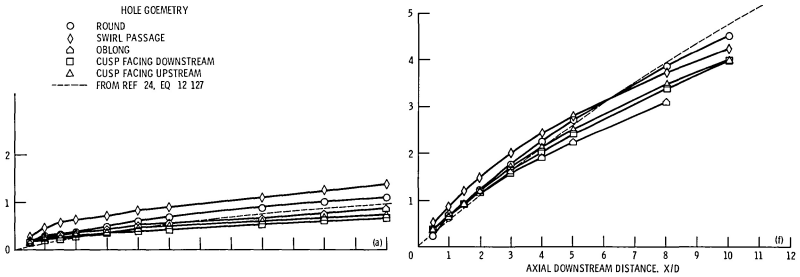

Figure 3.2: Jet centerline height as a function of axial distance for J=0.53 (left) and J=6.2 (right) from Simon and Ciancone [48]. Dotted line indicates a theoretical reference for circular jets.

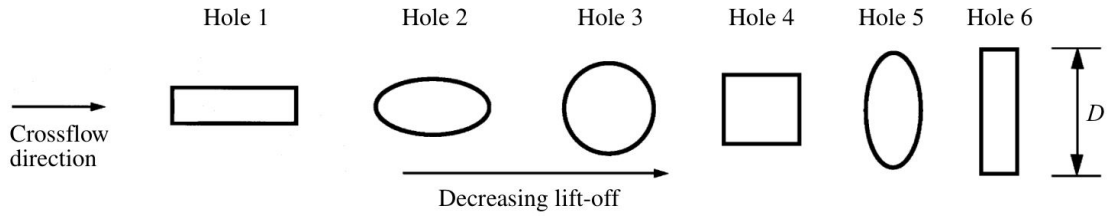

Figure 3.3: Lift-off characteristics of different hole geometries according to Haven [49].

rectangular injectors both in an high and low AR configuration, plus a squared and circular reference, all with the same cross section. Double decked structures and unsteady vortex pairs are linked with either sides, trailing edge or leading edge of the injector orifice, hence sharp edged geometries provide a more distinct view of these structures, which instead are less clear in round jets. For this reason a scaled version of the rectangular orifices were included by the author for in depth PIV and LIF (laser-induced fluorescence) analyses.

Since the two main vortices rotate in opposite directions, they induce an upward velocity into each other (figure 3.4). Vorticity that establish the CVPs is mainly issued from the sidewall boundary layer of the hole passage interacting with the main flow, therefore increasing the distance between the two main vortices reduces their mutually induced velocity. Similarly to Simon and Ciancone [48], Haven reports a decreasing lift-off with increased AR, thus an increased separation of the CVPs, as images show (figures 3.5, 3.6).

In these pictures it is also possible to observe the aforementioned double-deck structure. The lower deck is characterized by the two main "steady" vortices generated principally from the side vorticity plus some contribution introduced by the spilling vorticity from the leading edge corners. The upper deck, instead, is mostly influenced by a periodical shedding of the central portion of the leading edge boundary

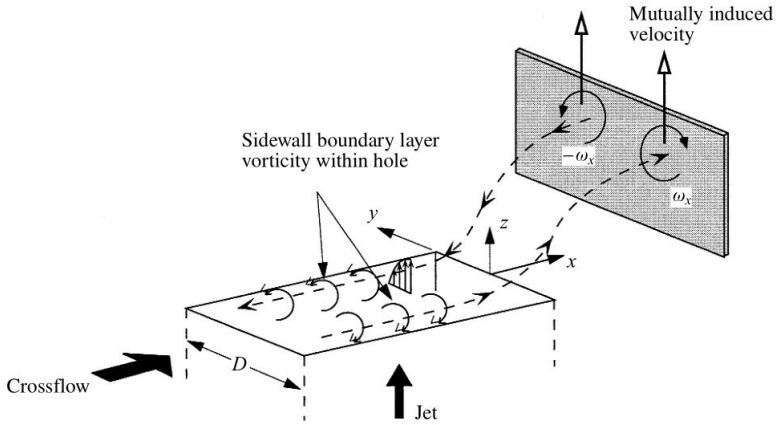

Figure 3.4: Kidney vortices formation and mutual lift-off induction [49].

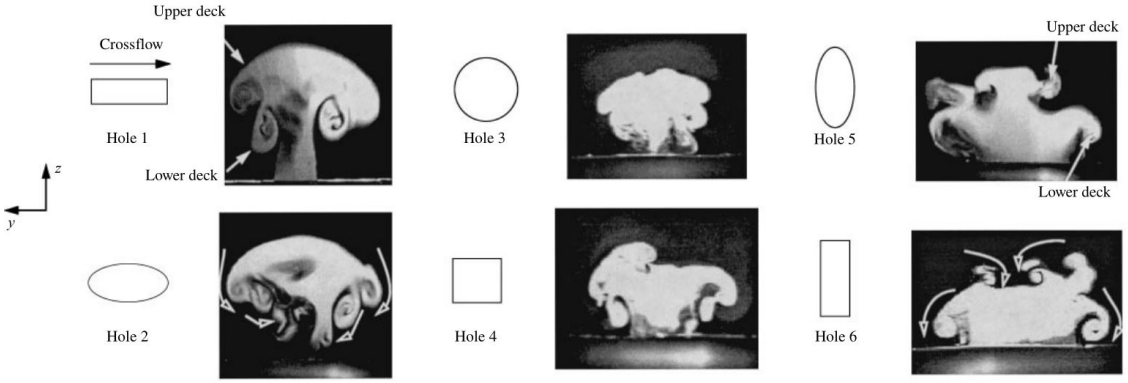

Figure 3.5: LIF images at the downstream edge of six different geometries. From Haven [49].

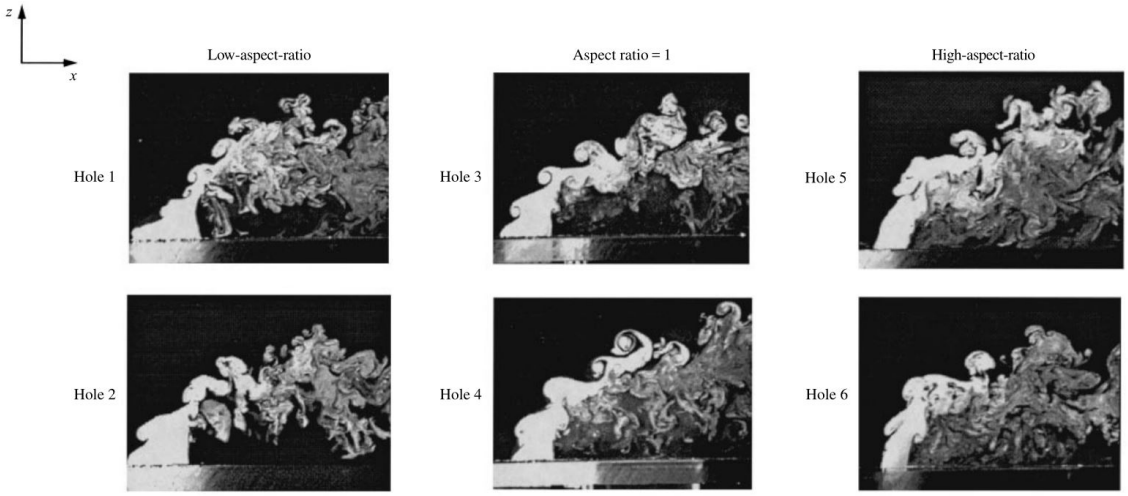

Figure 3.6: LIF images of jet trajectory along the centerline for six different geometries (Velocity ratio = 1.6). From Haven [49].

layer and in a similar manner from a warping caused by reverse flow in front of the trailing edge. In both regions either kidney or anti-kidney pair vortices originate, the first for low AR geometries and as well for squared and circular cases while the latter appear for higher AR. Kidney pairs rotate in the same orientation of the lower deck vortices, therefore the overall vortical system is enforced as well as the mutual induced lift-off velocity. Anti-kidney pairs, instead, rotate in the opposite direction and counteract the lower deck structure vorticity, thus their net balance determines the jet lift-off. The "deck" terminology should not be confused with the one introduced for the description of boundary layer in the previous chapter. More details on the formation of these vortical deck structures and their influence can be found in Haven's works [50, 49]. A comparison of the lift-off properties of the mentioned geometries is illustrated in figure 3.3. High AR rectangular injectors present a lower penetration than the elliptic cases, probably for an increased influence of leading and trailing edges due to its sharp corners. This study included only low velocity ratios ($VR < 2$), but higher values might mitigate the strong geometry influence reported here.

On this matter, Liscinsky et al [51] considered similar injector geometries but for an higher jet-to-mainstream flow momentum ratio of $J = 8.2$. Through PIV and mean concentration measurements of a methane tracer introduced into the flow they observed no significant difference on mean concentration trajectories for different shapes, although a similar, yet weaker, trend to Haven's research on AR influence on penetration can be observed. All the considered geometries presented similar turbulent mixing characteristics and turbulent fluctuations. Low AR orifices showed a different trajectory and stronger CVPs but a slower mass addition due to their longer axial length balanced this effect providing the same mixing capabilities of the remaining cases [51]. In general, shape influence seems to be mitigated from the high momentum ratio, but no detailed information on the vortex formation are given in this paper. It is worth noticing that in this study the jet flow was issued from a thin wall section ($L/D \ll 1$) therefore a reduced shape influence might also be linked to in-hole vortices formation [45].

A more recent and detailed study on non-circular JICF has been presented by Salewski et al [52] at low speed crossflow flow conditions: $0.1m/s$ crossflow and velocity ratio of 4. Both experimental verification, by means of simultaneous PIV/LIF measurements, and numerical simulation using large eddy simulations (LES), were performed to assess mixing and penetration capabilities of different geometries with the same cross section. In addition to the already studied elliptic shapes for different AR and the squared case, a diamond-shaped injector consisting in the same square rotated by 45°, thus with a vertex facing the flow, were analyzed (figure 3.7). A decreasing lift-off with increasing AR is observed also here for the elliptic cases, confirming the previously mentioned studies [48, 51, 49]. A lower penetration of the squared case compared to the reference circular in agreement with Haven [49]

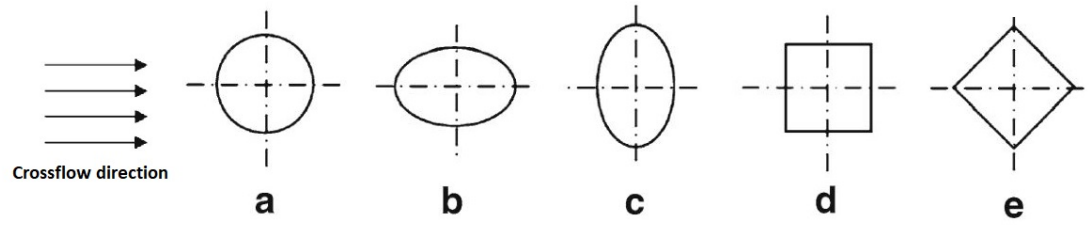

Figure 3.7: Different shapes considered in Salewski [52]. AR=1.56 for the elliptic case

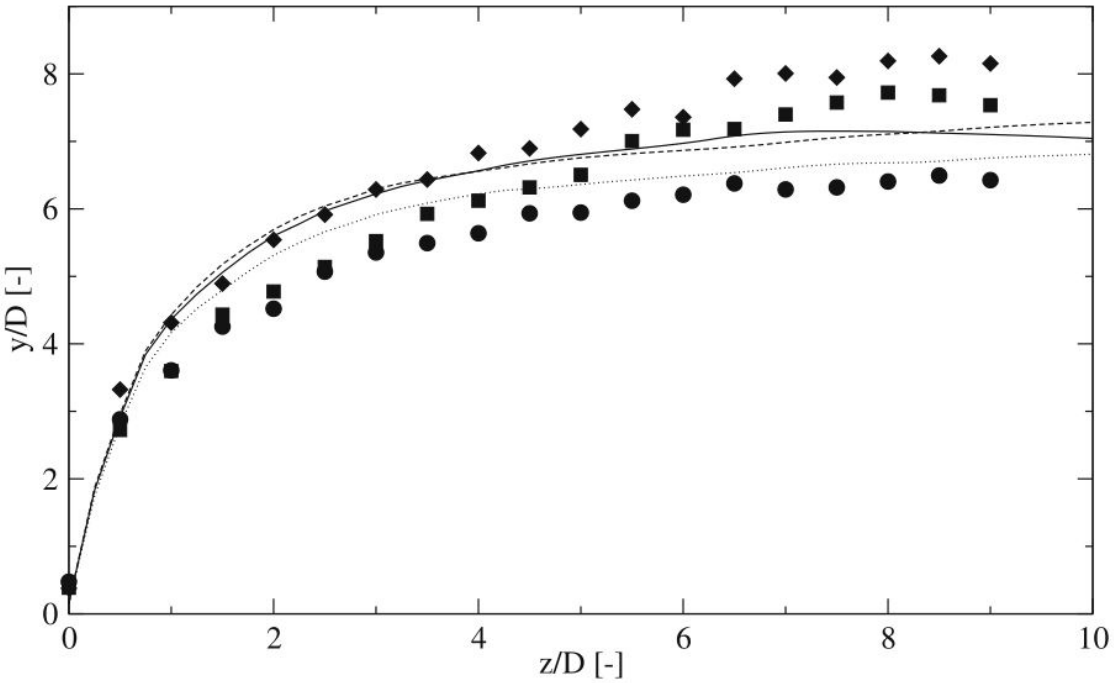

Figure 3.8: Jet trajectories defined by scalar concentration peaks for circular (straight line and circles), squared (square and dotted line) and diamond (diamond and broken line) injectors from Salewski [52]. Lines indicate numerical results while symbols are for experimental ones.

is reported as well. Regarding the diamond shape (45° rotated square), as it can be seen on figure 3.8, it gives an higher penetration than the squared case. This shows the effect of orifices' bluntness, which creates a stronger recirculation area and the additional turbulence produced affects negatively the penetration of the jet. As a main result, Salewski observed that the global mixing performance is enhanced for higher aspect ratio and blunt shapes.

Further assessments on the influence of sharp or blunt configurations can be found in some studies conducted by Gutmark, Ibrahim and Murugappan [53, 54]. Simi-

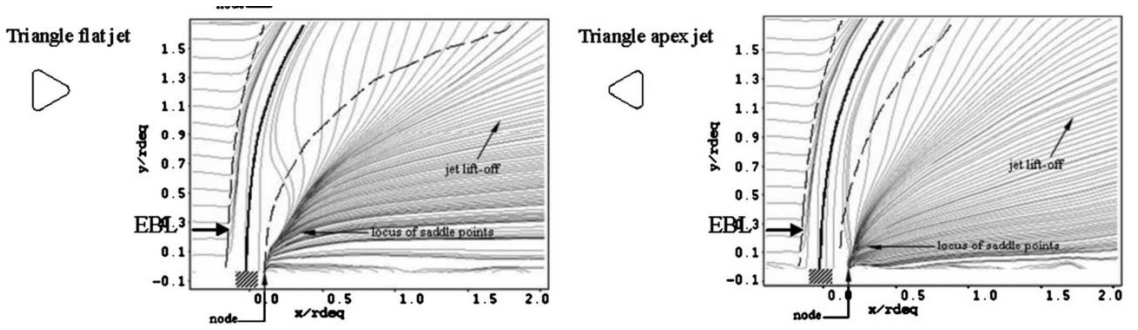

Figure 3.9: Streamline plot of average velocity on the xy plane for the two triangular configuration. From Gutmark et al. [54].

larly to the cases reported so far, their analysis on transverse jets in crossflow for different velocity ratios included, other than the circular reference and two "slot" configuration (one with AR=3.76, the second obtained with a 90° rotation), a triangular shape in two different orientation: one with a vertex facing downstream ("triangle flat") and the other facing upstream ("triangle apex"). The same recirculation and penetration trend described in other papers is verified here for the slot configurations, obtaining respectively minimum and maximum values of penetration and therefore more or less turbulent recirculation downstream of the jet for the high AR and low AR (90° rotated) configurations. In the same fashion as Salewski's comparison between squared and diamond injectors, for triangle apex injectors the vertex facing incoming flow reduces the disturbances while the triangle flat configuration, as a consequence of a larger blockage, presents a larger spreading of the jet, as can be seen from figure 3.9. In these plots the solid lines indicate the jet centerline and the dashed lines indicate the windward and leeward boundaries at 40% of the maximum jet velocity. The edge of the incoming boundary layer is also indicated.

However, some discrepancies on the presented data appears since on a previous publication [53] the flat triangle is claimed to have the lowest penetration (for velocity ratios, of 2 and 5) while a latter one [54], with the same experimental setup but for slightly higher velocity ratios (VR=3.2 and 8), states that a minimum value is obtained with the high AR slot configuration.

A common interesting detail of both researches is the effect of a decreasing area in the flow direction ($dA/dx < 0$), such as for the triangle flat. In these cases, the main flow encounter a larger obstacle which however do not have further "obstructions" behind as the area decreases towards the apex, therefore a spanwise spillage at edges of the nozzle geometry is observed. This causes an increased local blockage which affects the recirculation leeward of the jet and consequently its lift-off capacity [54]. This phenomenon can be observed in figure 3.10.

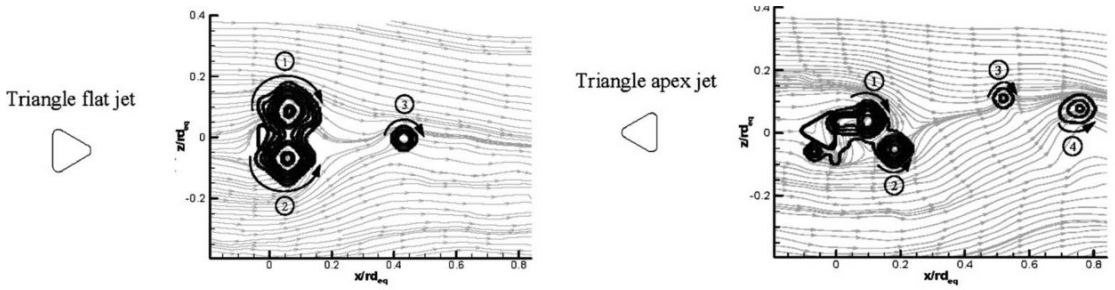

Figure 3.10: Vortex identification in the xz-plane from instantaneous streamlines for the two triangular cases. From Gutmark et al. [54].

In the attempt to obtain an effective scaling of elliptic jet trajectories, as usually performed for round jets despite the absence of a general solution, Lim et al. [55] examined five different elliptic injectors with aspect ratios varying from AR=0.3 to AR=3.0. The data used were from a previous research [56] in which they verified the kidney/anti-kidney structure described by Haven [49]. The usual trend of a larger bending of the jet towards the wall surface as AR increases was confirmed by their investigation. However, a satisfying scaling law could not be find due to a deterioration of the collapsed scaled trajectories as the elliptic jet geometry diverges further away from the circular shape.

Along with elliptic injectors, rectangular geometries have been subject of interest in several papers. In 1979 Weston and Thames [57] investigated the effect of an AR=4 rectangular injector for a streamwise, nozzle major axis parallel to freestream, and blunt, nozzle major axis normal to freestream, configurations for different pitch angles. In general, vortex spacing was observed not to be substantially affected by the pitch angle while higher vortex strength is present for increasing angle, as the jet interacts more intensely with the crossflow. The streamwise configuration showed similar penetration and vortex strength properties as circular injectors from other studies, while the blunt nozzle exhibited a significant reduction for both properties. Overall, blunt configuration was characterized by different vorticity distribution in both extent and magnitude.

Skew angle influence of rectangular injectors has been already mentioned in Rao's AJVG configuration [15] described in section 2.3.3. More extensive studies on this parameter were presented by Zhang in the late 1990s [58, 59]. LDA measurement for an AR=5.1 rectangular jet were used to better analyze vorticity properties for different pitch/skew angles combinations. As a first result, rectangular jets featured an increase of 63% in the maximum vorticity at the farthest measurement location for the non-skewed case, compared to a round jet with the same cross section, retaining however the same vortices shape and size. Among the different cases tested, skew angles between 45° and 90° showed similar properties, with an optimal result for

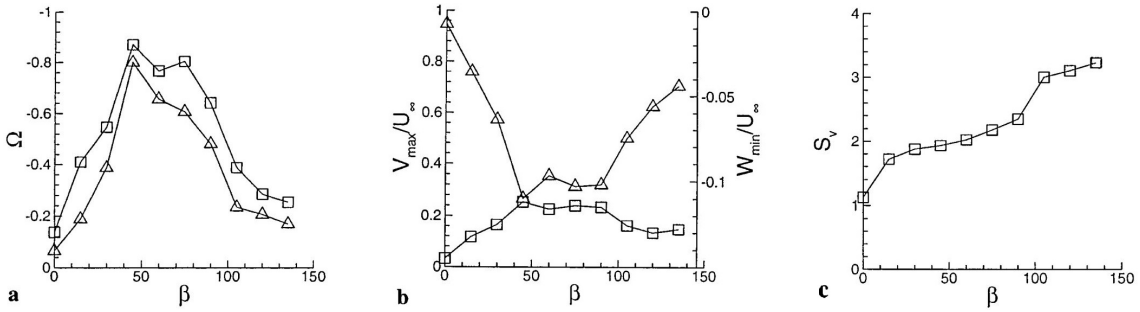

Figure 3.11: (a) Peak vorticity □ and main vortex center △ (at x=10D). (b) Maximum spanwise velocity □ and minimum transverse velocity △. (c) Size of the vortex S_v. From Zhang [59].

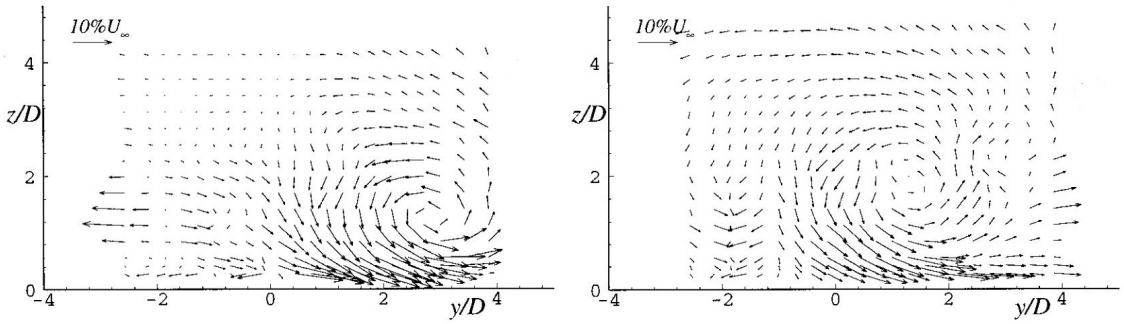

Figure 3.12: Velocity vectors for VR=1 injection at x= 20D for a 45° skew angle, at 30° pitch (left) and 60° pitch (right). From Zhang [58].

the 45° case. This can be seen in figure 3.11, where different vortices properties as a function of the skew angle β in a transverse plane located at $x = 10D$ from the injection point are reported. Plot (a) indicates the peak streamwise normalized vorticity Ω and the center of the main vortex, plot (b) shows maximum spanwise velocity and minimum transverse velocity and plot (c) gives the size of the vortex S_v, which is an empirical parameter defined in Zhang's paper as a function of the circulation level Γ and mean vorticity Ω_m. As discussed for skewed and pitched injections for AJVG in section 2.3.1, the generation of a single main longitudinal vortex instead of the CVPs for a non-skewed injection is evident in Zhang's results. Velocity vectors at a transverse plane for a 45° skew injection at two different pitch angles show this feature (figure 3.12).

In addition, an increased pitch angle results in a larger separation bubble in front of the jet exit. Velocity ratio also concurs in this effect. Oil flow pictures of this separation region from Zhang [58] can be seen in figure 3.13. For VR=1 and pitch angles under 45°, the author observed that the generated main vortex is embedded inside the boundary layer, therefore this condition might be beneficial for AJVG

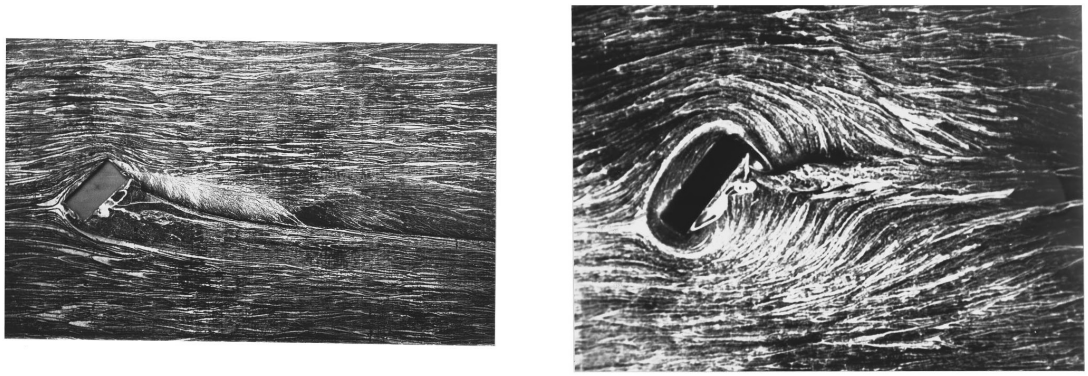

Figure 3.13: Oil flow visualization of the separation bubble downstream of a 45° skewed rectangular jet for: VR=1 and 30° pitch (left), VR=2 and 60° pitch (right). Pictures from Zhang [58]

.

applications.

Direct numerical simulations on squared jets in subsonic crossflow have been performed both by Sau et al. [60] and Maidi and Yao [61]. The latter study considered also a jet pair and their mutual interaction for different distances. Experiments and numerical simulation on an array of six squared injectors were presented by Ajersch et al. [62]. These studies are here mentioned only for completeness in the overview on non-circular jets in subsonic crossflow, however they either do not add further information on shape influence that has not been already discussed in this section or do not provide comparisons with round jets.

3.2 Non-circular jets in supersonic crossflow

The development of efficient supersonic combustion ramjet engines prompted interest in achieving rapid mixing of fuel with the main stream. As a consequence of its supersonic nature, the flow within the combustor chamber of a scramjet has a residence time of the order of milliseconds, therefore improved penetration and mixing capabilities with minimum total pressure loss are required [63]. One of the possible solution considered to improve such properties has been found in the implementation of non-circular geometries. Gutmark et al. [64] had already observed in 1989 the higher spreading rate of supersonic free jets characterized by elongated nozzles. Increased mixing capabilities of different injector shapes have been discussed in the previous section for subsonic crossflow conditions but the need of a better understanding of this feature for a supersonic main flow motivated the few studies reported here. A sonic injection was performed in all studies, except when

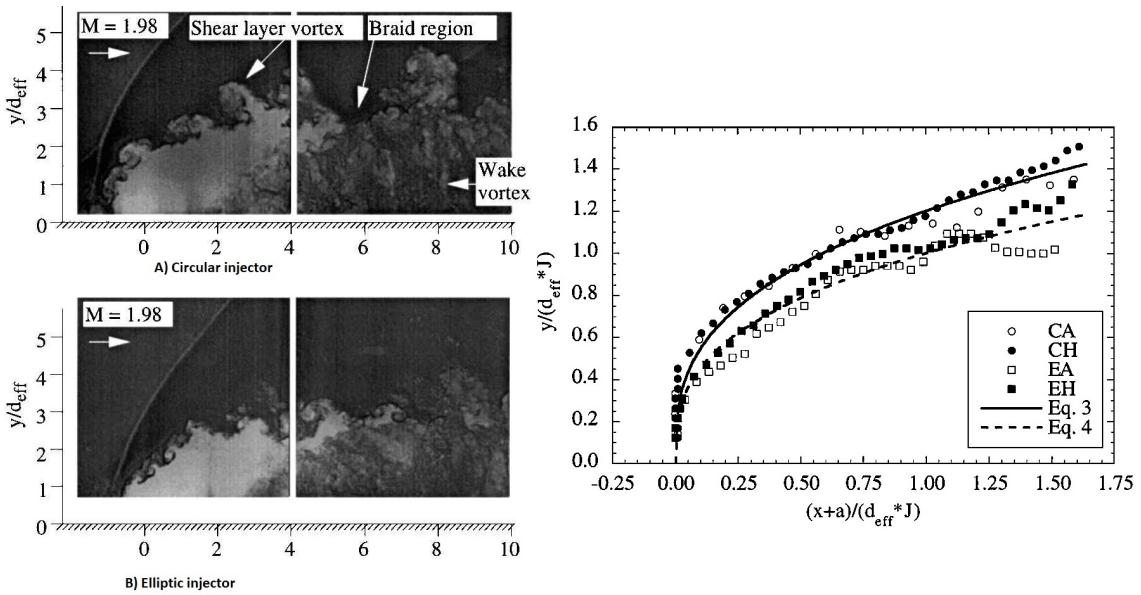

Figure 3.14: Left: side-view images of the two different injectors. Right: penetration data for all injection conditions (C=circular, E=elliptic, H=helium, A=Air). The two lines are power law curve fits of the data. From Gruber et al. [66].

noted.

Investigation on elliptic injectors for a Mach 1.98 free stream were conducted by Gruber et al. [65, 66]. An experimental comparison between a low aspect ratio elliptic (AR ≈ 0.25) and a reference circular geometries was performed for a transverse injection with $J = 2.90 - 2.93$ using planar Rayleigh/Mie scattering. While in their first study from 1995 [65] no significant differences in transverse penetration was reported, further statistical analysis from 2000 [66] actually suggest a 20% reduction for the low AR elliptic geometry. Tests were performed both with air and helium injections, showing similar results in the near field. Instantaneous side-view images for the circular and elliptic air injections and a plot of penetration data are showed in figure 3.14. The penetration boundary is here defined as the 90% of the average freestream intensity downstream of the bow shock.

In both studies, Gruber et al. observed a 25% increase in lateral spreading for the elliptical injector compared to the round jet which the authors claim is linked to the axis-switching phenomenon characteristic of non-axisymmetric injectors (further details on axis-switching in the next section). Top-view Mie scattering images for the two shapes can be seen in figure 3.15. The larger spreading is clearly visible in the elliptic case and, although less observable, the bow shock appears more attached to the elliptic injector case probably as a consequence of the much larger curvature of the edge.

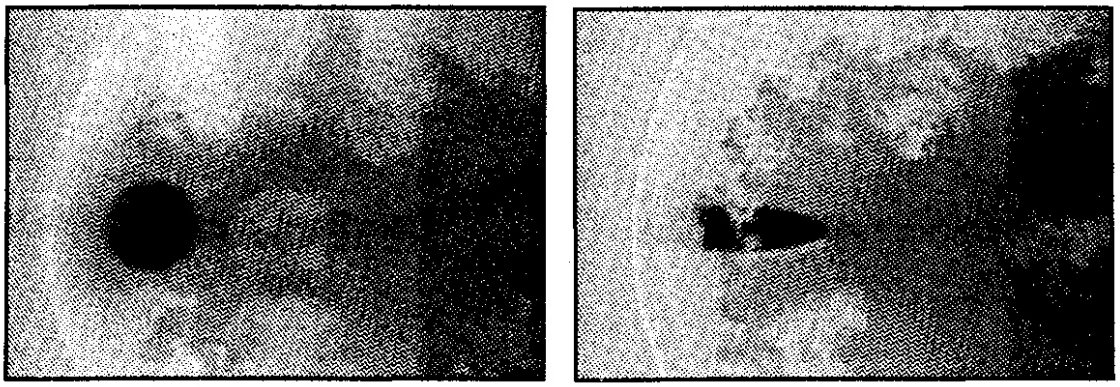

Figure 3.15: Top-view Mie scattering images of circular and elliptic injections. From Gruber et al. [65].

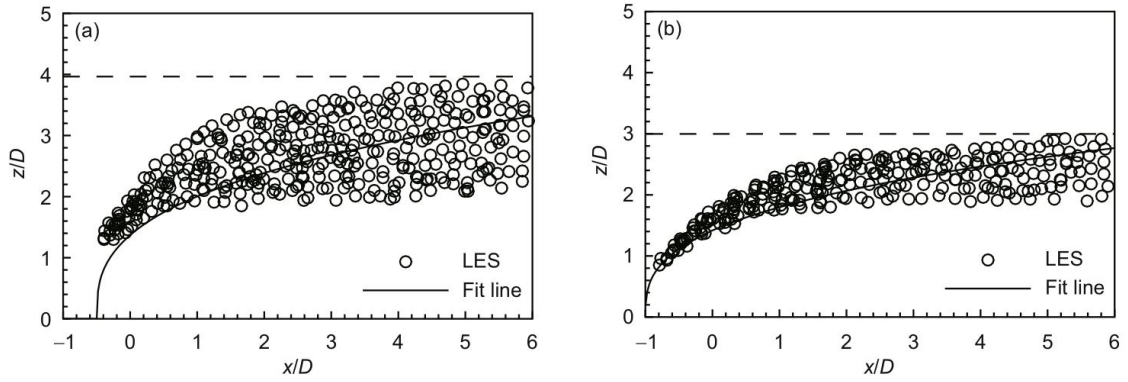

Figure 3.16: Jet penetration profiles for circular (left) and AR=0.25 elliptic (right) injectors. From Wang et al. [67].

Large eddy simulations of the same geometries for a Mach 1.6 crossflow were recently performed by Wang et al. [67]. A 25 % lower penetration for the elliptic case was registered, confirming Gruber's result. A narrower penetration band was also observed (figure 3.16, where the circles indicates the cores of the eddies). This last result is addressed to the different shear layer vortices produced in the two cases, with an higher deformation of the shock structures in the circular case. Numerical schlieren visualization by contours of density gradient $\|\bar{\rho}\|$ in the y/D=0 plane are showed in figure 3.17. Round jet presents a stronger bow shock, however a reflected shock and additional local shock waves characterize the elliptic injection. It is interesting noticing the discording results for subsonic and supersonic conditions. While low aspect ratio elliptic injectors exhibit an higher penetration than circular counterparts for a subsonic main flow, these studies in supersonic conditions display an opposite situation. This discrepancy might be attributable to the various shock structures (e.g. reflected shock in figure 3.17) that appear in the elliptic case.

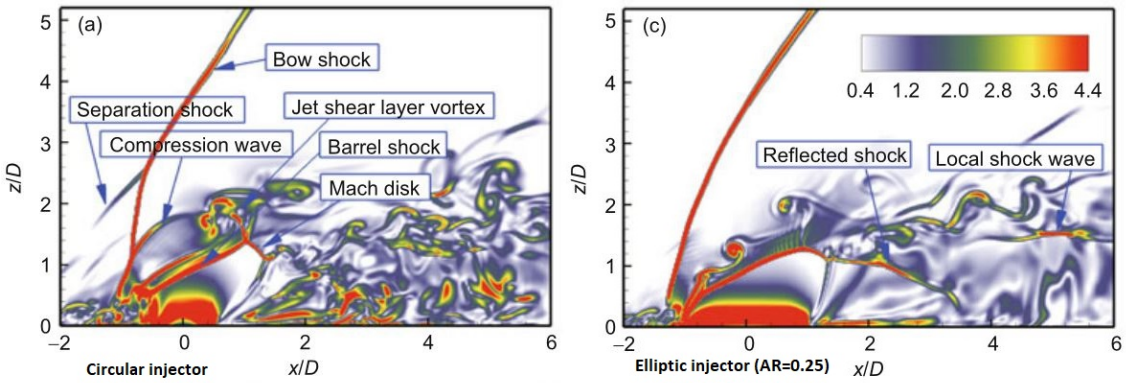

Figure 3.17: Numerical-schlieren visualization by contours of density gradient $\|\bar{\rho}\|$ in the y/D=0 plane. From Wang et al. [67].

As discussed in the previous chapter, excessive disturbances induced by the jet obstruction to the main flow and consequent stronger bow shock generation might induce a further separation ahead of the jet and cause an increased total pressure loss [32]. To reduce these effects, sharp edged injector geometries have been successfully applied in supersonic conditions.

A first example is provided by Barber et al. [68] which tested a wedge-shaped injector for a Mach 3 airstream and compared it to a transverse round jet. Helium injection was used to evaluate the achieved mixing. The elongated wedge-shaped injector presented an half-angle of 7.35°, with the apex oriented towards the incoming flow. As can be seen from the surface flow visualization in figure 3.18, although the bow shocks seems to have a similar strength from their shape, in the wedged configuration no upstream boundary layer separation zones are visible since the formed shock is attached to the injector apex. Based on helium concentration measurements, overall penetration based on the lowest perceivable fuel concentration from the measuring equipment was found to be 42% larger for the wedge geometry. "Core penetration", which was based on the position of the local concentration maximum, increases by 64%. In general, the wedge-shaped configuration shows significant improvement in penetration characteristic and induced disturbances to the main flow.

Notwithstanding the improved performance, Tomioka et al. [69] suggested that the round-shaped back of the wedged configuration could cause an excessive separation in the wake of the jet and the resulting low-pressure condition in the separated area might introduce intensive disturbance. Therefore, a diamond shaped injector with a 15° half angle corner in the flow direction was investigated in their research for the same Mach 3 crossflow condition. Along with transverse injection, pitched and skewed configuration were considered. Penetration height results were normalized with an effective diameter D_{eff} which is a function of the orifice area and the discharge coefficient. For the same condition reported by Barber et al. [68], the nor-

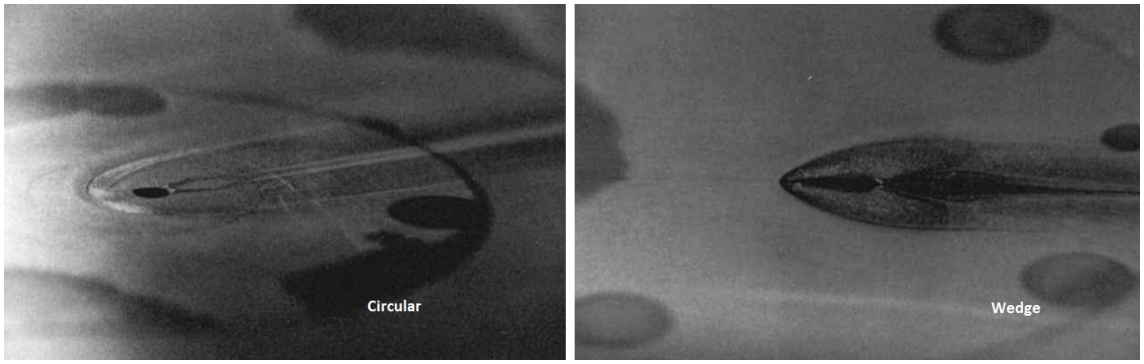

Figure 3.18: Surface flow visualization for a sonic transverse injection in a Mach 3 crossflow for a circular and wedge-shaped injectors [68].

malized penetration height was found to be about 200% larger than the reference circular case, thus providing better results than the 42%-64% increase for the aforementioned wedged shape. Oil flow visualizations for two different momentum rates in figure 3.19 show an actual stronger bow shock for the diamond shape due to the extremely larger penetration and consequent obstruction, although also in this case the resulting shock is attached to the injector vertex. Moreover, for low dynamic pressure injections ($J = 0.3$) separation ahead of the jet and wake disturbances for the diamond injector are no longer visible, in contrast to the circular case in which they are still visible. Penetration was observed to increase with downstream pitched injection as a consequence of a weaker interaction with the incoming flow (and consequently weaker shocks), but more interesting is the substantial increase obtained with a 15° skew angle for the 60° pitched injector (figure 3.20). Further skewness increments caused excessive interactions with the main flow and separation ahead of the jet as it acts more like a blunt obstacle.

Other evaluation on the same diamond configuration were performed by Bowersox et al. [70]. An overall reduced total pressure loss compared to the circular case and even lower losses for increasing pitched angles was confirmed. They showed that within certain injection pressure and inclination conditions the shock formed ahead of the jet remains attached, but exceeding certain critical conditions a detached shock, which separate the incoming boundary layer, and a lambda shock structure occur.

3.3 Non-circular jets without crossflow

Different behaviours of non-circular injectors are inherent on their geometric configuration. Manifestations of particular mechanisms are not clearly visible in the complex interaction of a jet with an incoming main current, while a better in-depth

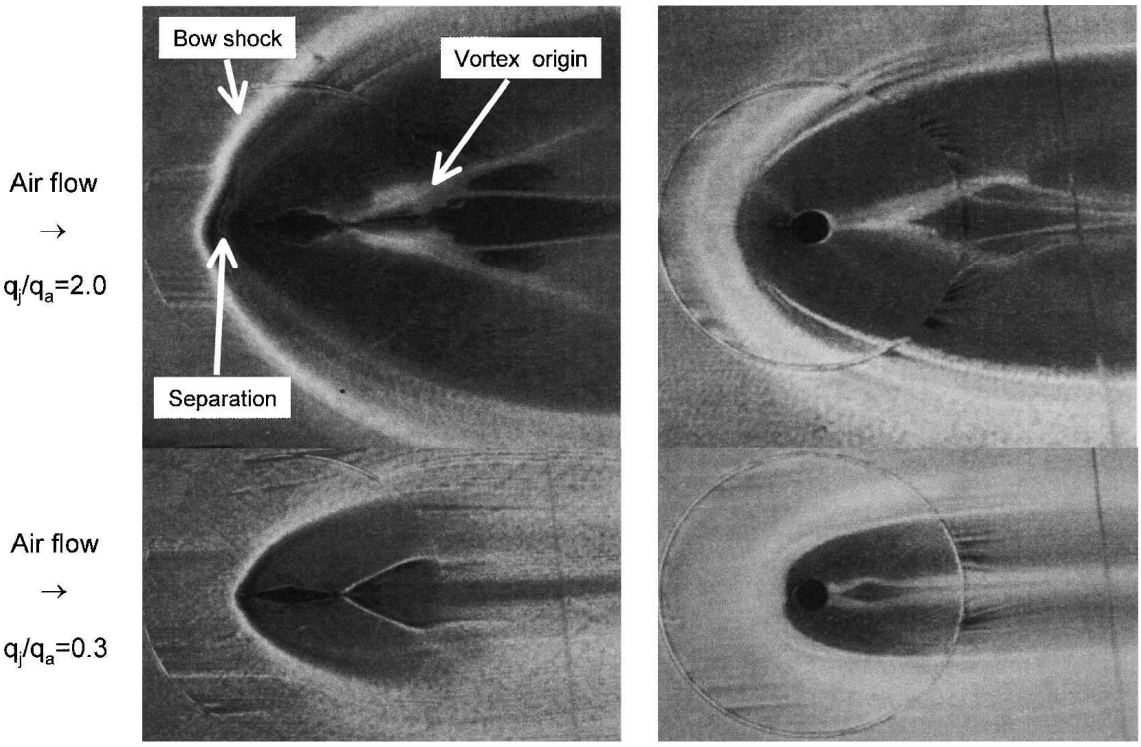

Figure 3.19: Surface flow visualization for a transverse injection in a Mach 3 crossflow for a circular and a 15° half angle diamond injectors at two different momentum ratios [69].

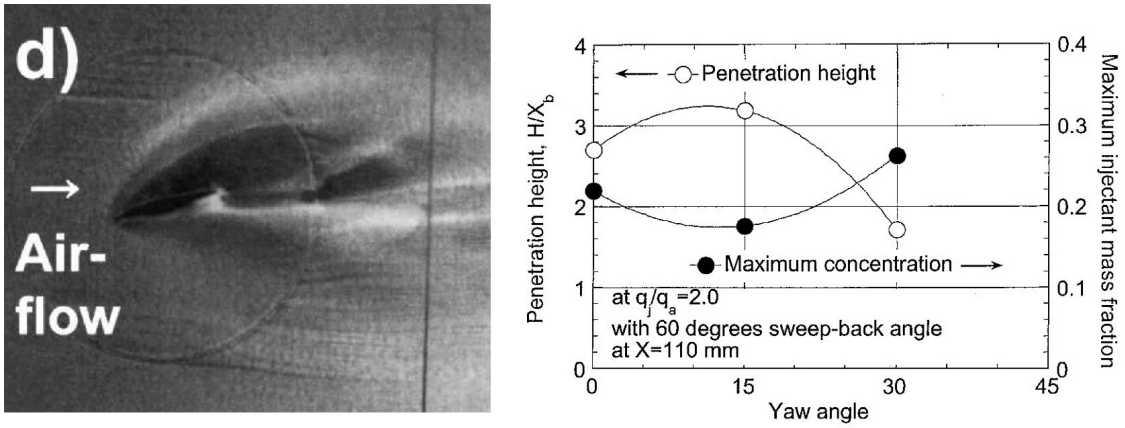

Figure 3.20: Left: surface flow visualization for the 15° skewed/60° pitched diamond injector. Right: penetration height and maximum concentration data for different skew angles [69].

description is possible when flow is injected in quiescent air. A common phenomenon in elongated nozzles such as elliptic ones is axis-switching. It emerges from a different spreading rate along the principal axes of a non-axisymmetric injector. More specifically, in case of elliptic injectors, the minor axis exhibit a larger spreading rate compared to the major one and for this reason at a certain axial position from the injection point, dependant from the geometry and the injection conditions, the minor axis spreading becomes larger than the initially wider distribution on the major axis, causing the so called axis-switching. The spreading boundaries at a certain axial location of a turbulent jet are commonly defined as the spanwise locations in which the mean velocity magnitude is half of the respective centreline one. Observations of axis-switching phenomena in an AR=3 elliptic nozzle were conducted by Schadow et al. [71] for subsonic, sonic and supersonic underexpanded jets ($M_j = 0.15, 1, 1.3$). For subsonic and sonic conditions the observed spreading rates of the minor axis were quite similar, with only a slight upstream shift of the switching point for the sonic case ($x/D_e \approx 20$ instead of $x/D_e \approx 24$). Surprisingly, in underexpanded condition the minor axis spreading rate was doubled from the sonic case, resulting in a switching point at only $x/D_e \approx 3$. Mean velocity contours of the two axis and visualization of the underexpanded reacting jet are showed in figure 3.21. This characteristic, especially for the supersonic injection, increases significantly the total mixing and entrainment rate of elliptic jets relative to the circular one. The authors link this behaviour to the presence of altered stability characteristics due to additional azimuthal modes, not present in the circular case, which describe the variation of disturbances in both amplitude and phase around the jet perimeter and increase the distortion of the different eddies formed along the two axes, with a growing influence for higher injection Mach numbers.

Gutmark et al. [64, 72] extended this study with a series of hot wire anemometry and PLIF measurement, the latter for both cold an reacting flows, introducing additional shapes. Geometries with sharp edges were compared to the circular and elliptic cases. Although a rectangular AR=3 injector manifested slightly lower spreading rate than the elliptic case with same aspect ratio [64], the sharp vertices were found to reduce the coherence of jet's large-scale structure. PLIF measurements confirmed the beneficial effect of the introduction of small-scale turbulence generated at the corners combined with the larger coherent scales generated at the flat sides in the mixing process for combustion systems. Comparison between squared, equilateral triangular and isosceles triangular with a 30° top vertex showed that this fine-scale mixing difference across the jet cross section was enhanched for smaller corner angles [72]. Increased mixing performance for a squared jet was confirmed also by Quinn [73].

In order to provide a proper comparison of the turbulent mixing characteristics of a wide range of different nozzle shapes within the same test conditions, Mi et al. [74] tested nine different injector geometries for a jet Reynolds number of $Re_d =$

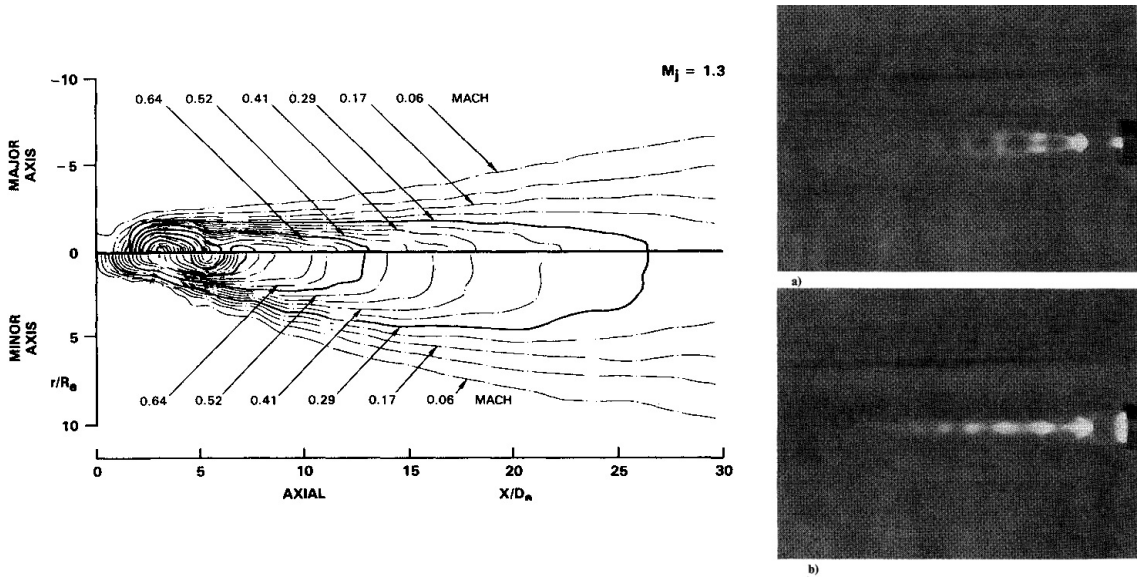

Figure 3.21: Left: mean velocity contours for an underexpanded reacting jet. Right: visualizations of minor (a) and major (b) axis for the same jet. From Schadow et al. [71].

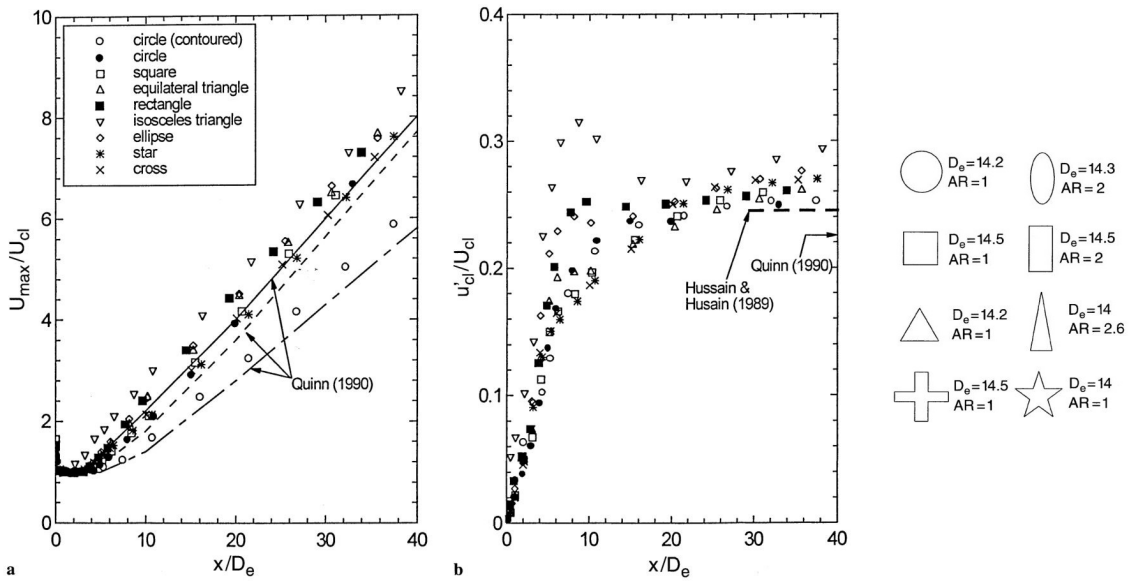

Figure 3.22: Centreline mean velocity variation (left), centreline velocity fluctuations variation (middle) and geometric configurations (right) from Mi et al. [74].

15000. The jet Reynolds number was based on an equivalent exit diameter which has been kept almost constant for all nozzles. Centreline mixing characteristics for the considered shapes were obtained through hot wire anemometry. Geometric characteristics of the considered injectors and centreline variations of both mean velocities and fluctuations are reported in figure 3.22. In general, all non-circular configurations show an higher decay rate than the round jet in the near field ($x/D_e < 10$). Among all the investigated jets, the isosceles triangle appears to produce the greatest mixing rates and the lowest penetration. In this section only some relevant AJVG related jet properties have been discussed. For more general informations on shaped injectors, a comprehensive overview, up to its publication, on flow control with non-circular jets has been published by Gutmark and Grinstein in 1999 [75].

3.4 Summary and test case definition

Throughout this chapter, two main geometrical characteristics appeared to influence the behaviour of a jet in a crossflow: aspect ratio and sharpness. As regards aspect ratio effects in subsonic conditions, it has largely been proven that for the same cross section area and same injection properties, higher aspect ratios provide lower penetration characteristics and larger wake disturbances, as they generate a wider obstacle to the incoming main flow [48, 49], even if some studies claim that this penetration difference could be mitigated for high jet-mainstream momentum ratios [51]. Different lift-off mechanism have been linked to the generation of either co-rotating or counter-rotating additional vortex pair in a so-called double-deck structure, introduced by Haven [49]. In supersonic condition instead, observation on low aspect ratio elliptic injectors actually showed an opposite result with a shorter penetration compared to a round jet [66, 67], instead of the expected higher value that would result in a subsonic crossflow [56]. However, no sufficient data on aspect ratio influence in supersonic flows was found, especially for high aspect ratio geometries. Therefore a more comprehensive study on various AR could help in establishing some sort of trend. In all flow conditions, despite the different penetrations, elongated nozzles presents larger spreading and mixing capabilities [58, 59], caused by the introduction of additional azimuthal instability modes [71, 64]. The second fundamental geometrical characteristic is the sharpness of the orifice. Its effect can be further subdivided in two properties. First, independently of the orientation, sharp corners introduce finer scale turbulence, improving the mixing capabilities from the jet. Larger scale turbulence emerging from long edges combined with the small scales emerging from corners resulted beneficial in combustion environments, although the overall coherence of large scale structures might be reduced [64, 72]. Second, certain orientations of sharp edges in respect to the main flow affect the introduced disturbances and total pressure loss. In particular, a sharp edge facing upstream provide beneficial effects in both subsonic [52, 54] and supersonic conditions. In

this second case, drastic improvements have been obtained for wedge-shaped [68] and diamond-like geometries [69, 70]. The resulting bow shock of the jet/crossflow interaction can sometimes remain attached to the leading edge, opposed to the detached conditions of blunt injectors and recirculation region, especially upstream of the jet, are substantially reduced or even removed under certain inclination and injection conditions. This results in a lower total pressure loss and overall reduction of introduced disturbances, with up to 200% increase in jet penetration compared to a round jet [69].

For AJVG applications a reduced penetration and consequently a lower lift-off of the produced vortices might emphasize the momentum exchange in the boundary layer energization process. Furthermore, a reduction in total pressure loss and in the introduced disturbances from the jet-crossflow interaction could ease the resulting unsteadinesses emerging from flow separation, especially in SBLI cases, which are considered in this thesis. As a result of this overview on non-circular injectors and the desired effects in air jet flow control applications, four different shapes have been selected. In order to perform a first assessment on the influence of injector shape aspect ratio in AJVG systems, two elliptic injectors, with AR=0.5 and AR=2 respectively, have been implemented, also in light of the discrepancies emerged between subsonic and supersonic conditions [49, 52, 56, 66, 67]. A rectangular injector with AR=2 was included to compare the effect of sharp edges with the elliptic AR=2 case. Moreover, large AR rectangular present stronger vortical structures according to Rao [15] and other studies [57, 58]. Finally, an isosceles triangle with a vertex angle of 30° and AR=1.86 closes this geometry selection. This last configuration has been included for several reasons. First of all, the introduction of a sharp corner facing the incoming supersonic flow should be beneficial in terms of total pressure loss as reported for the diamond and wedge cases [68, 69, 70]. As diamond shaped injectors might present excessive penetration, the triangular one has been preferred to verify the sharp corner influence, choosing the same angle aperture as in Tomioka et al. [69]. Moreover, as discussed throughout this chapter, triangular injectors showed a lower penetration in subsonic conditions [54, 53, 74] and an high mixing capability for sonic injections in quiescent flows [72], although a behaviour similar to the wedge shaped injector might be expected for supersonic crossflow injections [68]. This configuration is designed to be tested also orientating the apex in the opposite direction of the main flow to observe the "bluntness" effects for the same triangular shape.

All the considered geometries are characterized by the same hydraulic diameter to ensure similar mass flow conditions. More details on the dimensioning of the injectors are discussed in chapter 4. To ensure comparable results with the circular reference case, the same 45° pitched/90° skewed injection conditions will be maintained, thus some of the expected influences of the non-circular geometries might be either mitigated or altered by this particular angle configuration.

Chapter 4

Experimental Setup

4.1 AJVG Model

The tested baseline AJVG model and the designed different non-circular variants in this thesis will be described in this section. A more detailed description of the design process for the clean and circular configurations of the AJVG system can be found in Hinke [31], as part of the same research project. More detail will be here given on the non-circular inlets manufacture and the consequent adjustments that were needed on the baseline configuration.

4.1.1 Overall Wind Tunnel Model

The overall wind tunnel model is showed in figure 4.1, where all the basic dimensions are expressed in millimeters. It consist of a base plate, a modifiable top plate and a 24° compression ramp for shock generation. The base plate was manufactured out of high-grade steel and serves the main assembly process of the other parts. Its leading edge has a 10° chamfer to facilitate a homogeneous inflow. All the other components of the reference AJVG model were made of aluminium. The modifiable top plate is composed by three main parts and allows different modular configurations and opens to other possible test cases. The front part is a flat plate with a chamfer as in the base plate. A fully turbulent boundary layer is ensured by a laminar fence installed in the front part of the plate, as visible in figure 4.1. The middle part consist in the core of the model, the AJVG module. Finally, a third rear part is a simple rectangular plate with a notch for instrumentation and on which the 24° compression ramp is mounted. This allows to test different ramp configuration or probe installations. As regard the 24° compression ramp, the two sided inclination ensure a more stable flow due to a minimal wake region. The angle value has been

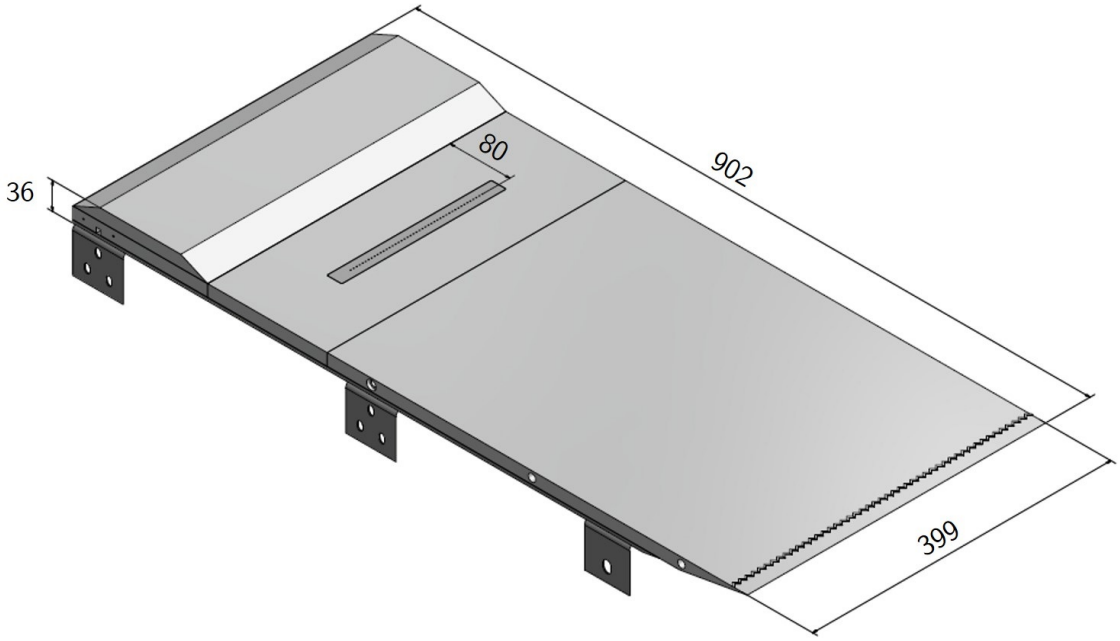

Figure 4.1: ISO-CAD view on the overall wind tunnel model [31].

selected to induce a significant SBLI separation. All the parts of the reference model were produced by the workshop of the Institute of Aerodynamics of RWTH Aachen.

4.1.2 AJVG Reference Model

As described in section 2.3, several factor affects the effectiveness of an AJVG system. A summary of the main configuration parameters used in this experimental setup are here listed. First, the selected development length between the jet array and the interaction area was chosen, in accordance with Szwaba results [37], of roughly 10 times the boundary layer thickness δ_0. Since a $\delta_0 = 8mm$ was first assumed in the design process, a total development length of $L = 80mm$ has been selected. However, later schlieren visualization resulted in a boundary layer thickness of $\delta_0 \approx 10mm$.

Szwaba's configuration has been used as reference as well for both orifice diameter and inclination angles. As regard the diameter, Szwaba suggests a $d_{jet} = 0,1 - 0,2 \times \delta_0$, therefore a 1,0 mm diameter has been selected. Lower values could not be achieved in the reference case due to manufacturing limitations. A skew angle of $\theta = 90°$ in respect to the incoming flow and a pitch angle of $\phi = 45°$ with the plate surface were selected, in accordance with several studies of AJVG applications for SBLI separation control [18, 13, 32, 34]. The AJVG system is arranged in an array of 23 equidistant orifices, with a spacing of 8 mm. Among the different spacings

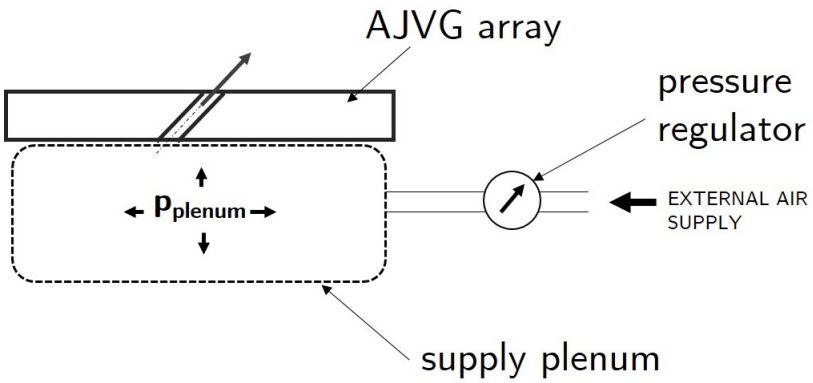

Figure 4.2: Schematic of the externally supplied AJVG plenum

tested within the project group this resulted to be the most effective, therefore it has been used as reference for the non-circular injector arrays.

Pressurized air is provided by an external supply and stagnation pressure inside the supply plenum is measured, in order to obtain the desired value (figure 4.2). As commonly done in other studies, a $p_{0,plenum}$ more or less equal to the main flow stagnation pressure is used [18, 32], in order to recreate similar conditions of self-supplying AJVG systems. Therefore a $p_{0,plenum}$ of circa 1 *bar* is applied. A Mach 2.5 main flow results in a static pressure p_∞ of $0,058 \pm 3\%$ *bar*. Since the obtained pressure ratio at the jet entry is far below the critical value of 0,528, an underexpanded injection is obtained. Further details on the experimental flow conditions is provided in the next section of this chapter.

An ISO-CAD view of both model and reference inlets of the AJVG module is showed in figure 4.3. A pressured air plenum (1) with a notch (2) for the interchangeable inlets is present. The inlets are inserted into the module and fixed with bolts. The insertion from below generates a self-sealing connection due to excess pressure and a sufficiently flat surface is obtained, with only small disturbances introduced and visible as Mach lines in the schlieren images. An uniform pressure supply is provided by three holes drilled into one wall of the plenum (3) and connected to the external air supply through the front part of the top plate and an external connection. All bonds between subdivided parts are rubber sealed by O-rings. Plenum conditions are then monitored through probes inserted into the two holes in the wall opposite of the supply holes (4). A static pressure probe and a thermal element have been used (figure 4.4). Their wiring is placed in a notch in the rear part of the top plate leading to the tunnel wall.

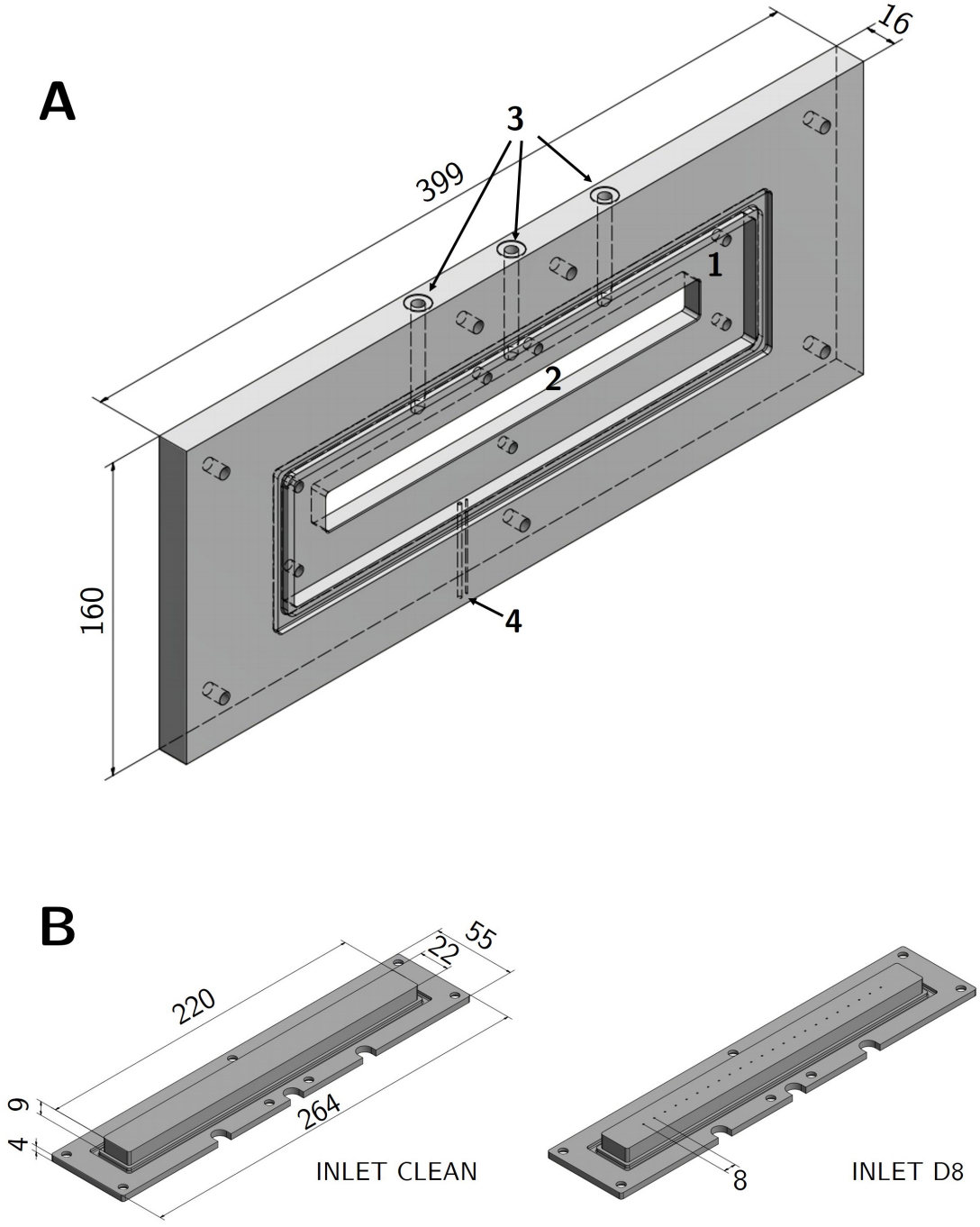

Figure 4.3: ISO-CAD view of the AJVG module (A) and both the clean and 8 mm reference inlet (B)

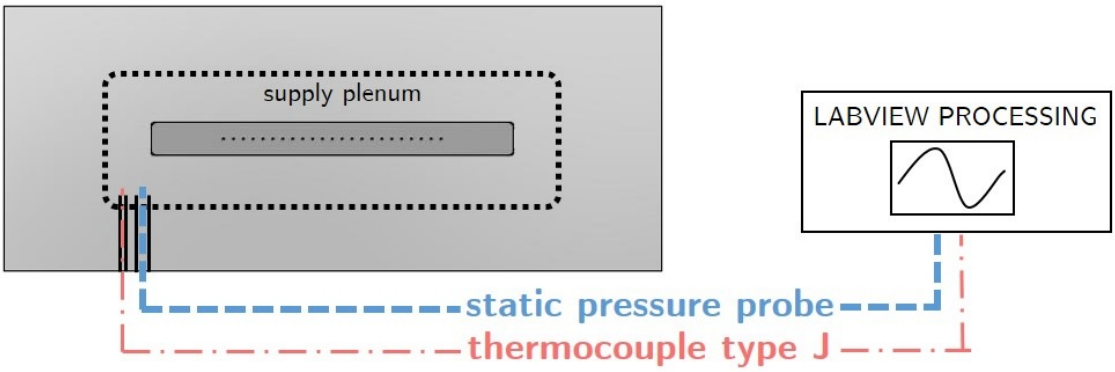

Figure 4.4: Schematic illustration of the internal measurement system of pressure and temperature

4.2 Non-circular AJVG inlets

Four different non-circular AJVG arrays have been designed for future assessments on geometry influence in this thesis: an high AR (aspect ratio) ellipse, a low AR ellipse, an high AR rectangle and an isosceles triangle with a top vertex of 30°. Motivation on this selection has been provided at the end of previous chapter. This section will focus on the orifice sizing, the selected manufacturing process and other aspects of the designing process.

4.2.1 Injector sizing

While circular injectors can be analyzed with a 1D model due to the axial symmetry, non-circular ones present 2D cross-sectional effects that affect the flow field inside the conduit. In order to have a more accurate comparison of the shape influence in AJVG applications, the same mass flux should be preserved among the different non-circular test injectors. This would require some mass flux measurements inside the injectors but this was difficult to achieve due to the small size of the injectors ($\approx 1mm^2$) and their limited accessibility. Thus an equivalent dimension that gives a result as close as possible had to be used. For non-circular pipe/duct sections there are usually two different sizes that are considered: hydraulic diameter and equivalent diameter. The hydraulic diameter (D_h) is defined as the ratio of 4 times the cross section and the perimeter of the "wetted area", that for a full wetted perimeter is:

$$D_h = \frac{4A}{P}$$

D_h can be seen as the diameter that gives a ratio of pressure forces, acting on

the flow cross section, to friction forces, applied along the channel perimeter of arbitrary shape, similar to the ratio of the same forces in an equivalent circular section with diameter $D = D_h$. The concept of the hydraulic diameter allows the use of relationships developed for circular pipes with non-circular conduits. The hydraulic diameter is usually employed in defining Reynolds number, friction factor and other characteristic values. It works well for turbulent flow where geometry is less important, but should not be used for the laminar flow regime, which is influenced to a much higher degree by conduit geometry [76, 77]. The equivalent diameter (D_e) is defined as the diameter of a circular pipe that gives the same pressure drop per unit length as the one with the non-circular section considered. For a circular section it is obvious that $D = D_e = D_h$. Depending on the shape, several equations for its computation have been developed, for example for a rectangular section Huebscher [78] provided a relation:

$$D_e = 1.30\frac{(ab)^{0.625}}{(a+b)^{0.25}}$$

Analogously for the elliptical case a relation was found by Heyt and Diaz [79]:

$$D_e = 1.55\frac{A^{0.625}}{P^{0.25}}$$

These relations have been proved to be inaccurate with a further analysis of the previous papers data performed by Koch [80]. Both relations take the hydraulic diameter as a starting point for the computation of an equivalent diameter that would provide the same pressure drop of a circular pipe but Koch showed that actually the correct value is closer to the hydraulic diameter than predicted by Huebscher and Diaz relations. For a square duct where AR=1, $D_e = 1.035D_h$ while for a rectangular duct with AR=8 $D_e = 0.955D_h$. Thus the usage of hydraulic diameter is usually preferred over equivalent diameter.

The characterization of the geometry of the non-circular injectors has been performed with the same hydraulic diameter of the reference circular case (1 mm) in order to maintain similar overall properties of the flow (pressure loss, Reynold number, mass flow). Even if the mass flow might not exactly be the same with this consideration, it should give a good approximation for the comparison.

Elliptic injectors

The two elliptic injectors considered have an aspect ratio of 2 and 0.5 respectively. They actually consist in the same shape but with a 90° rotation difference, therefore

the sizing is identical for both cases. For an AR=2 elliptic section, with the two semi-axes defined as a and $b = 2a$ the perimeter can be computed with the Ramanujan first approximation (1914) and it follows:

$$p \approx \pi \left[3(a+b) - \sqrt{(3a+b)(a+3b)}\right] = \pi a(9 - \sqrt{35}) \quad \text{and} \quad A = ab\pi = 2\pi a^2$$

For a $D_h = 1mm$, substituting the two obtained expression in the hydraulic diameter definition it follows $a = 0.3855mm$ and $b = 0.7710mm$. With these dimensions the respective cross section is $A_{ellipse} = 0.9337mm^2$, with an increase of 18.9 % in comparison to the reference circular case ($A_{circular} = 0.7854mm^2$).

Rectangular injector

The rectangular injector considered has an aspect ratio of 2. For this value, with the two sides defined as a and $b = 2a$, the following results hold:

$$P = 2(a+b) = 6a \qquad \text{and} \qquad A = ab = 2a^2$$

For $D_h = 1mm$ then $a = 0.75mm$ and $b = 1.50mm$. The respective cross section is $A_{rectangular} = 1.125mm^2$, thus an increase of 43 % of the cross section in respect to the reference circular is obtained.

Triangular injectors

For the triangular case, an isosceles triangle with a top vertex angle of 30° has been used. For a given base a, the height and the side length are defined as $h = a/2\tan(75°)$ and $l = a/(2\cos(75°))$. It follows:

$$P = a(1 + 1/\cos(75°)) \qquad \text{and} \qquad A = (a^2\tan(75°))/4$$

For $D_h = 1mm$ then $a = 1.3032mm$, $h = 2.4318mm$ and $l = 2.5178mm$. The relative cross section is $A_{triangular} = 1.5845mm^2$, with an increase of 101.7 % of the cross section in respect to the reference circular one.

From these simple calculations it is possible to see that non-circular cross sections with the same hydraulic diameter present a larger area than the circular one, especially the cases with sharp angles. For these geometries the flow near corners is more affected by the viscous effects of the wall, thus the average velocity for the same cross section is lower. A larger cross section compensate this effect and ensure

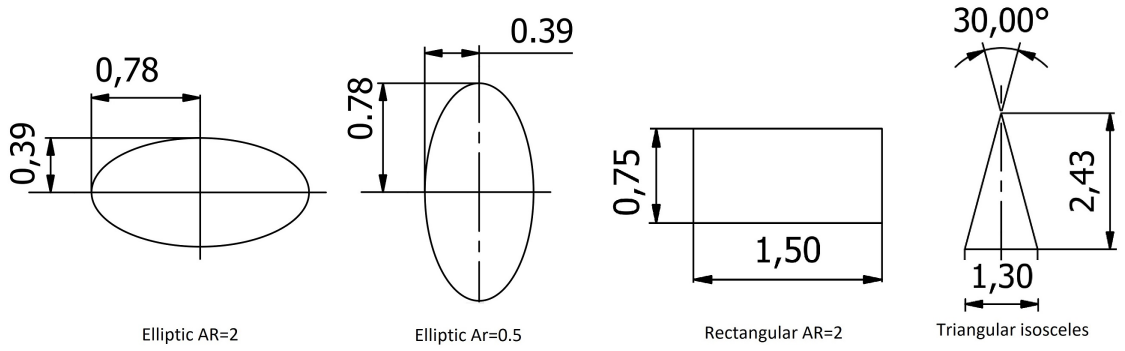

Figure 4.5: Overview of the four selected shapes. Values in millimeters

a similar mass flow. An overview of the selected shapes is given in figure 4.5, where the values, expressed in millimiters, have been rounded to the second decimal digit (in the order of $10\mu m$). The reported value are just theoretical as the real injectors tolerances are definitely higher due to the manufacturing process. It is worth noticing that, due to the 45° injector inclination in respect to the plane, their surface exit present an elongation in the spanwise direction by a factor of $1/\cos(45°) = \sqrt{2}$.

4.2.2 Manufacturing techniques for non-circular inlets

A crucial part in the development of non-circular AJVG inlets was to find an adequate and cost-effective manufacturing process to produce the shaped orifices. Although the full AJVG model was produced entirely in the Aerodynamic Institute workshop of the RWTH, the smallest attainable orifices were 1 mm circular holes with basic drilling techniques, therefore no shaped and consequently more precise injectors could be produced. Additive manufacturing techniques have been discharged for mainly two reasons: first, for both cost and production continuity, manufacturing of the full inlet outside the workshop was avoided and second, a drilling process was more suitable to the geometric nature of the part rather than an additive one. The required level of precision for the small shaped ducts and the amount of material required per part made this type of process unfeasible.

Hence the clean inlets to be drilled were manufactured at the institute workshop and a suitable drilling technique needed to be applied, since conventional mechanical drilling could not attain the required precision for the shaped injectors. Among the various techniques, two possible alternatives have been identified: electrical discharge machining (EDM) and pulsed laser drilling. Both drilling techniques are very common in the aerospace field, especially for cooling applications in turbine blades.

Electrical discharge machining

Electrical discharge machining (EDM), also known as wire or spark erosion, is a manufacturing process in which a desired shape is obtained by means of rapidly recurring electrical discharges which remove material from the work piece. This technique can be used for different operation such as cutting and drilling. The current discharges are generated between two electrodes, the tool-electrode and the work piece, which are separated by a dielectric liquid and subjected to an electric voltage. Depending on the operation the work piece can be also sunken in the dielectric liquid. It is crucial that the two electrodes are close enough to generate the material removing spark but do not make actual contact otherwise short circuit can occur. As regards EDM drilling process, there usually is a thin and long electrode, generally made of brass or copper, operated by a servo mechanism which provides the proper gap for spark erosion and that presents one or more cavities from where the dielectric fluid is constantly injected. This fluid, usually deionized water, other than allowing the generation of the spark, helps flushing the generated debris and works as coolant. In addition, the electrode usually rotates in order to generate a better quality drilling and to reduce sides erosion. With this technique very long aspect ratio holes can be obtained ($L/D > 100$), however deeper holes results in a more severe wearing of the electrode which levitates substantially the cost of the process.

This technique can provide small precise and deep holes, however for manufacturing shaped holes it could be excessively costly. After consulting the Werkzeugmaschinenlabor of RWTH (WZL, Laboratory for Machine Tools), it emerged that for this type of holes the electrodes would have been custom-made, factor that increases substantially the cost and since there are no internal holes for rinsing, in combination with the high length-to-diameter aspect ratio, the process would have been too much slow and characterize by an excessive wearing of the electrodes. A first estimation of the cost was in the order of 800€ per single hole, depending on the material to be processed. Lower costs could have been obtained with a reduction of the inlet thickness, however the custom-made electrodes are the most expensive part of the process. A possible way to overcome the need of custom-made electrodes has been successfully performed Yu et al. [81]. By means of a planetary movement of a smaller electrode, extra space for debris removal is provided and consequently the material removal rate increases with a reduction of the electrode wearing. They successfully obtained both high aspect ratio holes and blind non-circular micro holes in the order of $100\mu m$ (figure 4.6). Unfortunately no manufacturer which could perform this last operation was found.

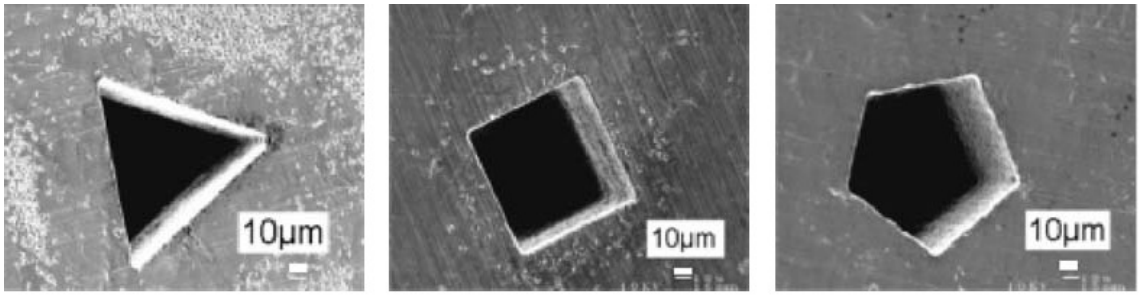

Figure 4.6: Blind non-circular micro holes from EDM drilling with planetary movement [81].

Pulsed laser drilling

Laser drilling is one of the non contact type machining process that are employed in machining of stiff and high-strength materials and high strength temperature resistance materials. It is a good alternative to expensive process as wire electro-discharge or other techniques. Laser drilling generally occurs with ablation of the work piece material through absorption of energy from a highly energized focused and pulsed laser beam. The molten metal is usually blown away using an assist gas. Since the laser beam has a Gaussian energy distribution, the interaction area between the laser and the work piece can be divided into a larger irradiated area, a more intern melting area and a central ablation area where the energy peak is located [82]. Commonly used for this process are Nd:YAG lasers. Large aspect ratio holes can be performed with this techniques, with diameter sizes down to the range of $10\mu m$ [83]. The pulsed controlled beam allows a narrow region of high energy but the severe thermal loads emerging from the process might damage the surrounding material with the generation of plasticity regions. These dangerous effects can be mitigated with the implementation of ultra short laser pulses with a pulse duration of typically less than 10 ps [84]. This feature allows an higher precision and control of the thermal loads, and more precise holes in the range of the micrometer can be obtained, with much reduced regions of additional stress.

Several laser manufacturing companies, mostly in the North Rhine-Westphalia region, have been contacted to have an overview on the feasibility of the laser drilling process for the non-circular AJVG inlets. In general, even if high aspect ratio micro holes are attainable with laser drilling, there is an upper limit on the maximum thickness of the material to be drilled since after a certain depth the produced hole might result excessively distorted. Considering also the complication due to the 45° inclined drilling process, a maximum inlet thickness of 3-4 mm was suggested by all the contacted manufacturers. Additionally, material with low melting point as aluminium ($\approx 660°C$) are not suitable for this process and other metals such as stainless steel or titanium alloys are usually employed. The attainable precision via

laser cutting from the contacted manufacturers was in the order of 20 to 50 μm, however this value can be higher as a consequence of the inclined drilling process. Some manufacturers pointed that through laser cutting the exit diameter is usually smaller ($\approx 50\mu m$ less) and never have straight edges. Early quotes were in the range of 300€ for a test part and a similar price for each inlet, therefore with a substantially lower price than EDM drilling process, even if the latter could have provided more precise exit diameters. For this reason pulsed laser drilling was preferred over EDM techniques and the manufacturing process was committed to the Fraunhofer-Institut für Lasertechnik (ILT) based in Aachen.

4.2.3 Reduced thickness model - influence of length to diameter aspect ratio

Since pulsed laser drilling has been chosen to manufacture the non-circular injectors, the clean inlets to be drilled were produced with high-grade stainless steel, differently to the rest of the AJVG model which is aluminium-made. Due to drilling limitations the original thickness of the inlet had to be reduced from 13 mm to only 3 mm. In order to do so, an additional 10 mm deep notch on the original inlet model has been added. Hence the resulting channel length of the injectors reduced to only $\approx 4.3mm$ and with a channel length to diameter ratio L/D of only 4.3, compared to the original ratio of $L/D \approx 18.4$. As already mentioned, Peterson and Plesniak [45] showed that for significantly low L/D values the channel flow is not fully developed and different recirculation regimes in the plenum supply chamber affects significantly the penetration properties of the jets. This mentioned study refers to both low speed crossflow and injections and to a much lower lenght to diameter ratio ($L/D = 0.5$) compared to the one considered in this AJVG configuration, hence the sonic injection and the sufficiently longer channel should make this effect negligible. Nevertheless, a reference inlet with circular holes and reduced thickness has been included in the measurement to verify the absence of any side effects caused by the additional notch. A CAD view of the reduced thickness reference inlet can be seen in figure 4.7. Finally, in order to test the same inlet in two different orientations, the three small half-circular notches in correspondence of the air supply holes have been performed on both sides, making the inlet symmetric and allowing two different mounting possibilities. This has been performed especially for the triangular case so that both configuration with either vertex or basis facing the incoming flow could be tested with the same inlet. ISO-CAD details of the four non-circular inlets are given in figure 4.8.

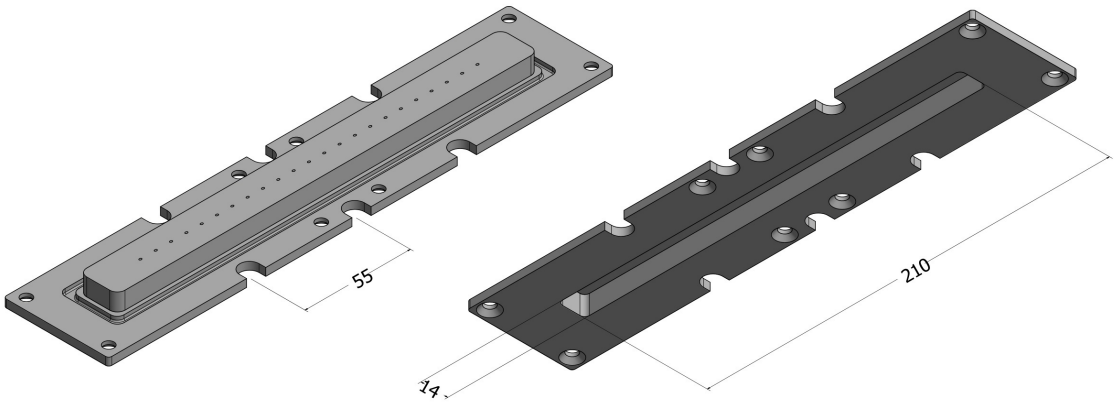

Figure 4.7: ISO-CAD view of the reduced thickness reference circular AJVG inlet

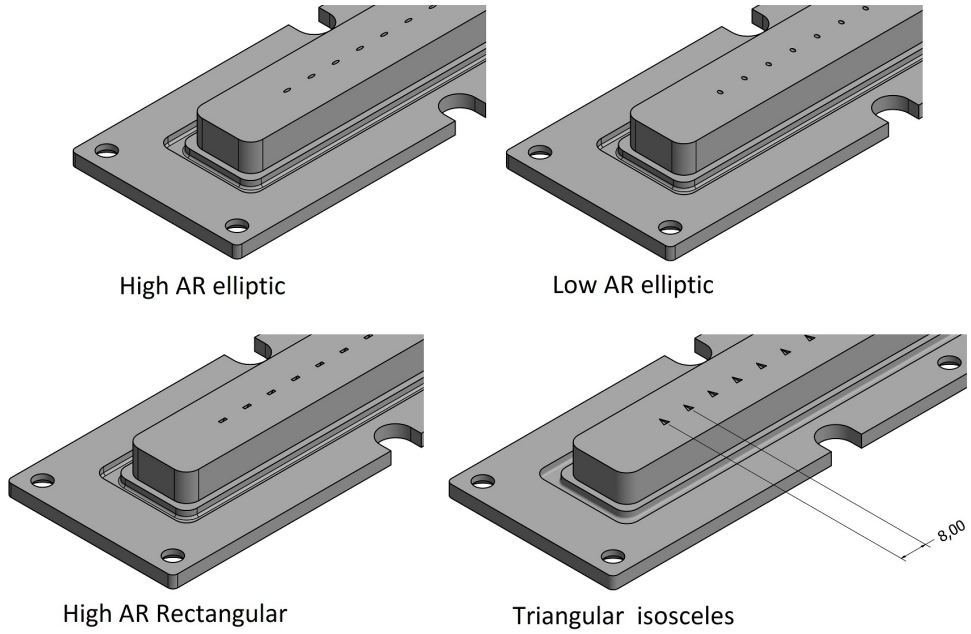

Figure 4.8: ISO-CAD details of the non-circular AJVG inlet

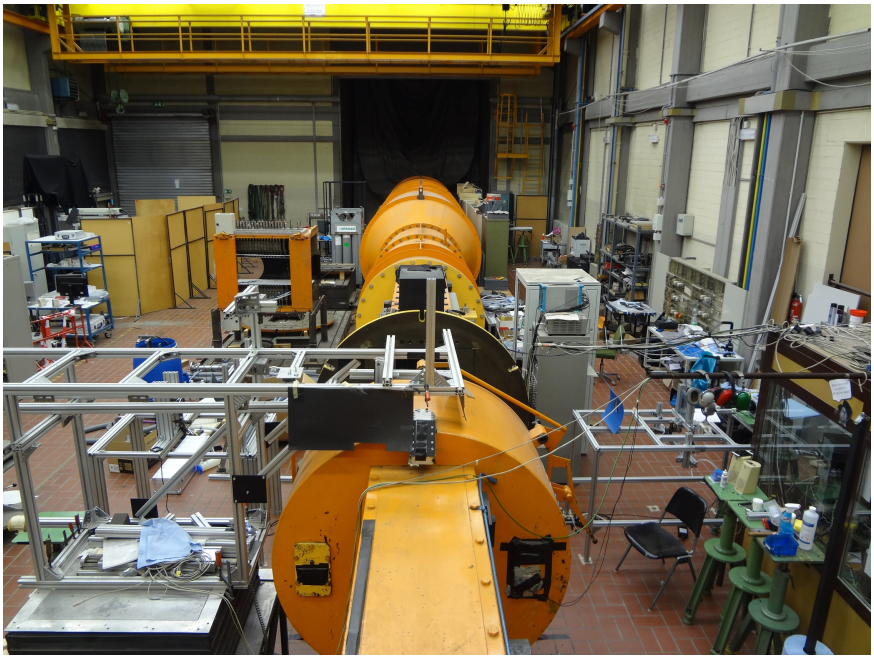

Figure 4.9: Top view of the trisonic wind tunnel of the Institute of Aerodynamics of the RWTH Aachen

4.3 Wind tunnel specifications

The experimental studies of this thesis and of the whole project were performed in the trisonic wind tunnel at the Institute of Aerodynamics of the RWTH Aachen (figure 4.9). In this blow-down tunnel supersonic conditions are obtained with a variable Laval nozzle. The cross-section dimensions of the measurement section are 400 mm x 400 mm. Two circular windows with a 280 mm diameter at the left and right walls of the measurement test section provide optical access. A third extra window at the top side of the channel is also present. Tests were performed at a Mach 2,5 speed, with an average time of stationary measurement of approximately 3,5 seconds. By means of vacuum tanks with a total capacity of $4{\times}95\ m^3$, the blow-down facility is operated with dried air stored in an air balloon reservoir with a volume of 165 m^3 which holds the current ambient temperature and pressure. Therefore, total conditions of the fluid are the same of the ambient ones in the hall. The air balloon is continuously refilled by an external compressor that draws air from the vacuum tanks. A schematic of the whole tunnel is given in figure 4.10. An average set of fluid conditions were obtained from the data transcript of the test series. The main values are listed in table 4.1. The boundary layer thickness $\delta_0 = 10mm$ was obtained from the Schlieren pictures showed in the next chapter. This value will be used as measure unit for the results presented next.

Flow Parameter	**Value**	**Annotation**
Mach number, Ma	2,5 + 1%	nozzle setup
Reynolds Number Re	$9,6 \times 10^6 1/m \pm 1\%$	f(ambient)
Stagnation Pressure p_0	1 bar $\pm 0,5\%$	f(ambient)
Stagnation Temperature T_0	295 K $\pm$ 5 K	f(ambient)
Humidity ϕ	1-5 %	f(ambient)
BL Thickness δ_0	$\approx$ 10 mm	Schlieren img.

Table 4.1: Flow experimental parameters

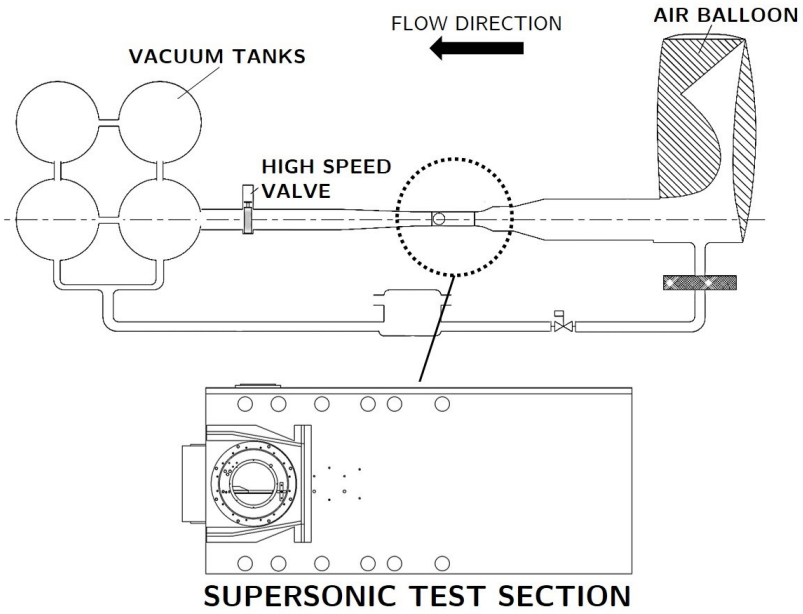

Figure 4.10: Schematic overview of the trisonic wind tunnel with detail of the supersonic test section

The most critical parts to be analyzed in the model are the ramp and the AJVG array, comprising of a region upstream of the jets. Both boundary layer separation and reattachment are expected to occur in these regions. Moreover, the interaction of the main flow with the jets is crucial in the momentum exchange process. For this reason, the longitudinal position of the model within the test section is defined by the field of view of the windows on these specific regions (figure 4.11).

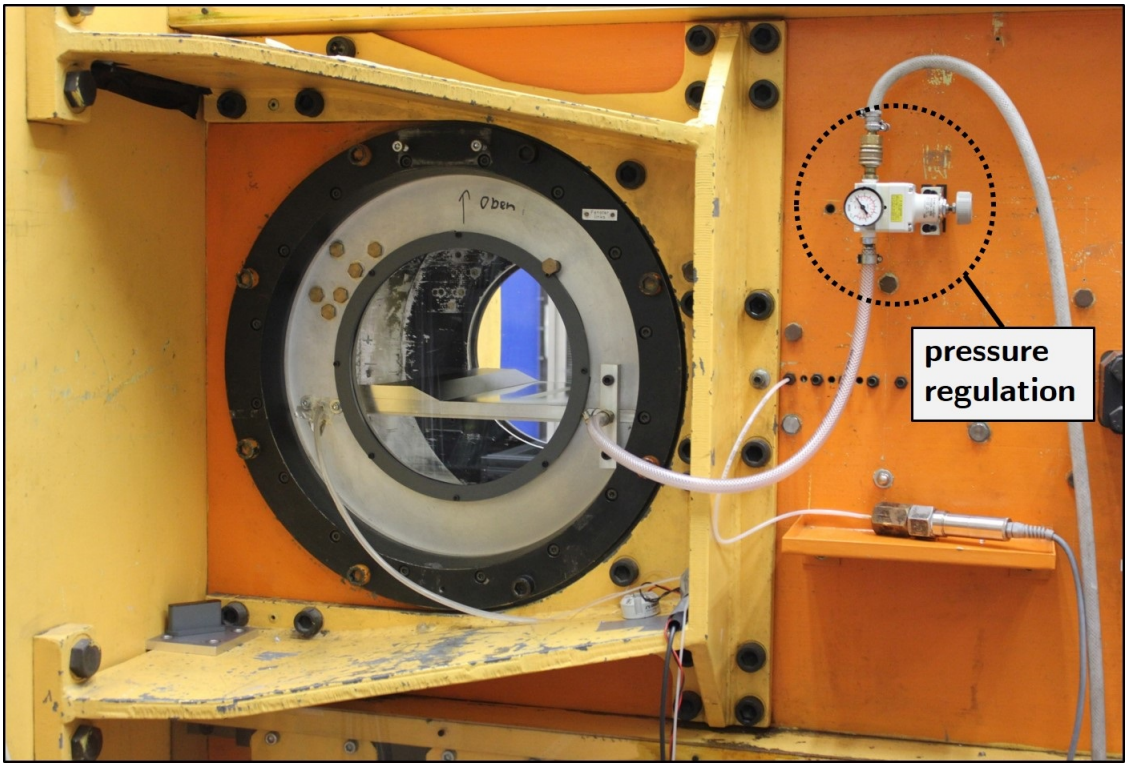

Figure 4.11: Side view of the mounted model and of the external air supply system

4.4 Measurement techniques and systems

While most of the AJVG parameters are defined by design and cannot be varied, the only adjustable value is the $p_{0,plenum}$ which is manually adapted throughout the tests according to the inlet variation and the mainstream conditions. Air supply pressure is controlled by an external regulation valve as can be seen in figure 4.11 where a side view of the mounted AJVG model is provided. In order to maintain the same plenum conditions for all the tests a static pressure probe and a Type J thermocouple are installed in the pressure plenum (figure 4.4). The obtained value can then be further used for an estimation of the jet outblow conditions.

4.4.1 Oil flow visualization

A common method to obtain detailed and at the same time wide characteristics of the flow motion, especially for separation and vortex trails regions, is oil flow visualization. A mixture of an oil-based fluid mixed with suitable colour pigments is applied to the surface of the model. During the test run the tunnel flow is imprinted on the oil layer and the flow structures are visualized by the colour pigments' dye.

This is then recorded by a camera. Oil flow visualization are helpful for qualitative and also quantitative information of separation area and reduction, flow directions and vortices trails. In order to obtain clear flow traces a suitable oil mixture, of which the optimal composition depends on the main flow conditions, is necessary. For this thesis the same mixture applied in other tests within the AJVG project group was used. The applied blend consists of an hydraulic oil (Shell Tellus S22 $\approx 64\%$ in weight) mixed with titanium dioxide ($TiO_2 \approx 30\%$) as white dye. For a fine-tuning of the mixture, oleic acid ($\approx 6\%$) was used to adjust the viscosity of the fluid. In order to obtain an higher contrast in the flow visualization recordings and photographs, the analyzed top parts of the model were spray painted pitch black in contrast to the white titanium dioxide. Video recordings were made with a digital compact camera Sony DSC RX100 mounted at the upper channel window.

4.4.2 Conventional and focusing schlieren

Compressible flow phenomena are typically observed through schlieren photography, which is a non-intrusive visualization technique. Its basic working principle relies on the refracting index of air that depends on the local fluid density. Strong compressibility effects such as shock waves generate large density gradients which in schlieren photography are visualized as darker streaks due to the different deflection of light. A basic schlieren optic setup consist of a light source, lenses, a cut-off device and finally a camera which captures the image. Classic setups allow full span two-dimensional images of the measuring section, in which the visualization is an "average" of the spanwise flowfield. Conventional schlieren photographies were taken for the uncontrolled case and the reference 8 mm spaced AJVG array with full length injectors, in order to have high resolution images of the overall flow topology. A Canon EOS 550D camera with a shutter speed of 1/4000 was used for this purpose. However, since the AJVG array does not cover the full spanwise length but only the central part, conventional visualizations show an overlap of both the uncontrolled region at the sides, which is also affected by wall effects, and the controlled region in the middle. For this reason an advanced large-field focusing schlieren system was designed and implemented within the AJVG project group by Schauerte [85, 86] of which a schematic can be seen in figure 4.12.

Conventional schlieren systems are characterized by the focusing of a single point source of light into a cut-off device (usually a knife-edge) on the focal point to control the light intensity which generates images integrated along the optical axis. In the used focusing schlieren system instead, a back-lit source grid is projected onto a corresponding plane where the cut-off grid is positioned. This second grid consist of a negative image of the source grid taken without flow in the test chamber which can be adjusted vertically for different cut-off settings. This arrangement can be seen as a series of light source slits and their corresponding cut-off stripes

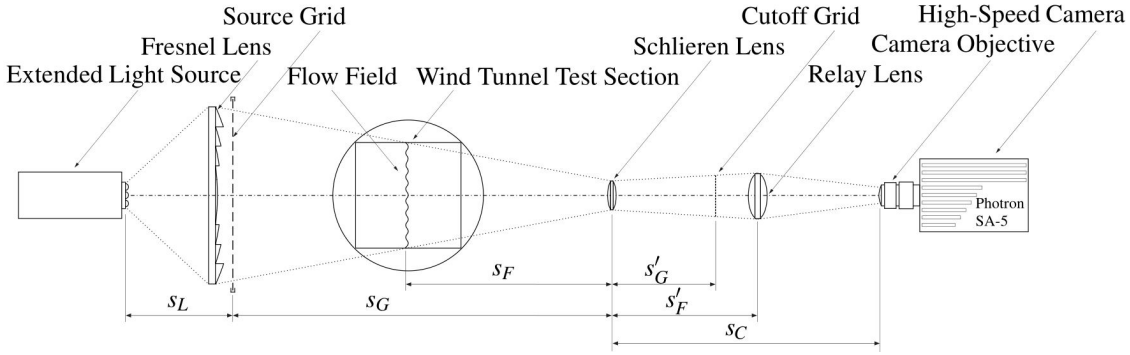

Figure 4.12: Schematic of the focusing schlieren arrangement with optical relay system ($s_L = 623$ mm, $s_G = 3189$ mm, $s_G{}' = 591$ mm, $s_F = 1510$ mm, $s_F{}' = 787$ mm, and $s_C = 1032$ mm). From Schauerte [85].

working as independent schlieren systems, where each light cone presents a different inclination in respect to the optical axis. As in conventional schlieren, light path from each cone is then deviated by density gradients and eventually blocked by its individual "knife-edge" stripe, generating the characteristics streaks of schlieren imaging systems. Therefore the obtained image is composed of a superposition of multiple source images obtained with different light cones which for a fixed axial position of the camera provide a sharp image of a specific plane of the measuring section. Objects placed outside of the focal plane, instead, appear blurred due to the limited depth of field of this system. On the top side of figure 4.13 there are showed the adjustable high-power white LED array used as light source, the Fresnel lens and the large-scale light source grids composed of alternating black and clear stripes. On the bottom side of the same figure there are the main focusing lens, the cut-off grid generated by exposing photosensitive sheet films and a second lens which projects the image on the recording camera. The two racks were mounted on the sides of the wind tunnel test section. In order to capture the characteristic low frequency oscillation of shock-boundary layer interaction and the large scale turbulent structures a Photron Fastcam SA5 high speed CMOS camera was used. A spatial resolution of 704 $\times$ 520 pixels with a 20kHz framerate and a reference shutter speed of 1/240000 were selected. Other shutter speed were also used to obtain different contrast. The light source current can be adjusted from a minimum of 4 A to a maximum of 10 A. A far more detailed description of both design and working principle of the focusing schlieren system can be found in Schauerte's work [85, 86].

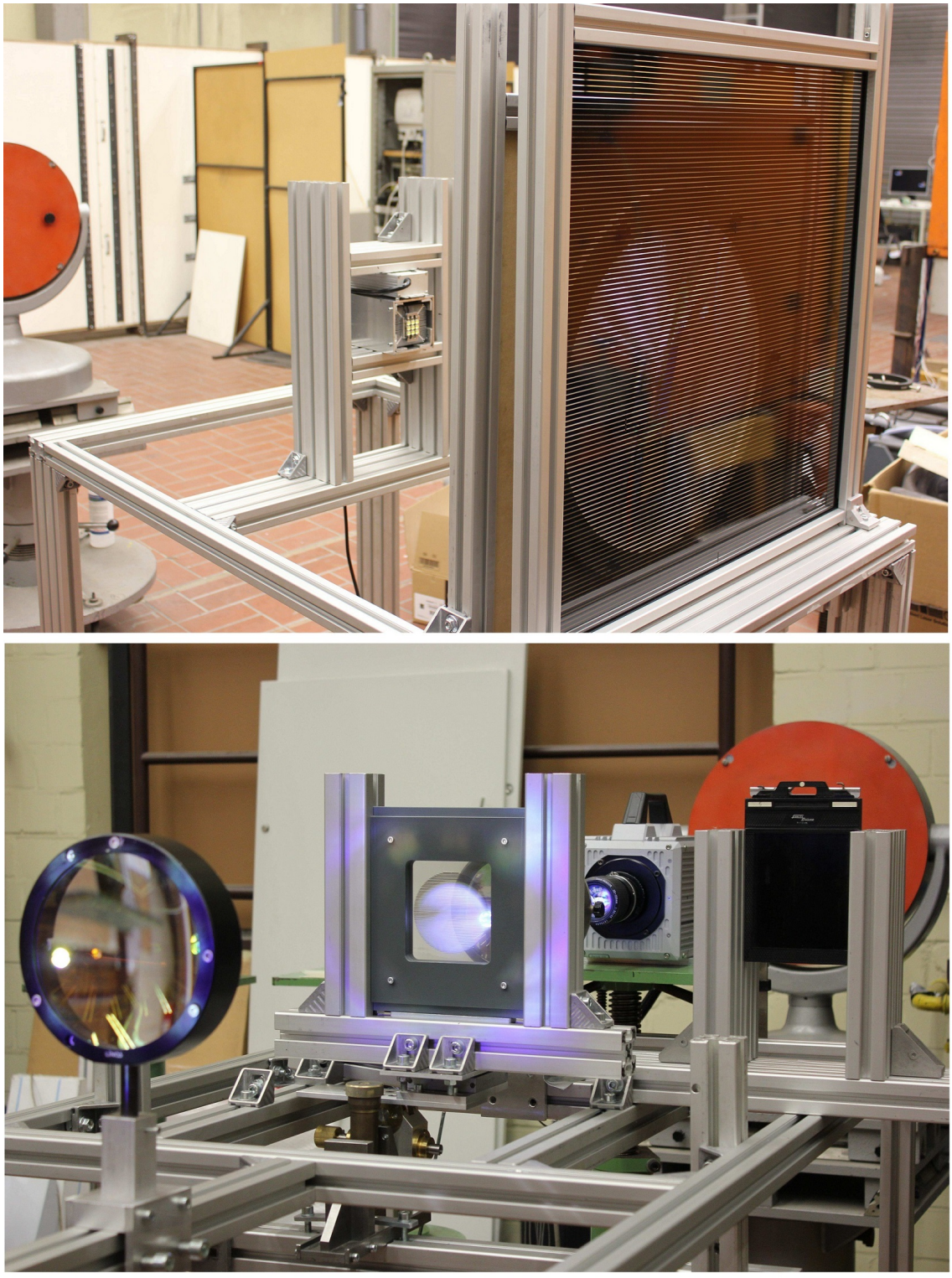

Figure 4.13: Focusing schlieren setup from Schauerte [85] used in the tests. Top: LED array light source, Fresnel lens and source grid. Bottom: main focusing lens, cut-off grid, projecting lens and high-speed camera.

Chapter 5

Results

In this chapter the results from the experimental tests will be reported. First, an analysis of the uncontrolled shock-induced separation flow topology is given. A detailed description of the reference AJVG system with circular orifices and its beneficial effect on the separation region is then discussed. Some insights into the flow field near the injection points are provided and additional assessments on the reduced inlet thickness and jet direction are also included and afterwards. The chapter closes with some considerations on the expected results from the non-circular AJVG inlets.

5.1 Shock Boundary Layer Interaction structure

To describe the effects of the AJVG flow control system a detailed overview of the wind tunnel test results for the baseline uncontrolled case, which will be referred as 'clean' configuration, are first here reported. Its flow topology can be observed in the schlieren images in figure 5.1, where also an additional schematic is reported.

The description of shock wave boundary layer interaction (SBLI) is performed mainly through the conventional schlieren pictures due to the higher definition but some considerations are made with the focusing schlieren images (figure 5.2). First of all, the incoming undisturbed turbulent boundary layer presents a constant thickness of roughly $\delta_0 = 10mm$. A fully turbulent condition is ensured by the laminar fence at the leading edge of the model as described in section 4.1. The visible three Mach waves, indicated in the picture with 'M', are generated by the small gaps between the modules of the top plate and the edges of the jet inlet. These lines are curved in the boundary layer region due to the normal velocity gradient. Outside the boundary layer they present an inclination of $\approx 24°$, which closely matches the

theoretical value for the free stream Mach 2.5 conditions (23.57°) and therefore a well-established tunnel flow is verified.

The separation shock of the overall SBLI structure is indicated with 'S'. It is located at about 3.8 $\times\delta_0$ ($\approx 38mm$) upstream of the compression ramp corner. Analogously to the Mach waves, the shock presents a varying curvature in the boundary layer region as it approaches the wall surface. From the conventional schlieren picture the shock does not appear as a thin line but as a thick dark region, since conventional schlieren photography provides an average of all the spanwise shock positions and in this case includes also those close to the windows which might have additional wall effects. The focusing schlieren pictures instead present a more defined separation shock, although some superimposition of different shock positions is observed as a consequence of the inherent unsteady oscillation of SBLI. Moreover, in the focused images the intensity difference between the strong separation shock and weak Mach lines is more evident. Moving back to the conventional schlieren image, the recirculation area is visible downstream of the separation shock. The separation bubble is associated with a thickening of the boundary layer as well as a strong reverse flow. These aspects are showed as darker traces in the detail A of figure 5.1. Downstream of the ramp corner the reattachment shock is visible as a widely spread darker area of recompression marked with 'R'. This might be due to a local merging of the weaker compression waves into the shock, as well as the oscillation of the reattachment shock itself. Even in the focusing schlieren pictures the reattachment shock is less defined and it does not penetrate significantly the boundary layer, therefore a precise identification of its position is difficult from the schlieren visualization alone. However, observing the detail view of figure 5.1, a reduction of boundary layer thickness and streamlines parallel to the ramp slope still indicates the reattachment process. Its position can therefore be initially estimated to roughly 1 $\times\delta_0$ downstream of the ramp corner. The merging of the separation and reattachment shocks is visible at around 4,2 $\times\delta_0$ elevation from the top of the ramp, and it is indicated in the conventional schlieren picture with 'T' (triple point). Additionally, some Mach waves disturbance generated at the leading edge of the model and reflected downwards from the upper wall of the wind tunnel encounter the formed shock system. This interaction presents no significant influence in the overall flow condition from the schlieren results. Figure 5.2 shows focusing schlieren images of the clean configuration with four different cut-off, light and shutter speed configurations, all focused in a middle spanwise position. It is worth noticing that for lower shutter speeds (picture D) finer turbulent structures, especially in the separation bubble, are visible. The generated SBLI structure is comparable to the expected lambda shaped shock system of a similar configuration by Settles [30], with a different separation shock position as consequence of other free stream conditions.

More detailed localization of the shock position have been performed by means of oil flow visualization as showed in figure 5.3. Both separation and reattachment

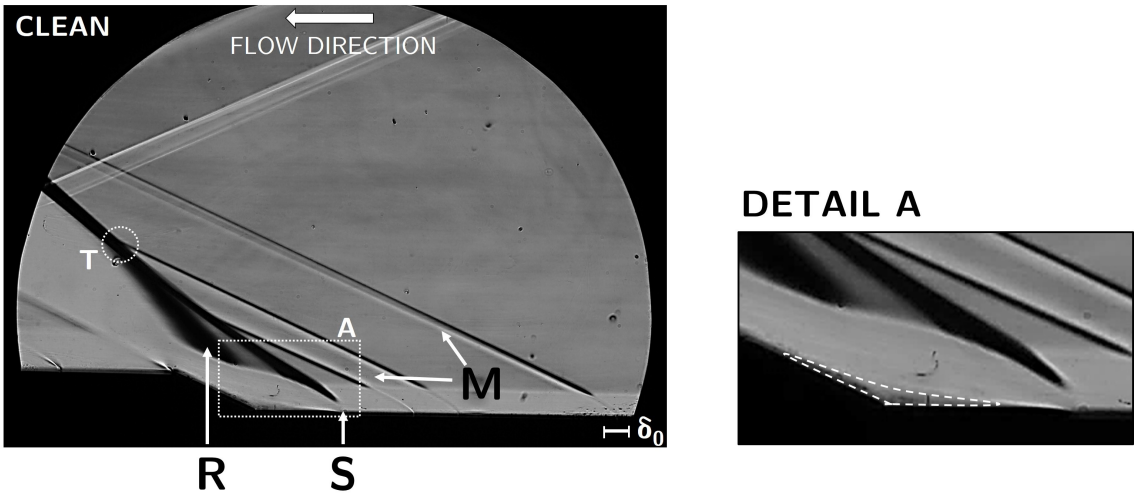

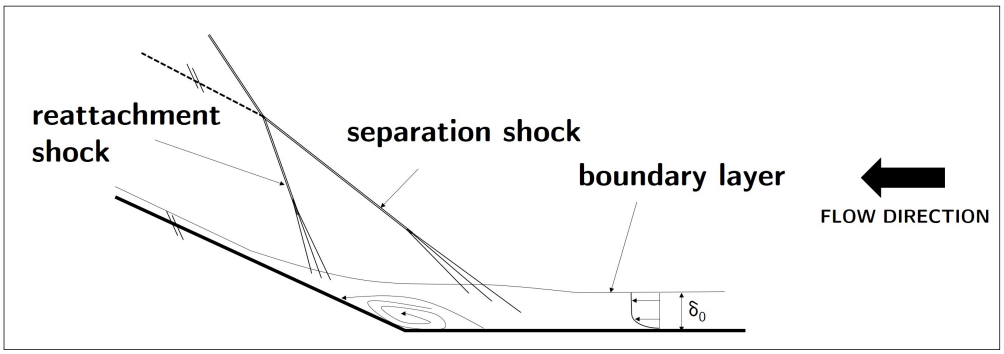

Figure 5.1: Top: Conventional schlieren visualization of the SBLI in the compression ramp model without AJVG control (Canon EOS 550D, shutter speed 1/4000). Bottom: schematic of the flow topology

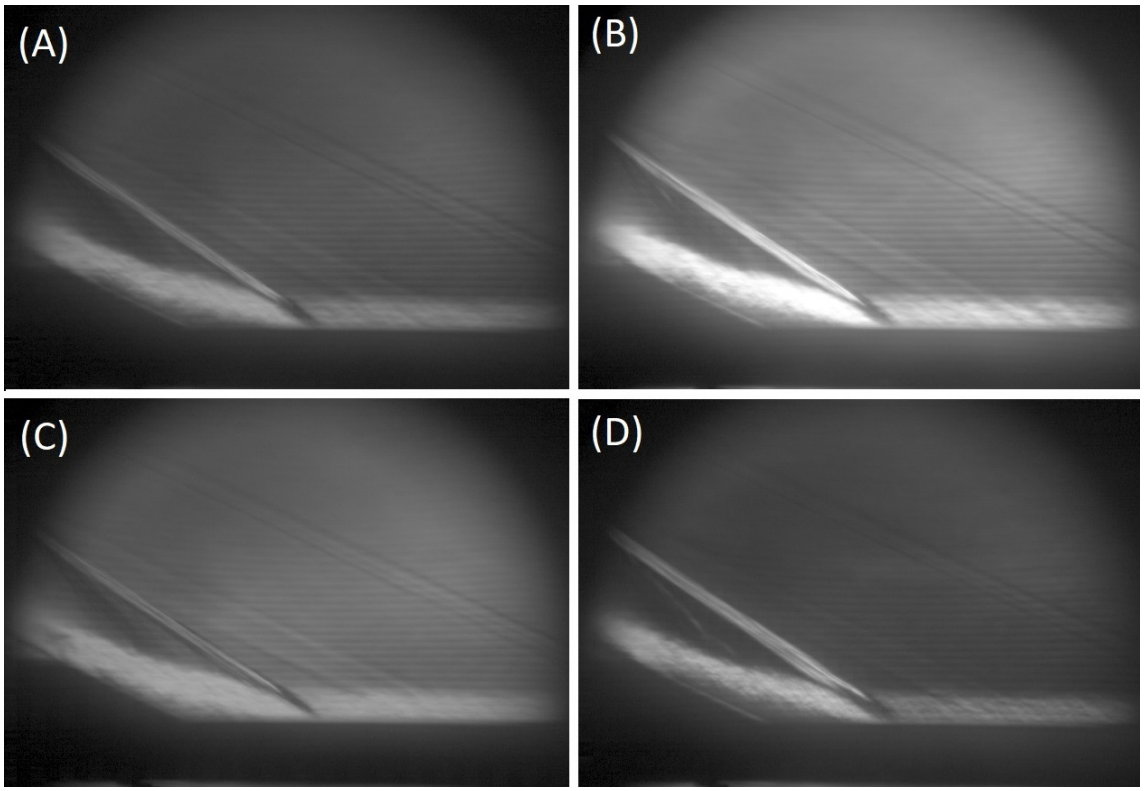

Figure 5.2: Focusing schlieren visualization of the SBLI in the compression ramp model without AJVG control with four different configurations: A) high cut-off, low light intensity (4 A), 1/240000 shutter speed. B) high cut-off, high light intensity (10 A), 1/240000 shutter speed. C) medium cut-off, low light intensity, 1/240000 shutter speed. D) high cut-off, high light intensity, 1/525000 shutter speed.

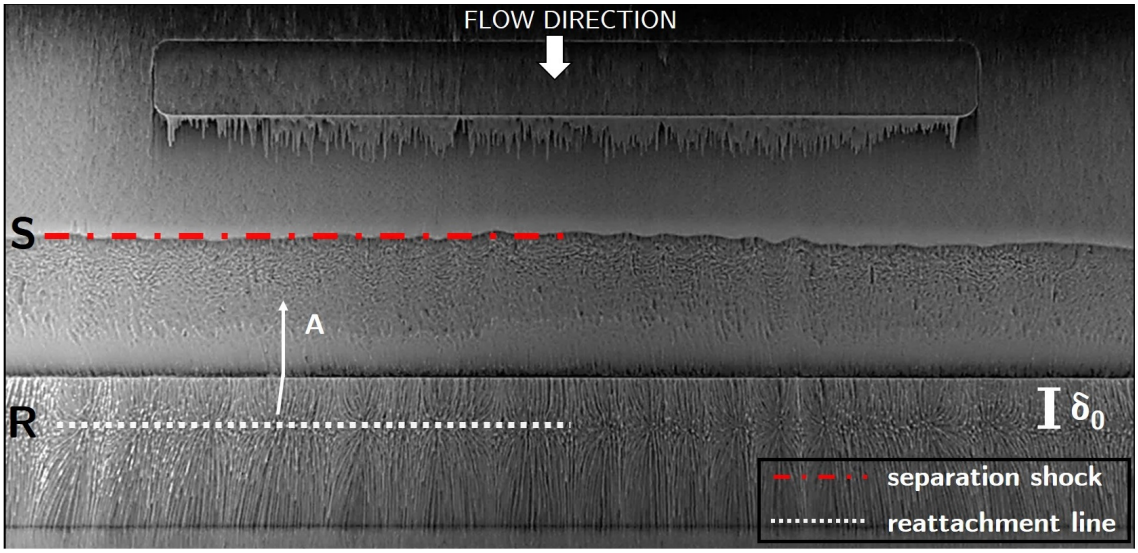

Figure 5.3: Oil flow visualization of the clean configuration

shock are indicated in the image. The first one is clearly visible and presents a small curvature on the sides due to wall effects. The previously estimated position is confirmed by the oil accumulation in the separation area. Reversed oil flow streaks (arrow A) confirm the presence of a recirculation region after the separation. The reattachment line instead is visible as a borderline between the reversed separated flow and the reattached flow in main stream direction. From the oil pictures it can be localized at about 1,6 $\times\delta_0$ downstream of the ramp corner. Overall flow topology matches Settles [30] and Verma et al. [32] results, however discrepancies from their visualization in the sides are present due to different installations of the models. Settles, for instance, installed some side fences to reduce the influence of the tunnel walls, with a comparable result to the full span installation of this test case. Verma et al. instead presented a model mounted in the middle of the channel with a gap between the model and the tunnel wall. Therefore altered three-dimensional characteristic of the flow topology might have affected the side regions.

5.2 Reference AJVG configuration with circular jets

After the discussion on overall SBLI induced separation flow topology for the uncontrolled case, a description of the main effects of AJVG systems for the reference case with an 8 mm spaced round jet array (referred as D8) will be now given. A comparison of the conventional schlieren pictures for the clean and D8 case is showed in figure 5.4 for the same inflow conditions of Ma=2.5 and $\delta_0 \approx 10mm$. The first

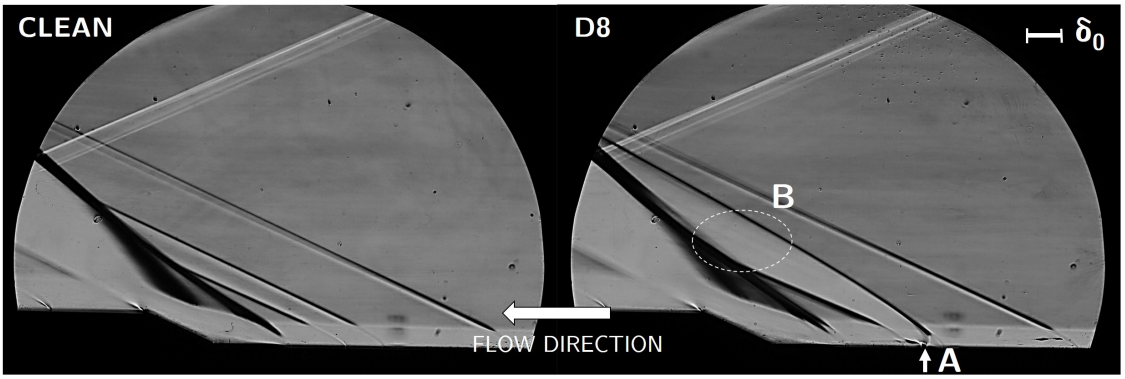

Figure 5.4: Conventional schlieren comparison of the clean and D8 AJVG cases. Taken with Canon EOS 550D 1/4000

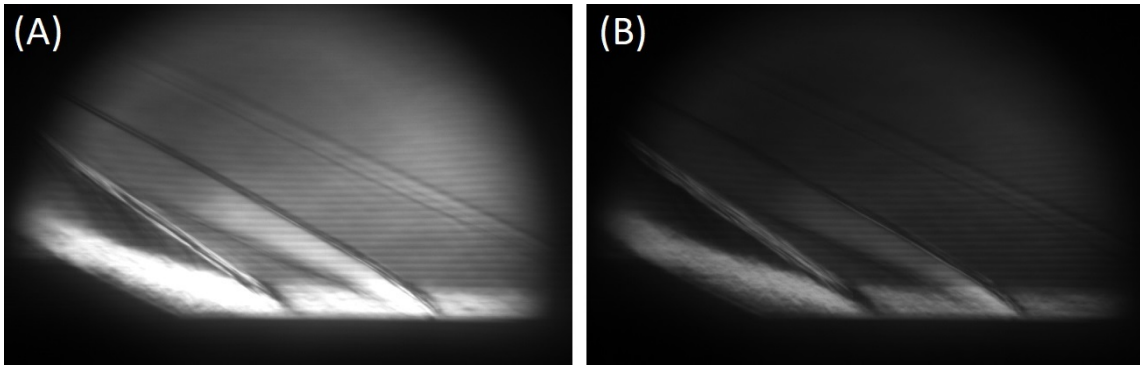

Figure 5.5: Focusing schlieren images for the D8 reference AJVG case: A) high cut-off, high light intensity (10 A), 1/240000 shutter speed. B) high cut-off, high light intensity, 1/525000 shutter speed.

main noticeable difference is caused by the air jets, where the injection point is indicated with 'A' in the right image. A bow shock is generated upstream of each of the 23 jets composing the array and a full span superposition of these shocks is clearly visible. The bow shock gradually bends away from the wall surface and turns in an oblique weaker disturbance as the obstruction of the jets gets less important. This jets-crossflow interaction also modify the initially parallel Mach lines structure present in the clean case, as they diverge (region 'B') from their original angle when interacting with the additional generated shock. The different intensity between the bow shock upstream of the jets and the weaker Mach lines can be appreciated more in the focusing schlieren pictures in figure 5.5, where the images are focused on a middle plane in the spanwise direction.

Downstream shifting of the separation shock can be observed through oil flow visualization (figure 5.6). Longitudinal vortices generated from the interaction of air jets with the main flow can be seen through the white traces in the surface. These

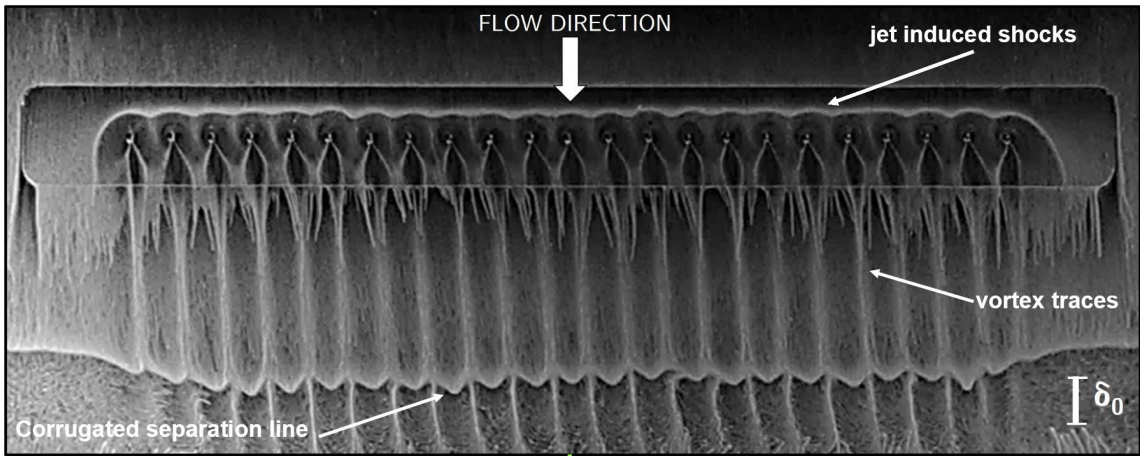

Figure 5.6: Oil flow visualization for the D8 AJVG array

vortices traces are still visible after the separation shock, indicating an effective convection within the boundary layer of the longitudinal vortices which are not completely dissipated by the shock intensity. The same phenomenon was reported by Szwaba [37]. The vortices' traces actually appears more defined downstream of the separation shock probably due to the overall reduced velocity in the reversed flow region within the boundary layer. As discussed previously (section 2.3), for an inclined injection, 45° in this case, a pair of vortices with unequal strength is formed and the oil pattern is characterised mainly by the stronger one. Streamwise accumulation of oil delimits the neighbour vortices generated. A characteristic structure of AJVG controlled separation, observed also in other studies [32, 17, 14], is the corrugated separation shock front. This wave-like contour is a consequence of the vortices interacting with the reverse flow of the separation region [32] and its peaks and indentation represent the maximum and minimum respectively of the separation length. As described by Verma et al [32], the indentations, thus the maximum separation length, correspond to the vortices' cores, while the peaks are located between two adjacent vortices and indicate the maximum shift of the separation shock. The fluctuation of these maxima and minima positions are relatively small ($0.1 \times \delta_0$) compared to the overall shift of the shock, as also verified by Souverein et al. [18]. On the sides of the jet array the vortices effect is no longer present, consequently the corrugated pattern disappear and the separation line moves upstream at the uncontrolled case position.

The jet induced bow shocks upstream of each injector cause a local separation of the flow and they are visible through the dark circular region around the orifices and the relative oil accumulation. As a consequence of the small spacing of the jets, individual bow shocks merge together in a wavy shock front. A similar merged bow shock front was observed by Verma et al. [32]. This bow shock pattern might be significantly modified by the implementation of sharp cornered orifices, such as the

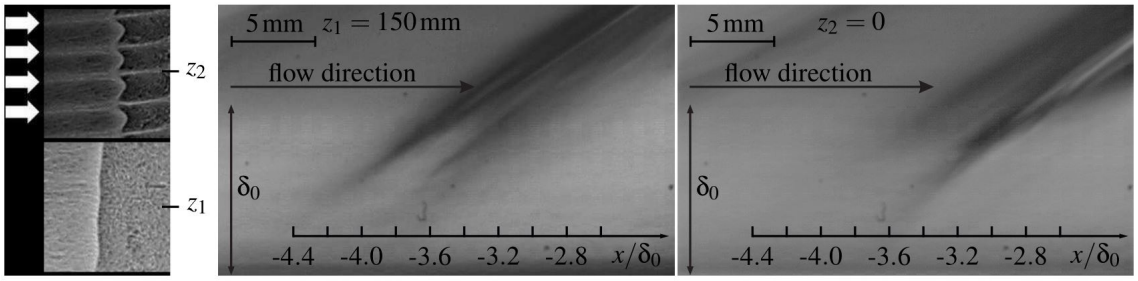

Figure 5.7: Focusing schlieren images of the separation shock shifting at different focal positions. Left: reference spanwise position of the two focused planes from the oil flow visualization. Center: schlieren detail of the separation shock focused in the uncontrolled region (z = 150mm). Right: schlieren detail of the separation shock focused in the controlled region (z = 0 mm) [86]

triangular injector proposed in this thesis. Jets are issued with a pitch angle to the left in respect to the incoming flow (thus to the right in figure 5.6) and this is visible from the slightly different bow shock of the two extreme jets of the array, the right one being wider, and from an overall small sideway drift in the injection direction induced by the vortices. These variation are negligible, therefore the general flow interaction can be considered symmetric in respect to the centre of the jet array.

Although less evident than from the oil visualization, the downstream shifting of the separation shock is visible also from the focusing schlieren pictures in figure 5.7. In these images two different spanwise focal positions z have been used, one in the sided uncontrolled region at $z_1 = 150mm$ where no jets are present and one in a middle plane $z_2 = 0$ where jets affect the flow field. The full $400mm$ model span goes from $z = -200mm$ to $z = 200mm$ and the $x/\delta_0 = 0$ axial position is set at the ramp corner. The different focus helps distinguishing both the uncontrolled shock position in the first image and the controlled one downstream of the jets in the second as the respective shocks appear sharper in each image. From these images a shift in the shock position of 0.7-0.8 δ_0 is visible, as confirmed by the following surface oil flow visualization.

A comparison between the clean and the D8 jet array configuration by means of oil flow visualizations is showed in figure 5.8, where both separation and reattachment lines are indicated. The two separation lengths are indicated as X_{clean} and $X_{jet-controlled}$ respectively. The extent of the reverse flow region is reduced approximately from 5,4 to 3,95 $\times\delta_0$, therefore it is $\approx$ 25% shorter in the controlled case. The average position of the corrugated line is located at circa 3,05 $\times\delta_0$ upstream of the ramp corner while the reattachment is moved approximately to just 0,9 $\times\delta_0$ downstream of the ramp corner. The reattachment pattern is similar in both clean and controlled cases, with no corrugation as for the separation in the latter, and its again detectable by the direction shifting of the flow traces. Curved and converging

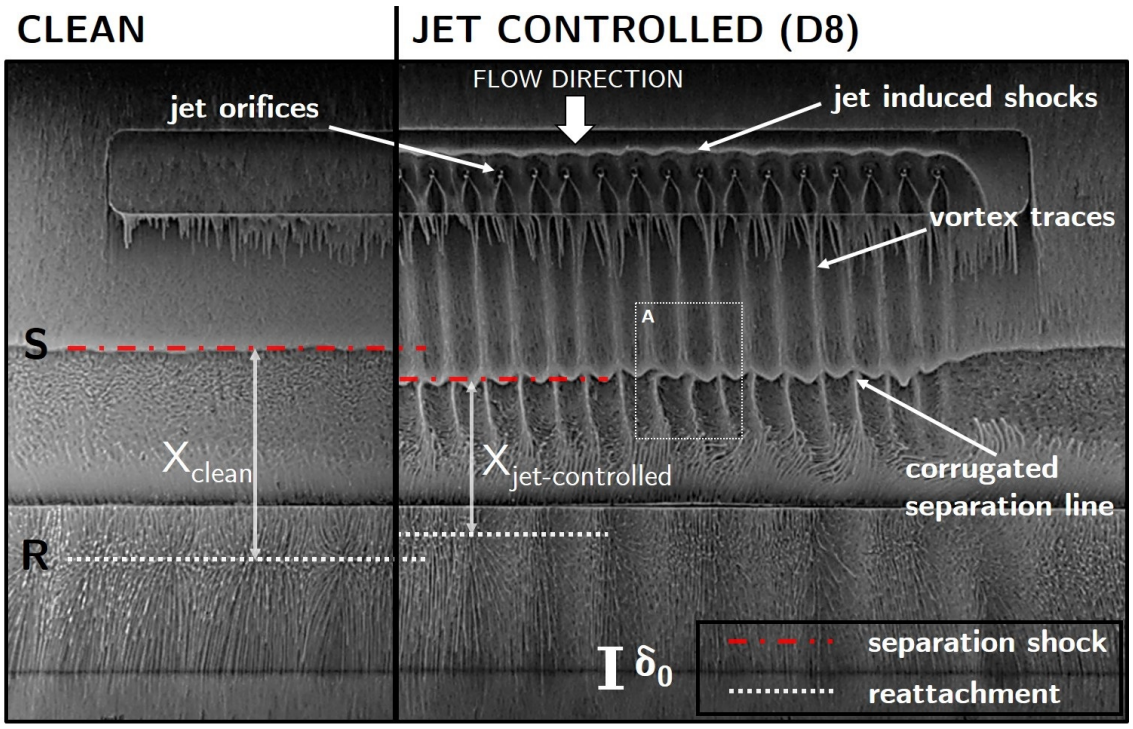

Figure 5.8: Comparison of the oil flow visualization for the clean and controlled D8 AJVG array

streamlines both upstream and downstream of the reattachment help visualizing it and form a particular cluster structure pattern. A comparable structure to the present case was obtained in Settles's experimental study [30] for a Ma=2.85 flow and in Dawson and Lele LES numerical simulations [87] for a Ma=2.9 flow, as can be seen in figure 5.9 and where both cases are without separation control. Dawson and Lele attribute the "alternating pattern of convergent and divergent streamlines" [87] to the up-wash and down-wash of Görtler vortices, typically generated in flow fields with concave surface. A comparable spacing of $1,5 - 2 \times \delta_0$ between the different cluster structures is present both in Dawson and Lele study and in this experimental configuration, with some small discrepancies attributable to the slight different Mach number and the superposition of the longitudinal vortices influence in the controlled case. In the presented controlled case (figure 5.8) the vortices' discrete traces are no longer visible in the reattachment zone as they vanishes at around $2 \times \delta_0$ from the separation line. This might be caused by the combined effect of reverse flow, gradual vortex energy dissipation and vortex lift-off from the surface as they convect downstream. This last aspect was reported also by Souverein et al. [18].

The obtained reduction is comparable to other AJVG shock induced separation control studies. Verma et al. [32] acquired a separation length reduction of 15% for

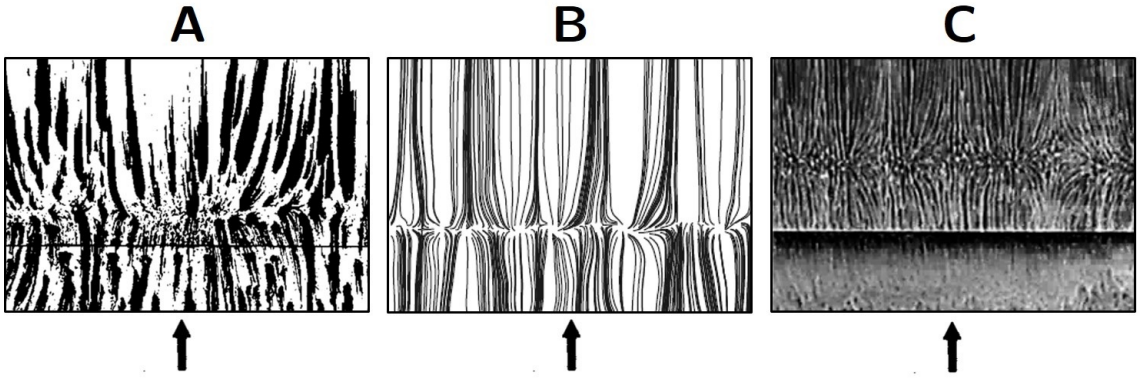

Figure 5.9: Comparison of the reattachment pattern on the ramp surface from Settles' [30] experimental study (A), from a streamline visualization of Dawson et al. [87] LES numerical study and from the present experimental case (C)

a $Ma_\infty = 2.05$ incoming flow. Their configuration presented slightly larger development length L and orifice diameter d_{jet}, but most importantly a larger spacing between the jets (1,5 $\times\delta_0$) compared to this setup ($0,8 \times \delta_0$), which might justify the lower reduction. Souverein et al. [18] observed a 25% variation for a $Ma_\infty = 2.3$ inflow, confirming the present work results since in their setup spacing ($1\times\delta_0$) and other AJVG parameters were more similar to this tested configuration. Although Johnston and Nishi [9] described the reattachment shift to be predominant in the overall separation reduction, this was not observed here.

5.3 Local flow field at the jet orifice

In order to obtain an effective reduction of the separation length, it is necessary that the jet and the relative counter vortex pairs generated from the interaction with the main crossflow remain within the boundary layer. In this section the bending process of the jets during the development of the stationary flow and a validation of the mentioned requirement are briefly illustrated. Figure 5.10 shows conventional schlieren pictures of different phases of the jet bending process and stationary flow development close to it. In picture A, the undisturbed jets without crossflow are visible, while picture B and C show the gradually bending of the jets as the main flow establishes. In detail D the flowfield is fully developed and it is possible to see that the jets remain within the boundary layer, as required for an effective AJVG system. Moreover, a thickening of the incoming boundary layer due to the air injection is also present. As already described in the previous section, the disturbance introduced by the jets generate a bow shock which extends into the main flow and of which the intensity decays moving away from the wall and from

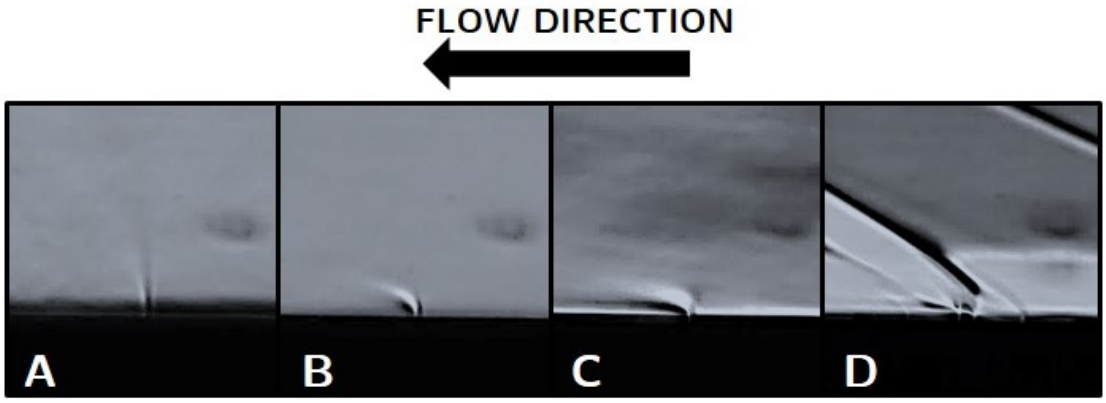

Figure 5.10: Schlieren images of the jet in crossflow development: (A) jet array in quiescent air. (B,C) transitional bending of the jet as the main flow develops. (D) fully developed jet-crossflow interaction. Size of the detailed images: 36 × 40 mm $\approx 3,6 \times 4\delta_0$.

the overall jet-crossflow interaction. The merging of the individual jets bow shock has been already showed by means of surface oil flow visualization in figure 5.6. Additional conventional schlieren pictures taken with an high speed camera with an exposure time of 1/10000 show further details in the injection area (figure 5.11). In the left figure (A) dark traces close to the wall surface indicate the filaments of the generated vortices which convect downstream within the boundary layer during the stationary part of the measurements. The underexpanded nature of the jet is showed in the right figure (B) for an injection in quiescent air. The dark stacked pattern indicates the presence of Mach disks and the relative barrel shock structure characteristic of underexpanded jets.

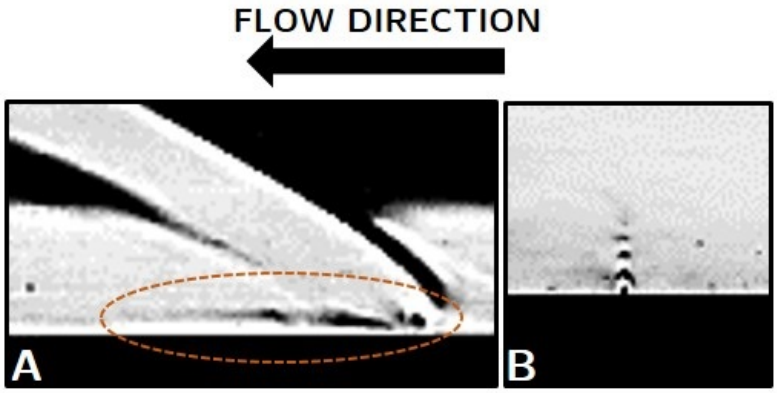

Figure 5.11: Schlieren jet details taken with high speed camera: (A) detail of the vortex traces, (B) Mach disks of the underexpanded jet in quiescent air. Size of the detailed images: (A) 36 × 21,5 mm $\approx 3,6 \times 2.15\delta_0$. (B) 18 × 20 mm $\approx 1.8 \times 2\delta_0$.

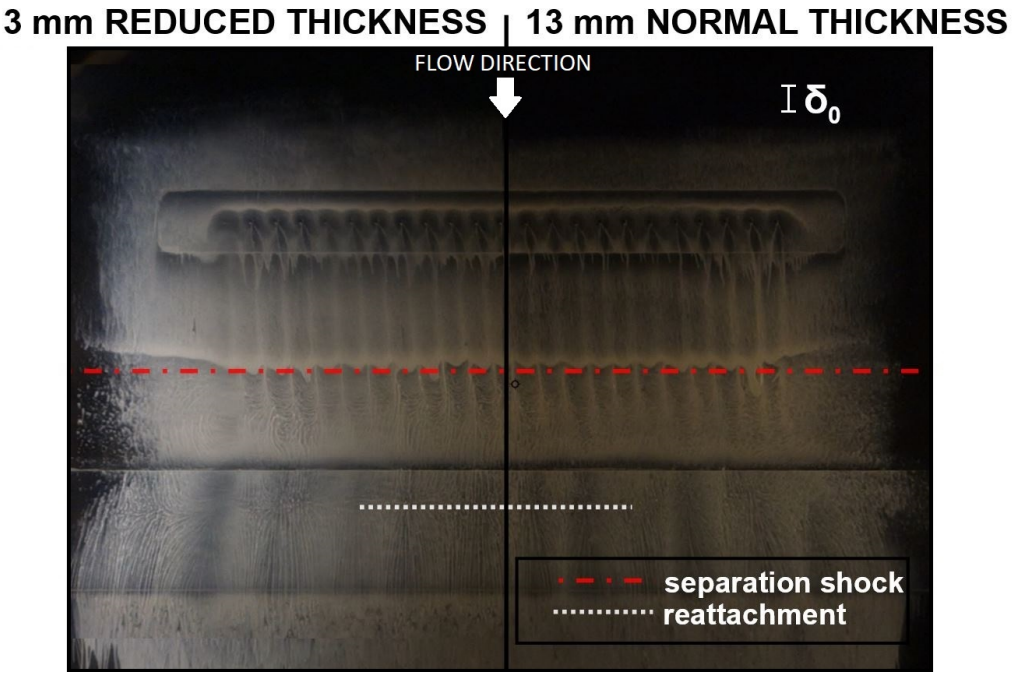

Figure 5.12: Oil flow comparison between reduced thickness (left) and reference (right) AJVG D8 inlets.

5.4 Reduced channel length circular injector

As the inlet thickness needed to be reduced for the manufacturing of non-circular AJVG inlets from 13 mm to 3 mm (section 4.2) an additional 8 mm spaced circular jet array with reduced channel length was tested to verify that no other side effects were introduced by this modification. An oil flow comparison of the reduced thickness inlet and reference D8 is reported in figure 5.12. The corrugated shock pattern is still preserved and there is no appreciable difference in both separation and reattachment positions. Secondly, since the triangular injector inlet is intended to be tested with both basis and vertex facing the flow, an assessment on the left and right injection has been performed for the reduced thickness inlet with circular orifices. It was tested with jet issuing both left and right in respect to the incoming flow direction. As can be seen from figure 5.13, similar separation shock position is obtained in this case, with only an opposite sideway drift of the traces due to the different jet orientations. In the reattachment area the vortex traces are no longer visible, therefore the region is similar for both jet directions. Focusing schlieren pictures with three different image settings of the reduced thickness model are reported in figure 5.14, where lower shutter speeds (pictures B and C) allow the visualization of finer turbulent structures. No changes in the flow topology from the full thickness D8 inlet are visible from these visualizations.

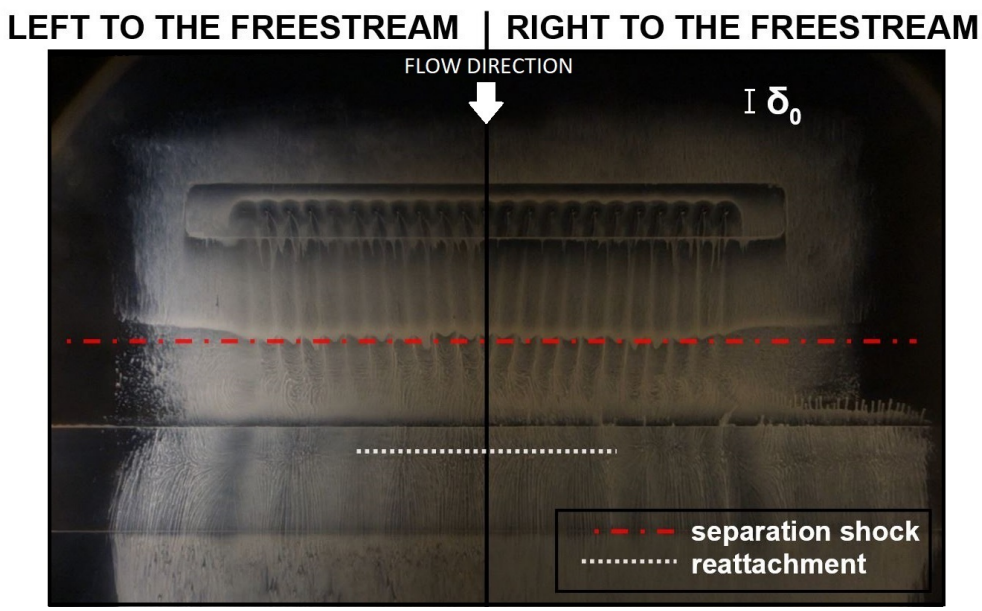

Figure 5.13: Oil flow comparison for the reduced thickness AJVG D8 with different jet directions in respect to the incoming flow direction (from top).

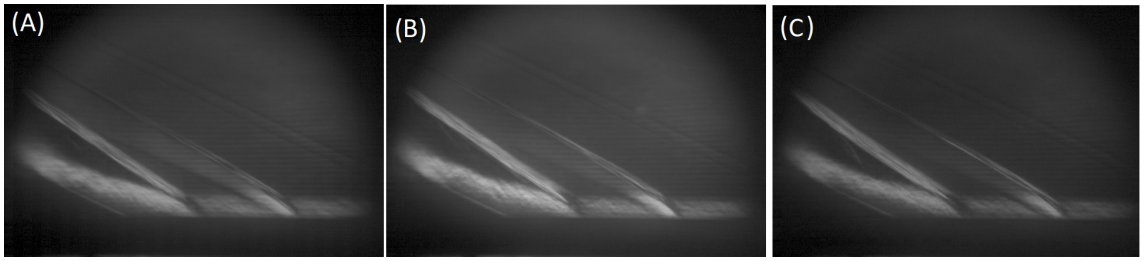

Figure 5.14: Focusing schlieren images for the reduced thickness D8 AJVG case (Jet to the left): A) high cut-off, low light intensity (4 A), 1/240000 shutter speed. B) high cut-off, high light intensity (10 A), 1/525000 shutter speed. C) high cut-off, high light intensity, 1/1000000 shutter speed.

5.5 Expected results from the AJVG arrays with non-circular holes

Due to severe delays in the manufacturing process of the non-circular inlets the scheduled schlieren and oil flow measurements for these AJVG configurations could not be performed, therefore in this section some consideration on the expected influence of the injector geometry on the effectiveness of AJVG systems will be reported here.

Four different shapes were selected (as discussed in chapter 3) to analyze three main geometric characteristic. First of all, the two different elliptic injector were selected to observe the influence of the section's aspect ratio. Although for subsonic crossflow it has been largely proven that high aspect ratios (> 1) result in a lower penetration (as a consequence of the larger spacing of the CVPs) while an higher penetration is obtained for low aspect ratios shapes compared to a circular injector [49, 52, 48, 55], the few studies on low aspect ratio elliptic injectors in supersonic crossflow showed an opposite trend [65, 67]. This could be a consequence of the higher spreading rate and faster axis switching for non-circular underexpanded jets as discussed by Schadow [71], since an underexpanded injection is typical of supersonic crossflow cases. Therefore the enhanced axis switching characteristic might overcome the aspect ratio influence and might also provide a lower penetration compared to circular jets in both low and high AR elliptic injectors, which would be positive in the AJVG separation control due to vortices closer to the wall surface and consequently to the less energized part of the boundary layer. However, Rao [15] claims that a larger spacing of the lateral edges, thus an high AR, generate stronger vortices also in transonic AJVG applications, even if his configuration presented rectangular injectors. In both elliptic cases, the azimuthal modes not present in the circular case could introduce additional turbulence [71], therefore an improved mixing. In conclusion, no certain prevision can be made due to the lack of experimental data on different aspect ratio jets in supersonic crossflow.

The second geometric characteristic considered is the presence of sharp edges and therefore the AR=2 rectangular injector was included in the test cases. This was the only shape of which a positive influence was already testified by other studies in AJVG applications. Rao [15] showed that rectangular injectors were more effective than circular counterparts for separation reduction in transonic airfoils, mostly because of the larger spacing of the two main vortices and their improved strength. Although only for subsonic cases, a stronger vorticity for the rectangular jets was observed by other studies [58, 59, 57]. Moreover the introduction of sharp edges and corners introduces finer scale turbulence in both subsonic and supersonic injections [64, 72] which enhances the mixing process. This however might affect the large-scale structure's coherence [72], thus altering the main vortex pair which is the

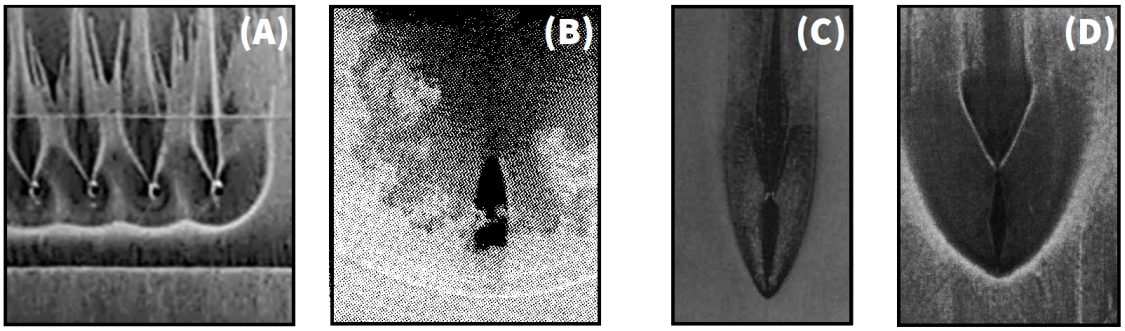

Figure 5.15: Surface visualizations of jet interaction with supersonic crossflow for different injector geometries: A) circular jets array from the presented experimental setup. B) Low aspect ratio elliptic injector from Gruber et al. [65]. C) Wedge shaped injector from Barber et al. [68]. D) Diamond shaped injector from Tomioka et al. [69].

leading actor in the momentum exchange process. In general, a stronger vorticity and a consequent stronger mixing might be observed in the selected case.

Last, the influence of sharp corners directed towards the incoming flow has been also considered. As demonstrated by other studies [68, 69, 70], a sharp vertex helps reducing the introduced disturbance to the main flow and therefore obtaining less recirculation closer to the injection point. In figure 5.15 the circular jet array (A) from the previous described measurement is compared with three other cases from the literature: low AR elliptic (B), wedge-shaped (C) and diamond (D) injectors. The detached bow shock in front of round jets causes additional recirculation ahead of the injection point, while this is either reduced or not present at all particularly for the wedge and diamond shapes as the shock is attached to the injector vertex and affects a narrower region. Due to its very low aspect ratio also the elliptic case (B) acts as a sharp cornered injector and presents a sufficiently attached shock, although not clearly visible from the image. In general, sharp corners mitigate the abrupt obstruction caused by blunt shapes, which might lead to lower disturbances at the surface level, reduced recirculation regions both upstream and downstream of the injection point and slightly lower total pressure losses. However, especially for diamond shaped cases, sharp corners provide an higher penetration which, if excessive, generates an overall larger obstacle to the incoming flow. More important if the jet penetrates outside the boundary layer region, the generated vortices would not be effective at all in the energizing process. For this reason the triangular shape was selected as its flat back side, combined with the inclined injection, could prevent an excessive penetration still preserving the positive effect of a sharp cornered injector and generate an effective vortices system within the boundary layer region. The reduced penetration characteristics of triangular shaped injectors, especially for subsonic cases, were described in chapter 3. Among the selected shapes this last one

could be the most promising for the considered supersonic case of this thesis as it could significantly vary the shock front ahead of the jet array and reduce the overall interference with the main flow.

As a final note, introducing different injector shapes could affect the optimal jet spacing and injection angles previously assessed also in other studies for the round jets array, since the generated vortex systems between adjacent jets could interact differently due to different penetration and counter-rotating vortex pair structure.

Chapter 6

Conclusions

6.1 Summary and conclusions

In this thesis shock-boundary layer interactions, the induced separation and its control by means of air jet vortex generators were analyzed. A first analysis of the effectiveness of the reference AJVG system with circular orifices was performed by means of schlieren and oil flow pictures. This configuration showed a 25% reduction of the separation length. The main aim of this work was to investigate the influence of non-circular injectors in AJVG applications. Therefore, an extensive literature study on non-circular jets in crossflow was performed. Among the different properties of this complex three-dimensional interaction, penetration, mixing characteristics and shock formation were indicated as main influencing factors for AJVG systems.

As a result of this literature survey, four shapes were selected in order to observe some critical geometric effects. First of all, two elliptic injectors with different aspect ratios were chosen, as this parameter was found to be crucial in the penetration properties of jets in crossflow. Then a rectangular injector with similar aspect ratio was included, since other studies on injectors with sharp corners claimed that these introduce finer turbulent scales that might affect positively the momentum exchange process of the AJVG mechanism. Finally, a triangular injector with a 30° sharp corner was chosen since sharp corners facing the incoming flow reduce significantly the introduced disturbances and mitigates possible additional recirculation regions downstream of the jet.

Subsequently, AJVG arrays with non circular injector were designed. Different manufacturing techniques were compared for the non-circular injectors. Among them electrical discharge machining and pulsed laser drilling resulted the most appropriate. The second one was selected mostly for reduced costs reasons. Limitation

imposed by the manufacturing process lead to some modification of the original inlet, with a drastic reduction of the inlet thickness from 13 mm to 3 mm and usage of different materials. To verify the presence of additional effects caused by the reduced jet channel length a comparison between the original D8 inlet and the reduced thickness model both with circular holes was performed and no significant difference was observed from the oil flow and schlieren visualizations. Due to severe delays in the manufacturing process of the non-circular inlets, oil flow and focusing schlieren measurements still need to be performed. Expected results from the selected shapes have been reported in this work.

6.2 Outlook

An effective way of processing the data from the focusing schlieren high speed video in order to estimate the inherent shock oscillation of SBLI and the eventual reduction with AJVG application is currently under investigation. Moreover, an improved colour focusing schlieren is being tested by Christopher Schauerte, who already designed the used focusing system.

Oil flow visualization will give only a rough estimation on the separation reduction by means of non-circular injectors, for this reason further PIV measurements could be beneficial to a better understanding on the shape influence on the jet-crossflow interaction. Measurements on perpendicular planes to the main flow would help to analyze the generated vortex size/strength and how they propagate toward the SBLI region. Additional measurements with seeded jets could provide a better insight on the jet penetration and mixing properties in the main flow.

Pressure measurement on the overall compression ramp model will be later performed, with both pressure sensitive paint and a second model with pressure probes, to estimate the total pressure loss caused by the shock induced separation and its mitigation with AJVG arrays.

Parallel to the experimental side, numeric simulation of the same flow configuration are being developed. Experimental results will serve as reference data to the numerical simulations. However, modelling of non-circular injectors could excessively complicate the already intricate three dimensional flow topology, therefore experimental results are of crucial importance.

Although diamond shaped injectors were excluded in this analysis due to a possible excessive penetration of the jet outside the boundary layer, a future effectiveness estimation of this configuration could be interesting since this geometric arrangement might introduce further less disturbances to the main flow and the excess in penetration could be counteracted by the inclined injection.

As a final remark, AJVG effectiveness has been verified in various application ranges, from separation control in engine intakes to drag and noise reduction devices. For this reason implementation of non-circular injectors also in these other systems and not only in the supersonic case considered in this work could significantly improve their already established capabilities without introducing additional components and maintaining the original simplicity of the system.

Bibliography

[1] D. S. Dolling, "Fifty years of shock-wave/boundary-layer interaction research: What next?" *AIAA journal*, vol. 39, no. 8, pp. 1517–1531, 2001.

[2] J. Delery, "Shock phenomena in high speed aerodynamics: Still a source of major concern," *The Aeronautical Journal*, vol. 103, no. 1019, pp. 19–34, 1999.

[3] H. Holden and H. Babinsky, "Shock/boundary layer interaction control using 3d devices," p. 447, 2003.

[4] P. Krogmann, E. Stanewsky, and P. Thiede, "Effects of suction on shock/boundary-layer interaction and shock-induced separation," *Journal of aircraft*, vol. 22, no. 1, pp. 37–42, 1985.

[5] H Babinsky, "Active control of swept shock wave/boundary layer interactions," in *Drag Reduction by Shock and Boundary Layer Control*, Springer, 2002, pp. 179–203.

[6] J. M. Delery, "Shock wave/turbulent boundary layer interaction and its control," *Progress in Aerospace Sciences*, vol. 22, no. 4, pp. 209–280, 1985.

[7] H. Pearcey, "Shock induced separation and its prevention," *Boundary layer and flow control*, vol. 2, pp. 1170–1344, 1961.

[8] J. C. Lin, "Review of research on low-profile vortex generators to control boundary-layer separation," *Progress in Aerospace Sciences*, vol. 38, no. 4-5, pp. 389–420, 2002.

[9] J. P. Johnston and M. Nishi, "Vortex generator jets-means for flow separation control," *AIAA journal*, vol. 28, no. 6, pp. 989–994, 1990.

[10] H. A. Holden and H. Babinsky, "Effect of microvortex generators on seperated normal shock/boundary layer interactions," *Journal of Aircraft*, vol. 44, no. 1, pp. 170–174, 2007.

[11] P Ashill, J Fulker, and K Hackett, "Research at dera on sub boundary layer vortex generators (sbvgs)," in *39th Aerospace Sciences Meeting and Exhibit*, 2001, p. 887.

[12] R. Wallis, "The use of air jets for boundary layer control," AERONAUTICAL RESEARCH LABS MELBOURNE (AUSTRALIA), Tech. Rep., 1952.

[13] R. Wallis and C. Stuart, *On the control of shock-induced boundary-layer separation with discrete air jets*. HM Stationery Office, 1962.

[14] G. Selby, J. Lin, and F. Howard, "Control of low-speed turbulent separated flow using jet vortex generators," *Experiments in Fluids*, vol. 12, no. 6, pp. 394–400, 1992.

[15] M. Rao, "An experimental investigation of the use of air jet vortex generators to control shock induced boundary layer separation," PhD thesis, City University London, 1988.

[16] T. P. Bray, "A parametric study of vane and air-jet vortex generators," 1998.

[17] R. Szwaba, "Shock wave induced separation control by streamwise vortices," *Journal of Thermal Science*, vol. 14, no. 3, pp. 249–253, 2005.

[18] L. Souverein and J.-F. Debiève, "Effect of air jet vortex generators on a shock wave boundary layer interaction," *Experiments in Fluids*, vol. 49, no. 5, pp. 1053–1064, 2010.

[19] P. Klebanoff, "Characteristics of turbulence in a boundary layer with zero pressure gradient," 1955.

[20] H. Schlichting and K. Gersten, *Boundary-layer theory*. Springer, 2016.

[21] H. Babinsky and J. K. Harvey, *Shock wave-boundary-layer interactions*. Cambridge University Press, 2011, vol. 32.

[22] S. B. Pope, *Turbulent flows*. IOP Publishing, 2001.

[23] D. Coles, "The turbulent boundary layer in a compressible fluid," *The Physics of Fluids*, vol. 7, no. 9, pp. 1403–1423, 1964.

[24] M. Perlin, D. R. Dowling, and S. L. Ceccio, "Freeman scholar review: Passive and active skin-friction drag reduction in turbulent boundary layers," *Journal of Fluids Engineering*, vol. 138, no. 9, p. 091 104, 2016.

[25] M. J. Lighthill, "On boundary layers and upstream influence ii. supersonic flows without separation," *Proc. R. Soc. Lond. A*, vol. 217, no. 1131, pp. 478–507, 1953.

[26] J. D. Anderson, *Modern compressible flow: with historical perspective*. McGraw-Hill New York, 1990, vol. 12.

[27] M. Van Dyke, *An album of fluid motion*. Parabolic Press Stanford, 1982.

[28] J. Délery and J.-P. Dussauge, "Some physical aspects of shock wave/boundary layer interactions," *Shock Waves*, vol. 19, no. 6, p. 453, 2009.

[29] G. S. Settles, I. E. Vas, and S. M. Bogdonoff, "Details of a shock-separated turbulent boundary layer at a compression corner," *AIAA journal*, vol. 14, no. 12, pp. 1709–1715, 1976.

[30] G. S. Settles, T. J. Fitzpatrick, and S. M. Bogdonoff, "Detailed study of attached and separated compression corner flowfields in high reynolds number supersonic flow," *AIAA journal*, vol. 17, no. 6, pp. 579–585, 1979.

[31] R. Hinke, "Design of an air-jet vortex generator array for the control of shock-induced flow separation," *Master Thesis, RWTH Aachen*, 2018.

[32] S. Verma and C Manisankar, "Shockwave/boundary-layer interaction control on a compression ramp using steady micro jets," *AIAA journal*, vol. 50, no. 12, pp. 2753–2764, 2012.

[33] A. M. Kuethe, "Effect of streamwise vortices on wake properties associated with sound generation.," *Journal of Aircraft*, vol. 9, no. 10, pp. 715–719, 1972.

[34] R. Szwaba, "Comparison of the influence of different air-jet vortex generators on the separation region," *Aerospace Science and Technology*, vol. 15, no. 1, pp. 45–52, 2011.

[35] A. Krzysiak, "Control of flow separation using self-supplying air-jet vortex generators," *AIAA journal*, vol. 46, no. 9, pp. 2229–2234, 2008.

[36] S. A. Prince, C. Badalamenti, and C. Regas, "The application of passive air jet vortex-generators to stall suppression on wind turbine blades," *Wind Energy*, vol. 20, no. 1, pp. 109–123, 2017.

[37] R. Szwaba, "Influence of air-jet vortex generator diameter on separation region," *Journal of Thermal Science*, vol. 22, no. 4, pp. 294–303, 2013.

[38] T. Fric and A Roshko, "Structure in the near field of the transverse jet," in *7th Symposium on Turbulent Shear Flows, Volume 1*, vol. 1, 1989, pp. 6–4.

[39] ——, "Vortical structure in the wake of a transverse jet," *Journal of Fluid Mechanics*, vol. 279, pp. 1–47, 1994.

[40] R. M. Kelso, T. Lim, and A. Perry, "An experimental study of round jets in cross-flow," *Journal of fluid mechanics*, vol. 306, pp. 111–144, 1996.

[41] J Santiago and J Dutton, "Crossflow vortices of a jet injected into a supersonic crossflow," *AIAA journal*, vol. 35, no. 5, pp. 915–917, 1997.

[42] M. Y. Ali and F. Alvi, "Jet arrays in supersonic crossflow—an experimental study," *Physics of Fluids*, vol. 27, no. 12, p. 126 102, 2015.

[43] H. Pearcey, K Rao, and D. Sykes, "Inclined air-jets used as vortex generators to suppress shock-induced separation," *AGARD, Computational and Experimental Assessment of Jets in Cross Flow 10 p(SEE N 94-28003 07-34)*, 1993.

[44] R. Portz and C. Segal, "Penetration of gaseous jets in supersonic flows," *AIAA journal*, vol. 44, no. 10, pp. 2426–2429, 2006.

[45] S Peterson and M Plesniak, "Short-hole jet-in-crossflow velocity field and its relationship to film-cooling performance," *Experiments in fluids*, vol. 33, no. 6, pp. 889–898, 2002.

[46] C. Singh, D. J. Peake, A. Kokkalis, V. Khodagolian, F. N. Coton, and R. A. McD Galbraith, "Control of rotorcraft retreating blade stall using air-jet vortex generators," *Journal of Aircraft*, vol. 43, no. 4, pp. 1169–1176, 2006.

[47] S Shun and N. Ahmed, "Airfoil separation control using multiple-orifice air-jet vortex generators," *Journal of Aircraft*, vol. 48, no. 6, pp. 2164–2169, 2011.

[48] F. F. Simon and M. L. Ciancone, "Flow visualization study of the effect of injection hole geometry on an inclined jet in crossflow," 1985.

[49] B. Haven and M Kurosaka, "Kidney and anti-kidney vortices in crossflow jets," *Journal of Fluid Mechanics*, vol. 352, pp. 27–64, 1997.

[50] B. A. Haven, "The effect of hole geometry on the near field character of crossflow jets," AIR FORCE INST OF TECH WRIGHT-PATTERSON AFB OH, Tech. Rep., 1996.

[51] D. S. Liscinsky, B True, and J. Holdeman, "Crossflow mixing of noncircular jets," *Journal of propulsion and power*, vol. 12, no. 2, pp. 225–230, 1996.

[52] M. Salewski, D. Stankovic, and L. Fuchs, "Mixing in circular and non-circular jets in crossflow," *Flow, Turbulence and Combustion*, vol. 80, no. 2, pp. 255–283, 2008.

[53] I. Ibrahim, S. Murugappan, and E. Gutmark, "Penetration, mixing and turbulent structures of circular and non-circular jets in cross flow," in *43rd AIAA Aerospace Sciences Meeting and Exhibit*, 2005, p. 300.

[54] E. J. Gutmark, I. M. Ibrahim, and S. Murugappan, "Circular and noncircular subsonic jets in cross flow," *Physics of Fluids*, vol. 20, no. 7, p. 075 110, 2008.

[55] T. Lim, T. New, and S. Luo, "Scaling of trajectories of elliptic jets in cross-flow," *AIAA journal*, vol. 44, no. 12, pp. 3157–3160, 2006.

[56] T. New, T. Lim, and S. Luo, "Elliptic jets in cross-flow," *Journal of fluid mechanics*, vol. 494, pp. 119–140, 2003.

[57] R. P. Weston and F. C. Thames, "Properties of aspect-ratio-4.0 rectangular jets in a subsonic crossflow," *Journal of Aircraft*, vol. 16, no. 10, pp. 701–707, 1979.

[58] X. Zhang and M. W. Collins, "Measurements of a longitudinal vortex generated by a rectangular jet in a turbulent boundary layer," *Physics of Fluids*, vol. 9, no. 6, pp. 1665–1673, 1997.

[59] X. Zhang, "An inclined rectangular jet in a turbulent boundary layer-vortex flow," *Experiments in Fluids*, vol. 28, no. 4, pp. 344–354, 2000.

[60] A. Sau, T. W. Sheu, S. Tsai, R. R. Hwang, and T. Chiang, "Structural development of vortical flows around a square jet in cross-flow," in *Proceedings of the Royal Society of London A: Mathematical, Physical and Engineering Sciences*, The Royal Society, vol. 460, 2004, pp. 3339–3368.

[61] M. Maidi and Y. Yao, "Numerical visualization of vortex flow behavior in square jets in cross-flow," *Journal of visualization*, vol. 11, no. 4, pp. 319–327, 2008.

[62] P. Ajersch, J.-M. Zhou, S. Ketler, M. Salcudean, and I. S. Gartshore, "Multiple jets in a crossflow: Detailed measurements and numerical simulations," in *ASME 1995 International Gas Turbine and Aeroengine Congress and Exposition*, American Society of Mechanical Engineers, 1995, V004T09A009–V004T09A009.

[63] J. M. Seiner, S. Dash, and D. Kenzakowski, "Historical survey on enhanced mixing in scramjet engines," *Journal of Propulsion and Power*, vol. 17, no. 6, pp. 1273–1286, 2001.

[64] E Gutmark, K. Schadow, and K. Wilson, "Noncircular jet dynamics in supersonic combustion," *Journal of Propulsion and Power*, vol. 5, no. 5, pp. 529–533, 1989.

[65] M. Gruber, A. Nejadt, T. Chen, and J. Dutton, "Mixing and penetration studies of sonic jets in a mach 2 freestream," *Journal of Propulsion and Power*, vol. 11, no. 2, pp. 315–323, 1995.

[66] M. Gruber, A. Nejad, T. Chen, and J. Dutton, "Transverse injection from circular and elliptic nozzles into a supersonic crossflow," *Journal of Propulsion and Power*, vol. 16, no. 3, pp. 449–457, 2000.

[67] G. Wang, L. Chen, and X. Lu, "Effects of the injector geometry on a sonic jet into a supersonic crossflow," *Science China Physics, Mechanics and Astronomy*, vol. 56, no. 2, pp. 366–377, 2013.

[68] M. J. Barber, J. A. Schetz, and L. A. Roe, "Normal, sonic helium injection through a wedge-shaped orifice into supersonic flow," *Journal of Propulsion and Power*, vol. 13, no. 2, pp. 257–263, 1997.

[69] S. Tomioka, L. S. Jacobsen, and J. A. Schetz, "Sonic injection from diamond-shaped orifices into a supersonic crossflow," *Journal of Propulsion and Power*, vol. 19, no. 1, pp. 104–114, 2003.

[70] R. D. W. Bowersox, H. Fan, and D. Lee, "Sonic injection into a mach 5.0 freestream through diamond orifices," *Journal of Propulsion and Power*, vol. 20, no. 2, pp. 280–287, 2004.

[71] K. Schadow, E Gutmark, S Koshigoe, and K. Wilson, "Combustion-related shear-flow dynamics in elliptic supersonic jets," *AIAA journal*, vol. 27, no. 10, pp. 1347–1353, 1989.

[72] E Gutmark, K. Schadow, and K. Wilson, "Subsonic and supersonic combustion using noncircular injectors," *Journal of propulsion and power*, vol. 7, no. 2, pp. 240–249, 1991.

[73] W. Quinn, "Streamwise evolution of a square jet cross section," *AIAA journal*, vol. 30, no. 12, pp. 2852–2857, 1992.

[74] J Mi, G. Nathan, and R. Luxton, "Centreline mixing characteristics of jets from nine differently shaped nozzles," *Experiments in Fluids*, vol. 28, no. 1, pp. 93–94, 2000.

[75] E. Gutmark and F. Grinstein, "Flow control with noncircular jets," *Annual review of fluid mechanics*, vol. 31, no. 1, pp. 239–272, 1999.

[76] B. J. Sutherland, "A redefined hydraulic diameter for laminar flow.," AIR FORCE INST OF TECH WRIGHT-PATTERSON AFB OH SCHOOL OF ENGINEERING, Tech. Rep., 1986.

[77] J Nikuradse, "Untersuchungen über turbulente strömungen in nicht kreisförmigen rohren," *Ingenieur-Archiv*, vol. 1, no. 3, pp. 306–332, 1930.

[78] R. Huebscher, "Friction equivalents for round, square and rectangular ducts," *ASHVE Transactions (Renamed ASHRAE Transactions)*, vol. 54, pp. 101–144, 1948.

[79] J. Heyt and J. Diaz, "Pressure drop in flat-oval spiral air duct," *ASHRAE Transactions*, vol. 81, no. Part 2, pp. 221–230, 1975.

[80] P Koch, "Equivalent diameters of rectangular and oval ducts," *Building Services Engineering Research and Technology*, vol. 29, no. 4, pp. 341–347, 2008.

[81] Z. Yu, K. Rajurkar, and H Shen, "High aspect ratio and complex shaped blind micro holes by micro edm," *CIRP Annals-Manufacturing Technology*, vol. 51, no. 1, pp. 359–362, 2002.

[82] G. D. Gautam and A. K. Pandey, "Pulsed nd: Yag laser beam drilling: A review," *Optics & Laser Technology*, vol. 100, pp. 183–215, 2018.

[83] R Patwa, H Herfurth, R Flaig, M Christophersen, and B. Phlips, "Laser drilling for high aspect ratio holes and a high open area fraction for space applications," *taper*, vol. 200, no. 10, pp. 0–05, 2014.

[84] S. Döring, "Analysis of the hole shape evolution in ultrashort pulse laser drilling," 2014.

[85] C. Schauerte, "Design of color and focusing schlieren optical systems for the examination of complex three-dimensional high-speed flows," *Master Thesis, RWTH Aachen*, 2018.

[86] C. Schauerte and A.-M. Schreyer, "Design of a high-speed focusing schlieren system for complex three-dimensional flows," *5th International Conference on Experimental Fluid Mechanics ICEFM 2018 Munich*, 2018.

[87] D. M. Dawson and S. K. Lele, "Large eddy simulation of a three-dimensional compression ramp shock-turbulent boundary layer interaction," in *53rd AIAA Aerospace Sciences Meeting*, 2015, p. 1518.